Year : 2021

Investigating, imaging and targeting the glioma microenvironment

Croci Davide

Croci Davide, 2021, Investigating, imaging and targeting the glioma microenvironment

Originally published at : Thesis, University of Lausanne

Posted at the University of Lausanne Open Archive http://serval.unil.ch
Document URN : urn:nbn:ch:serval-BIB_EF25E57E70AA1

UNIL | Université de Lausanne
Faculté de biologie
et de médecine

Département d'oncologie fondamentale

Investigating, imaging and targeting the glioma microenvironment

Thèse de doctorat en sciences de la vie (PhD)

présentée à la

Faculté de biologie et de médecine
de l'Université de Lausanne

par

Davide Croci

Biologiste diplômé, Master de l'ETH de Zürich.

Jury

Prof. Johanna A. Joyce, Directrice de thèse
Prof. Monika Hegi, Présidente
Prof. Michele De Palma, Expert
Prof. Mikaël Pittet, Expert

Lausanne
2021

Table of Contents

1. Acknowledgments

First, I would like to say that this page is the only one that no one reviewed before printing my thesis. I decided to do so, so that I might surprise you.

Exactly 5 years ago, I applied to the lab and asked my PI Johanna if I could stop by and have a coffee in order to introduce myself, since I was coming to Lausanne to visit some friends. In reality I came to Lausanne on purpose, once I knew we could have a coffee (but I still visited my friends of course). I thought a lot about how to describe my PhD journey under the scientific supervision and support of Johanna. Since I very much like sports, I'd like to compare her to a track-and-field official, specifically the one who was in Salamanca in 1993. That day Javier Sotomayor set the world record of high jump at 2.45 meters. That official set the bar up there, where excellence is. Johanna sets the bar high, to push our science beyond the current knowledge. I had to train a lot, I was excited, I was supported, sometimes I was tired. I don't own any world record, but I definitely jump higher and better than before, and I am truly grateful to you, Johanna, for that.

Of course, in sports you don't train and play alone. Last Olympics clearly showed that even high jumpers can team up and get the gold medal. I've learned a lot by sharing my time in the lab with brilliant scientists, colleagues and friends, and I'd like to thank Anoek, Joanna, Lucie, Leila and Klara for that, and of course all other past and previous lab members, collaborators, facility members, and anyone who allows us to do the best research possible. Also, a special thanks to Ruud. Our project is a good example of how it is important to look on the bright side of challenges. We might have never met, if it was not for the infinite troubles in getting that famous MRI, and here we are with a project I am very proud of.

Next, I'd like to thank my friends. First, you are all the best! Thanks to you all! Some of you deserve some extra words (for the other I am sorry, nothing personal, but the PhD school allows one page maximum of acknowledgments, which the 1.5 line spacing just made longer, but whatever…). To the Monto crew & co, you are a living example of how I was in the right spot at the right moment. Agli amici della Cazzöla del Pigi, e a quelli che meriterebbero di entrare nel club visto il vostro talento a "mangia e bef", grazie per essere dei portenti della natura. À les amis et amies de Neuchâtel et Lausanne, j'espère vivement de finalement être plus active sur le group «activités de je sais plus quelle saisons». À Annie pour tous les moments fun passé ensemble! A tutti gli altri amici e amiche del Ticino che non ci si vede mai

abbastanza. Alla Fio e allo Ste, siete semplicemente i migliori e non mi dilungo. À Claire qui a aidé beaucoup pendent des moments pas faciles, et naturellement aussi quand ça allait tout bien! À les amis de PluSport Martigny! À Roeltje, peut-être tu es déjà en train de rire ou sourire. Je pense que les mot «rire et sourire» sont un bon résumé de ces derniers ans.

Per finire, grazie alla mia famiglia: mamma, papi, Lisa, Luci, bro & family, la zia Sissi e i nonni, la mia cara madrina Nene, la Ros! Vi devo ringraziare per tante altre cose comunque, ed è semplicemente magnifico poter sempre contare su di voi.

To you, who just red this page, thank you! If I forgot you, I own you one, cheers!
À toi, qui vient de lire cette page, merci! Si je t'ai oublié, je te dois une choppe, santé!
A te, che hai letto questo pagina, grazie! Se ti ho dimenticato, te ne devo una, salute!

2. Summary

High-grade gliomas, the most common and aggressive primary brain tumors, are characterized by a complex and multifaceted tumor microenvironment (TME). Among the non-malignant cells of the glioma TME, tumor-associated microglia and macrophages (TAM) constitute the major compartment. In patients, a higher abundance of TAMs is associated with a higher grade and more aggressive disease. In different glioma mouse models, we observed specific TAM dynamics during tumor development and following therapeutic interventions, including irradiation. TAM abundance may also modulate the response to TAM-targeted therapy, including the anti-CSF1R inhibitor BLZ945, which has been previously shown by our lab to lead to a substantial tumor regression in preclinical models.

These observations indicate that it is crucial to evaluate TAM abundance and dynamics in gliomas. Current techniques to quantify TAMs in patients rely mainly on histological staining of tumor biopsies. While informative, these techniques require an invasive procedure to harvest tissue and typically only result in a snapshot of a particular region at a single point in time. Fluorine isotope 19 MRI (^{19}F MRI) has been shown to be a powerful tool to non-invasively and longitudinally monitor myeloid cells in other pathological conditions by injecting perfluorocarbon-containing nanoparticles (PFC-NP). In this thesis, I demonstrate the feasibility and power of ^{19}F MRI in glioma models (and brain metastasis models) and show that the major cellular source of ^{19}F signal consists of TAMs. Moreover, PFC-NP accumulation occurred predominantly in proximity to dysmorphic vessels, thereby enabling the identification of a TAM subpopulation with a specific oxidative metabolism. I also applied this technique in the context of irradiation (IR) treatment and found that the ^{19}F signal allows the tracking of TAM dynamics over time following IR. Moreover, multispectral ^{19}F MRI with two different PFC-NP allowed me to identify spatially- and temporally-distinct TAM niches in IR-recurrent tumors. Together, I have been able to image TAMs non-invasively and longitudinally with a powerful integrated cellular, spatial and temporal resolution, while revealing new biological insights into the many functions of TAMs, including in disease recurrence.

In my second major project, we aimed to achieve a higher imaging resolution, and implemented an experimental pipeline allowing intravital microscopy (IVM) combined with 2-photon (2p) microscopy of glioma-bearing mice. Through the surgical implantation of a cranial imaging window (CIW), we were able to record the behavior and migration of different cells *in vivo* in the tumor, and monitor the same mice longitudinally during tumor progression and in response to anti-CSF1R therapy. Importantly, we were able to image several cellular and non-cellular components of the TME, including cancer cells, microglia, peripheral immune cells,

the vasculature and the dura mater. Moreover, we applied dimensionality reduction analysis to our single cell IVM dataset, which allowed us to define various cell clusters with distinct phenotypic behavior (e.g. migratory ability).

Finally, in my third major project, I investigated the therapeutic efficacy of targeting TAMs via an anti-mouse-CSF-1R antibody (termed 2G2). I first evaluated the potential therapeutic benefits of 2G2 as a single agent, or in combination with either IR or anti-angiogenic treatment, but did not observe any substantial therapeutic effect. To understand the possible reasons underlying the lack of therapeutic efficacy, I explored the potential molecular mechanisms of CSF1R inhibition with 2G2, including the contribution of IL34, a brain-specific ligand of CSF1R. However, due to the incomplete and heterogenous penetration of 2G2 into the brain, and no evident phenotype in IL34-deficient glioma-bearing mice, we were not able to draw satisfying conclusions from this particular series of experiments.

3. Résumé

Les gliomes de haut grade, tumeurs cérébrales primaires les plus courantes et les plus agressives, sont caractérisés par un microenvironnement tumoral (TME) complexe et varié. La microglie et les macrophages associés à la tumeur (TAMs) constituent la majeure partie des cellules non malignes du TME des gliomes. Chez les patients, une forte abondance de TAMs est associée à une maladie agressive. Dans différents modèles murins de gliome, nous avons observé une dynamique spécifique des TAMs pendant le développement de la tumeur et après des interventions thérapeutiques, notamment l'irradiation. L'abondance de ces cellules peut également moduler la réponse à une thérapie ciblant les TAMs. C'est le cas pour l'inhibiteur anti-CSF1R BLZ945, qui entraine une régression tumorale substantielle dans des modèles précliniques, comme montré précédemment par notre laboratoire.

Ces observations indiquent qu'il est crucial d'évaluer l'abondance et la dynamique des TAMs dans les gliomes. Les techniques actuelles de quantification des TAMs chez les patients reposent principalement sur la coloration histologique des biopsies tumorales. Bien qu'instructives, ces techniques nécessitent une procédure invasive pour prélever les tissus et ne donnent généralement qu'une capture instantanée d'une région particulière à un moment donné. L'IRM de l'isotope 19 du fluor (IRM ^{19}F) s'est avérée être un outil puissant pour surveiller les cellules myéloïdes dans d'autres conditions pathologiques en injectant des nanoparticules contenant du perfluorocarbone (PFC-NP). Dans cette thèse, je démontre la faisabilité et la puissance de l'IRM ^{19}F dans des modèles de gliomes et je montre que la principale source cellulaire du signal ^{19}F est constituée de TAMs. J'ai également appliqué cette technique dans le contexte d'un traitement par irradiation (IR), que a permis de suivre la dynamique des TAMs dans le temps après l'IR. De plus, l'IRM multispectrale au ^{19}F avec deux PFC-NP différents m'a permis d'identifier des niches TAMs distinctes dans des tumeurs récurrentes par IR. J'ai donc été en mesure d'imager les TAMs de manière non invasive et longitudinale avec une puissante résolution cellulaire, spatiale et temporelle intégrée, tout en révélant de nouvelles perspectives biologiques sur les nombreuses fonctions des TAMs.

Dans mon deuxième projet, nous avons cherché à obtenir une résolution d'imagerie plus élevée et mis en œuvre un pipeline expérimental permettant la imagerie intravitale (IVM) combinée à la microscopie à 2 photons (2p) de souris porteuses de gliomes. Grâce à l'implantation chirurgicale d'une fenêtre d'imagerie crânienne (CIW), nous avons pu enregistrer le comportement et la migration de différentes cellules *in vivo* dans la tumeur, et suivre les mêmes souris longitudinalement pendant la progression de la tumeur et en réponse au traitement anti-CSF1R. Crucialement, nous avons été en mesure d'imager plusieurs

composants cellulaires et non cellulaires de la TME. De plus, nous avons appliqué une analyse de réduction de la dimensionnalité à notre ensemble de données IVM de cellules uniques, ce qui nous a permis de définir divers groupes de cellules au comportement phénotypique distinct (par exemple, la capacité migratoire).

Pour finir, dans mon troisième projet, j'ai étudié l'efficacité thérapeutique du ciblage des TAMs par le biais d'un anticorps anti-CSF1R de souris (appelé 2G2). J'ai d'abord évalué les avantages thérapeutiques potentiels du 2G2 en tant qu'agent unique, ou en combinaison avec l'IR ou un traitement anti-angiogénique, mais je n'ai pas observé d'effet thérapeutique substantiel. Pour comprendre les raisons possibles de ce manque d'efficacité thérapeutique, j'ai exploré les mécanismes moléculaires potentiels de l'inhibition du CSF1R par le 2G2, y compris la contribution de l'IL34, un ligand du CSF1R spécifique du cerveau.

4. Introduction

4.1 Invading the brain: the biological mechanisms of gliomas

4.1.1 The brain

The central nervous system (CNS) is composed of the spinal cord and the brain: the command-and-control center of our body and feelings. It integrates the external signals we capture with our senses and translates them into physiological responses that allow us to react to the outside world. Moreover, it is the source of intellectual thinking that is fundamental to the evolution and development of humankind. Such a fascinating organ is based on, and built by, a complex wiring network composed of the neurons [1] and other cells that exert crucial supporting roles to brain functions. Neurons are cells with a well-defined structure, where the main cellular body receives information from other neurons and transmits signals to distant cells through its axon, a specialized cellular compartment that allows a unique intercellular communication through the interplay of signaling molecules and electric stimuli [1]. Such a biological system allows this evolution-made "computer" to learn, update and run an infinite number of tasks. The neurons are necessarily supported by a plethora of other unique cells in the brain which fine-tune the crucial balance that enables the protection and wellness of this vital organ. Among these cell types, brain-resident oligodendrocytes are responsible for the axons' isolation, in order to ensure a proper electric signal transmission [2]. This process is called myelination and involves the deposition of a lipid-based layer (the myelin) around the axon's membrane, to avoid dissipation of the electrical current.

Microglia (MG) are the key brain-resident cells of the immune system that are responsible for patrolling the brain parenchyma and react in case of infection or injury to defend and heal the tissue [3]. This task is reinforced by astrocytes, the "handymen" of the brain, a cell type also involved in supporting neuronal activity and a major component of a brain-unique structure: the blood-brain barrier (BBB) (Figure 1) [4]. The BBB is a very specialized assemblage of different cell types and molecular cell junctions supporting the blood vessels in the brain and thereby controlling their permeability. The main role of the BBB is to shield the brain from infections by pathogens, or damage due to toxins or harmful compounds, while ensuring the passage of critical nutrients and oxygen. Moreover, under homeostasis, the BBB impedes the extravasation of peripheral immune cells, in order to hinder the mounting of detrimental inflammation reactions that could damage the tissue. For these reasons, the brain has been

historically regarded as an immune-privileged site [5]. However, this notion has been revisited by recent findings describing new roles for other structures in protecting the brain (Figure 1) [6]. First, the skull encloses the organ and protects it from physical impact and damage. Underneath the skull, a complex system of membranes forms the meninges (composed of the dura, arachnoid and pia mater), which ensures an additional level of protection for the CNS (Figure 1) [6]. Importantly, recent studies have found lymphatic vessels - a vascular system specialized in tissue drainage and immune cell trafficking - in the dura mater [7, 8]. These new findings have shifted the viewpoint on the immune-privilege of the brain, and better defined it as an immune-distinct site, where peripheral immune cells have no access to the parenchyma due to the presence of the BBB, but are able to effectively guard the surroundings and, under specific circumstances, mount an immune response [6, 9].

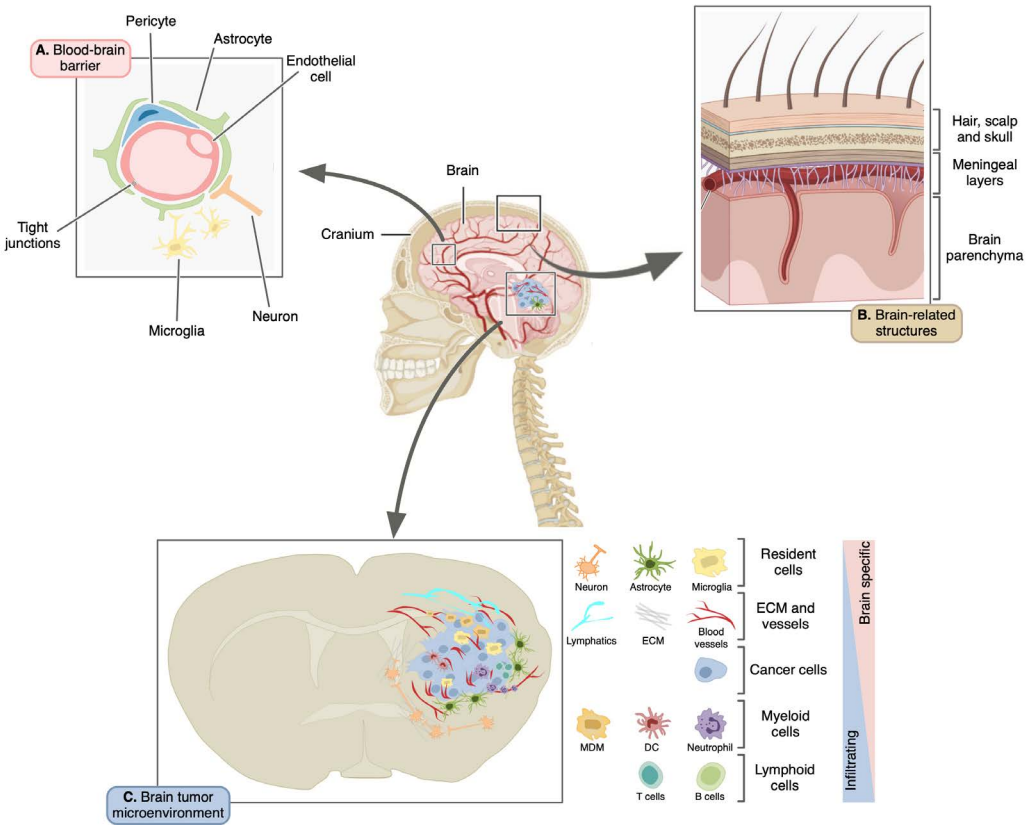

Figure 1

An overview of brain-resident cells and structures, and the composition of the brain TME. *A.* The blood-brain barrier (BBB) protects the brain from infection and harmful insults by regulating endothelial permeability. It is composed of endothelial cells, pericytes, astrocytes and the crucial support of tight junctions between cells. Microglia and neurons can also contribute to its regulation. In brain tumors, the BBB can be partially disrupted allowing the influx of peripheral immune cells and impacting drug distribution kinetics. *B.* Another layer of protection is the mechanical shield of the skull. Moreover, the three meningeal membranes (dura, pia and arachnoid mater) further support the brain. Of note, the dura mater is disseminated by lymphatic vessels which mediate the trafficking of the immune cells patrolling the brain surroundings. *C.* The malignant outgrowth of brain tumors leads to the establishment of a unique microenvironment composed of tissue-resident cells (neurons, astrocytes, microglia, oligodendrocytes), brain-associated structures (blood and lymphatic vessels, extra-cellular matrix (ECM)), malignantly transformed cancer cells, and parenchyma-infiltrating immune cells including monocyte-derived macrophages (MDM) and dendritic cells (DC). Adapted from [6, 10].

4.1.2 Brain development

The development of such a complex organ begins early in embryogenesis, as soon as the neural crest is formed [11]. Multiple steps are required for the accurate development of the CNS. Among these different processes, neurogenesis plays a crucial role in neuronal development [12]. The development of neurons starts from a series of neural stem cells (NSC) and neural progenitor cells (NPC) that reside in specific regions of the brain, called the ventricular zone (VZ) and the subventricular zone (SVZ) [12, 13]. After neurogenesis, these stem cell niches are maintained and can give rise to either neuroblasts (neuronal precursors) or supportive glial cells (oligodendrocytes or astrocytes) [11]. Importantly, these stem cell niches are supported by different cells and cellular structures, including the vasculature, microglia, astrocytes and other glial cells, and extra-cellular matrix (ECM) deposition [11]. This niche-microenvironment is fundamental during the complex development of the brain and later in adult life. Therefore, it is crucial that the proliferative and differentiation ability of the stem cells is tightly regulated in order to support the brain functions, but also to avoid unwanted and harmful proliferative expansions [12]. When this balance is disrupted, uncontrolled proliferation can lead to the formation of brain tumors [14].

4.1.3 Primary brain tumors

Primary brain tumors account for approximately 1.5% of all new diagnosed cancer cases in Switzerland and worldwide [15, 16]. The most recent classification of primary brain tumors by the World Health Organization (WHO) is based on both histological and genetic features [17]. Of all primary brain tumors, approximately one third are categorized as malignant (Figure 2) [18]. Of these, the majority are categorized as gliomas, ranging from less threatening disease to the most malignant forms (grade II to IV gliomas respectively). Brain tumors are hypothesized to originate from NSC that acquired genetic and epigenetic modifications allowing them to escape the tight control mechanisms typically regulating their proliferative ability [13, 14]. Among these genetic alterations, there are certain mutations that have been shown to specifically characterize the three main types of gliomas (oligodendroglioma, astrocytoma, glioblastoma) (Figure 2). Importantly, these mutations are also critical as prognostic indicators and impact the clinical management of the patient [18]. For instance, mutations in the isocitrate dehydrogenase 1 and 2 genes (*IDH1* and *IDH2*), two enzymes involved in oxidative metabolism and histone methylation, are found in low-grade (grade II and III) gliomas and are associated with a better prognosis [19]. Chromosome 1p and 19q co-

deletion combined with *IDH*-mutation is specific for oligodendroglioma. Low-grade gliomas can also be characterized by a CpG island methylator phenotype (G-CIMP positive state), often found in younger patients in combination with *IDH* mutations and associated with a better survival [20, 21]. The G-CIMP positive state can also be found in high-grade gliomas, typically when those are arising from recurrent/secondary low-grade malignancies. Among glioblastomas (grade IV), epigenetic modifications are also relevant. One example is the specific methylation of the O-6-methylguanine-DNA methyltransferase (*Mgmt*) gene promoter and consequent reduced gene expression. MGMT is a DNA-repairing enzyme and its silencing leads to a higher susceptibility to DNA-alkylating chemotherapeutics and, consequently, to a better survival of patients harboring this epigenetic alteration [22, 23].

Glioblastomas have been further classified in at least three different subtypes according to their transcriptomic signature [24], although other states have been described (Figure 2) [25, 26]. Specific mutations in oncogenes and tumor-suppressor genes define each subtype and have direct prognostic implications. The proneural subtype, characterized by an oligodendrocyte-like expression signature and frequent mutations in the platelet-derived growth factor receptor alpha (*Pdgfra*), tumor suppressor P53 (*p53*), phosphatase and tensin homolog (*Pten*) and *Idh* genes. These patients generally have a longer survival, though do not gain major advantages from standard of care therapy (surgery, radiation and chemotherapy) [25, 27]. Patients with glioma characterized by either the classical (astrocyte-like signature, epidermal growth factor receptor (*Egfr*) mutation) or the mesenchymal (activated-astrocyte/microglia-like signature, neurofibromin 1 (*Nf1*) gene mutated) signature, benefit most from an aggressive treatment schedule [25]. Moreover, the mesenchymal subtype generally has a higher infiltration of immune cells from the periphery [28]. The expression signatures of these subtypes indicate the potential role of the NSC and transdifferentiating cells that, in the transition to generate a specific cell type, may have acquired mutations that led to tumor formation, while partially retaining the traits of the lineage they were initially committed to [13]. Importantly, transitions between different cellular states have been described and were linked to the acquisition of new genetic and epigenetic modifications [26]. The resulting biological complexity leads to a high degree of intratumoral cellular heterogeneity [26, 29], which has a negative impact on response to therapy, due to the potential pre-existence of resistant clones [13]. Undeniably, glioblastomas have the worst prognosis among primary brain tumors with a median survival of only 14 months (5 years survival of only 5%) [27, 30-32]. This unfortunate clinical scenario, which has not seen significant improvements in more than 15 years, led the scientific community to a thoughtful consideration of the many challenges to overcome in order to better understand the biology of these tumors and thereby develop new treatments for glioma patients [14].

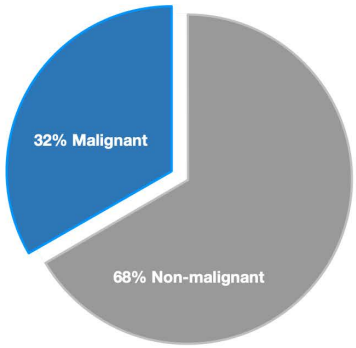

Disease	*Histology*		*Genetics*	*Type*
Glioma	Low grade (II, III)	*IDH* mut	1p/19q co-deletion; G-CIMP+ state	Oligodendroglioma
			G-CIMP+ state	Astrocytoma
	High grade (IV)	*IDH* wt	*MGMT* promoter methylation status	Glioblastoma

Glioblastoma subtype	*Expression signature*	*Genetics*	*Mouse Model Examples*
Proneural	Oligodendrocytes-like	*Mutations in PDGFRA, P53, PTEN, IDH*	RCAS/t-va GEMM (PDGFA and PDGFB driven) (Hambardzumyan *et al*., 2009)
Classical	Astrocytes-like	*Mutations in EGFR*	U87-EGFRvIII human cell line (Li *et al*., Frontiers in Oncology 2020)
Mesenchymal	Activated astrocytes/ microglia-like	*Mutations in NF1*	RCAS/t-va GEMM (NF1 mutated) (Ozawa *et al*., Cancer Cell 2014), Lentiviral GEMM (Magod *et al.*, Cell Reports 2021)

Figure 2

Classification of malignant primary brain tumors in adults. About one third of all primary brain tumors are classified as malignant gliomas, which are further precisely diagnosed according to histological and genetic/epigenetic features. Of note, low grade gliomas have a better prognosis than grade IV glioblastoma. At least 3 subtypes of glioblastoma can be identified based on their gene expression signature and specific (yet not exclusive) mutations. Importantly, recent single-cell studies have demonstrated that individual tumors contain different cell populations recapitulating the different subtypes. In order to better study this disease, several genetically-engineered mouse models (GEMM) of glioma have been described, and a representative selection is listed in the last column of the second table.

4.1.4 Research approach

Current brain tumor research efforts rely on an array of experimental techniques and approaches, which include both preclinical experimentation (*in vitro* and *in vivo* glioma models) and clinical research (from analysis of tissue samples to clinical trials) [14]. In recent years there has been an exponential increase in studies investigating the biology of human gliomas, studying the cellular composition and spatial organization, and applying multiple *omics* approaches, such as genomics, transcriptomics, and others [26, 33-35]. The invaluable findings from these studies are leading the way to a better biological understanding of human gliomas and, importantly, they also define the path of preclinical research. It is therefore crucial to establish a continuous crosstalk between the clinic and research laboratories. As an

illustrative example, assessment of glioma grade and subtypes (Figure 2) have a major impact on the disease biology, prognosis and clinical management. Therefore, the establishment of reliable mouse models and *in vitro* systems is essential to understand the limitations of current therapies and evaluate innovative treatments before entering into clinical trials [36-41]. Moreover, the development of experimental techniques which can be applied to both the clinic and preclinical models would allow the relevant direct comparison of the data, which can eventually advance the translational application and understanding of the preclinical research. I have therefore critically planned my projects to achieve this central objective, and developed therapeutic interventions and imaging methods which could potentially be directly implemented in the clinic.

4.2 Clinical management and novel treatments

4.2.1 Standard of care therapy

Current standard of care therapy for high-grade glioma patients consists of the surgical removal of the tumor, followed by fractionated irradiation up to 60 grays (Gy) with concurrent and adjuvant chemotherapy with temozolomide (TMZ), a DNA alkylating agent [18, 27, 30]. Patients are also commonly treated with antiepileptic drugs when experiencing seizures, and with corticosteroids to control perivascular edema [18]. Despite these aggressive treatments, however, tumors inevitably recur [27]. The challenges in treating this type of tumor rely on multiple factors. First, the highly infiltrative growth impedes the precise definition of the glioma boundaries and thus impacts the surgical removal of the entire tumor mass. Moreover, surgeons need to preserve the normal brain tissue so as to not affect critical neurological functions. Also, the high cellular heterogeneity and the presence of cancer cells with stem cell-like properties, increases the probability of the appearance of resistant clones [13, 14]. Consequently, there is an unmet need for better treatment options for these patients, and therefore researchers and clinicians are assessing the potential of new anti-cancer therapies in an ever increasing number of preclinical and clinical trials [42].

4.2.2 Immunotherapy

Over the past decade, cancer treatment management has seen a profound revolution. Milestone studies showing the importance of the immune system in controlling tumor appearance and growth have been translated into effective treatments [43]. The immune

system consists of two lines of defense: the innate immune cells at the frontline, and the more specialized adaptive immune cells, coming into play at later stages of the immune response. Tumor cells have been shown to block the attack of the immune system by different mechanisms, which modulate the immune cell phenotypes and activation states [43]. For instance, through the regulation of cell surface molecules, such as the programmed cell death 1 ligand 1 and 2 (PD-L1 and PD-L2), cancer cells can actively interact with immune cells and block their effector functions, thereby evading cancer cell killing. Moreover, the secretion of signaling molecules (*e.g.*, transforming growth factor beta (TGFβ), interleukin 10 (IL-10)) and the regulation of central metabolites (adenosine, tryptophane) further contribute to the generation of an immunosuppressive microenvironment. Importantly, the secreted factors can also lead to the additional recruitment of other immunosuppressive cell types, such as regulatory T cells. The therapeutic blockade of this cellular communication, through a range of different agents [44], unleashes the immune cells to actively target the cancer cells. Currently available immunotherapies mainly trigger an adaptive immune response by T cells, a specialized immune cell type with the ability to recognize exogenous pathogens, but also abnormal cancer cell antigens, and have led to a tremendous improvement in treating certain cancer types and enhancing survival for many patients [45]. In light of these breakthroughs for extracranial tumors, immunotherapies have also been assessed in brain cancers.

In gliomas, the BBB structure is altered and acquires more permeable features [46]. Consequently, brain tumors show a higher infiltration of peripheral immune cells which are generally not present in the normal brain parenchyma [33, 34]. The potential exposure of glioma cells to the immune system has stimulated the evaluation of several immunotherapy approaches in multiple clinical trials, attempting to tackle the immunosuppressed TME of glioblastoma from different therapeutic angles [47]. For example, checkpoint inhibitor blockade with therapeutic antibodies against the PD-1-PD-L1/2 axis or the cytotoxic T-lymphocyte-associated protein 4 (CTLA-4) has been investigated [47]. Moreover, engineered chimeric antigen receptor T cells have been designed to target glioblastoma-specific antigens, such as the epidermal growth factor receptor variant III (EGFRvIII) [47]. Last, the delivery and presentation of such tumor-specific antigens has been boosted with various vaccine approaches, including direct peptide administration or cellular therapy with dendritic cell-vaccines [47]. Nonetheless, there has been no widespread success to date in effectively treating these patients [14, 48, 49], other than a very modest survival benefit in a subset of patients with recurrent glioblastoma treated with either virotherapy or immune checkpoint inhibitors, whose tumors were characterized by a high inflammatory status and low tumor mutational burden (TMB) [50]. The counterintuitive correlation between low TMB (and consequently few neo-antigens that could be recognized by T cells) and therapy response

could not be fully explained by the authors. Indeed, the extended survival of this group could have been affected by additional factors such as time to tumor recurrence, which can subsequently impact tumor evolution and TMB [50]. Moreover, the unsatisfactory outcome of immunotherapies in glioma patients to date may also be partially related to the concomitant use of immunosuppressive chemotherapeutics and corticosteroids, as well as the generally immunosuppressive glioma microenvironment [46].

4.2.3 Anti-angiogenic treatments

Glioblastoma is one of the most vascularized cancer types [51]. A common hallmark of cancer is the formation of an aberrant and unstructured network of vessels that supports tumor growth [52]. While a tumor is growing, cancer cells can be depleted of nutrients and oxygen. The lack of oxygen, a condition called hypoxia, affects the oxygen-sensitive regulation of transcription factors that eventually leads to the enhanced expression and secretion of vascular growth factors, a process also common in gliomas, thereby inducing the formation of new blood vessels – termed angiogenesis [51, 53]. Anti-angiogenic therapies have therefore been developed to block the development of the new tumor vasculature. Interestingly, a normalization of the vessels, rather than a complete destruction, appears to be a more effective treatment option that can synergize with other therapies by allowing a better drug delivery to the tumor site [54, 55]. Importantly, the balance between vessel normalization versus destruction depends in part on the dosage of the anti-angiogenic agent used, which is still controversial [56, 57]. In this context, anti-angiogenic therapies have been tested in glioma patients. Although different conclusions have been reported in distinct clinical trials [51], the anti-angiogenic antibody bevacizumab (an antibody blocking the vascular endothelial growth factor-A (VEGF-A)) is currently approved for the treatment of glioma patients (in the United States of America, Canada, Switzerland and other countries, but not in the European Union) [58]. Important benefits to quality of life, edema control and the reduced use of corticosteroids have been described [51]. However, long-term studies have shown only a limited effect on the survival of a subset of patients [59, 60].

The poor outcome of standard of care therapy, and the failure of novel therapies to show efficacy in gliomas, highlight the need to understand in depth the underlying complex biology and the interactions occurring between all the different cells within a tumor mass. Importantly, while the current and innovative treatment modalities often focus on targeting just one cell type, it is crucial to investigate and exploit all cellular players of such a unique milieu: the brain tumor microenvironment (TME) (Figure 1) [46]. Moreover, many components of the TME are also affected by the individual treatments, which leads to a constant and dynamic reshaping

of the TME composition and cellular phenotypes, which I investigated during my Ph.D. to better understand the type, sequence and timing of the therapies required.

4.3 The complexity of brain tumors

4.3.1 The brain tumor microenvironment

Upon BBB leakage in brain tumors, multiple novel cellular interactions are established between cancer cells, non-malignant resident cells, infiltrating immune cells and non-cellular components such the ECM (Figure 1) [10]. Several recent studies have addressed the composition and cellular communication in the TME of different brain malignancies, including *IDH*-mutant and *IDH*-wildtype gliomas, and brain metastases originating from diverse primary sites [33, 34]. These studies revealed that the genetic background of brain tumors strongly affects the degree and ontogeny of immune cell infiltration. Moreover, it impacts the phenotype of these cells, including their proliferation and activation state [33, 34]. Interestingly, among all cells of the brain TME that have been identified, the immune cell population that is by far the most abundant in gliomas are the tumor-associated microglia and macrophages (TAMs).

4.3.2 Tumor-associated macrophages

The innate immune system is our first-line defense mechanism and is critical for the immediate response upon injury or infection. Innate immune cells incorporate mononuclear phagocytes (macrophages, monocytes, dendritic cells), granulocytes (basophils, eosinophils, neutrophils) and others. Macrophages exert several tissue-specific roles, from immune surveillance and resolution of inflammation, to support of homeostatic functions such as debris clearance and iron processing [61, 62]. Colonization of tissue macrophages starts early during embryogenesis, while other immune populations are established or replenished at later stages during development from peripherally-derived monocytes. For instance, the resident CNS macrophages comprise the parenchymal MG and non-parenchymal border-associated macrophages (BAMs) which include perivascular, meningeal and choroid plexus macrophages [63-65]. While these different subpopulations originate early from yolk sac progenitors, dural and choroid macrophages also receive contributions from adult hematopoiesis [63, 64]. The brain TAM populations are mainly characterized by two major and distinct populations [66, 67]: the resident MG, and the monocyte-derived macrophages (MDMs), which gradually infiltrate during tumor progression [33, 34]. While these two different

macrophage populations share a common core genetic signature, driven by their education within the tumor milieu, they also possess their own distinct ontogeny- and tumor-driven phenotypes. Indeed, MG and MDMs have distinct and specific functions and activation states [66], including antigen presentation potential and proliferative ability [33].

The TAM phenotype has often been connected to the dichotomy of the “M1” and “M2” polarized macrophage phenotypes [68]. M1 macrophages, or pro-inflammatory macrophages, are mainly activated in response to interferon gamma (IFNγ) signaling and, in the context of cancer, exert an anti-tumorigenic function [68]. M2 macrophages, or non-classical macrophages, are mainly driven by exposure to interleukin 4 (IL-4), interleukin 10 (IL-10) and/ or interleukin 13 (IL-13), and have been shown to favor an immunosuppressive microenvironment in different tumor types [68]. Although overly simplified, the M1/M2 paradigm has revealed several of the different functions of TAMs. Importantly, a number of studies have now demonstrated a much broader plasticity and heterogeneity in the phenotype of these cells, which encompasses various pro- and/or anti-tumorigenic functions [33, 34, 67, 69]. Of note, in several cancer types macrophage abundance has been associated with a worse patient prognosis, including glioma [70]. In glioma mouse models, TAMs have been shown to possess a M2-like phenotype, and support tumor progression [71-73], contribute to the immune suppressive environment [74] and hinder the efficacy of standard of care therapy [75]. These findings have been corroborated in human samples, where TAMs express different T-cell inhibitory factors [33]. Consequently, TAMs emerge as an attractive target to potentially re-activate their anti-tumoral state and establish an immune response against cancer cells [76].

4.3.3 Therapeutic approaches targeting TAMs

Several different strategies have been proposed to therapeutically target brain TAMs [46, 76]. One approach is based on the notion of re-education, which implies the ability of certain drugs to modulate TAMs towards an anti-tumorigenic phenotype, which can lead to direct killing of cancer cells and their phagocytosis, or via indirect mechanisms by modulating other cells in the TME, such as T cells [76, 77]. Another strategy involves TAM depletion, whereby TAMs are directly killed or their recruitment into the tumor bed is blocked, and thus they can no longer exert their pro-tumor functions [76, 77].

One of the most promising interventions to re-program the TAM phenotype to an anti-tumorigenic state is through the modulation of the CD47-SIRPα phagocytic axis [78]. CD47 is a “don’t eat me” signal expressed on cancer cells in several solid tumors, including glioma

[79]. CD47 is recognized by its ligand SIRPα, which is expressed by macrophages (and dendritic cells), and several mechanisms can be engaged to prevent macrophages from phagocyting CD47-expressing cells. Administration of anti-CD47 antibodies led to increased survival in glioma models by unleashing the phagocytosis of tumor cells by TAMs when combined with standard of care chemotherapy using temozolomide (TMZ) [78]. Moreover, this treatment favored increased antigen presentation and T cell priming [78]. Other therapeutic strategies involve the direct targeting of immune-modulators expressed by TAMs. In a recent preclinical study, TAMs have been shown to express PD-L1 in glioma models, which blocks T cell effector functions upon interaction with its receptor, programmed cell death protein 1 (PD1) [74]. Disruption of the PD1-PDL1 interaction boosted the immune response in combination with a dendritic cell-based cancer vaccine and led to a longer survival of the animals [74]. Taken together, these studies show the potency of interfering with different effector functions of macrophages and unleashing their potential anti-tumoral functions. Importantly, these therapeutic approaches are currently being investigated in several clinical studies [80-83].

Conversely, TAM depletion relies on the elimination of macrophages from the TME, either by inhibition of their recruitment to the tumor bed or by interfering with their survival there [76, 77]. This strategy has been achieved experimentally with different approaches in diverse cancer models, including blockade of CCL2 cytokine signaling (a monocyte chemoattractant) or via the delivery of clodronate liposomes [84-86]. Other studies have proposed targeting of the colony-stimulating factor 1 receptor (CSF1R) as a strategy to deplete TAMs in glioma [87] or other cancer types [88, 89]. Importantly, multiple reports have clearly shown how CSF1R inhibition leads to TAM re-education rather than depletion in glioma models [72, 73, 75, 90]. In light of these studies, and due to the central role of CSF1R signaling in macrophage biology, a substantial effort has been made to deeply understand the mechanism and therapeutic outcome of blocking this key pathway.

4.3.4 Therapeutic targeting of CSF1R

During their development, and later on throughout homeostasis, macrophages rely on the CSF1R signaling pathway, which promotes their survival, proliferation and differentiation [91]. CSF1R is a tyrosine kinase receptor that triggers intracellular phosphorylation cascades via the phosphoinositide 3-kinase (PI3K) signaling pathway and others [92], upon binding to its ligands colony-stimulating factor 1 (CSF1) or interleukin 34 (IL34) [92, 93]. Multiple approaches have been taken to block CSF1R signaling, ranging from small-molecule tyrosine kinase inhibitors to therapeutic antibodies targeting the receptor or the ligands [89, 94]. In

preclinical models of glioma, several CSF1R-targeting compounds have shown promising results as monotherapy and in combination with standard of care therapy or immunotherapies [72-75, 87, 90]. In two distinct studies, two molecularly different small-molecule kinase inhibitors of CSF1R, BLZ945 (Novartis) and PLX3397 (Plexxikon), were shown to have a potent antitumoral effect and a significant reduction of the tumor mass after only 1 week of treatment [72, 90]. Interestingly, while CSF1R inhibition led to MG depletion in the normal contralateral brain, TAMs were protected within the residual tumor. It was found that upon BLZ945 treatment, TAM survival was actually supported by glioma cell-secreted factors, including IFNγ, granulocyte-macrophage colony-stimulating factor (GM-CSF) and C-X-C motif chemokine ligand 10 (CXCL10). Moreover, TAMs were re-educated from a M2-like phenotype (though there was no global increase in M1-like markers), which was associated with a significant increase in their phagocytosis of cancer cells [72, 73].

While very effective in initially regressing large high-grade gliomas in all mice, long-term treatment with BLZ945 led to the emergence of therapy resistance in about 50% of the treated animals [73]. In resistant tumors, an interleukin 4 (IL4)-driven production of insulin-like growth factor 1 (IGF1) by TAMs supported tumor growth, and mouse survival could be improved by the combinatorial inhibition of different nodes involved in mediating this resistance mechanism [73]. These findings showed the importance of combinatorial strategies to effectively target the multifaceted complexity of the brain TME. In this regard, CSF1R signaling inhibition with BLZ945 and consequent TAM re-education has also been reported to be effective in the context of IR, showing a far more robust therapeutic effect than simply blocking the recruitment of MDMs [75]. In addition, PLX3397 enhanced the efficacy of multi-target tyrosine kinase inhibitors that otherwise showed a modest efficacy as monotherapies [90]. Moreover, CSF1R targeting has been shown to synergize with and improve immunotherapeutic treatment outcomes [74, 95]. Of note, another study in a different glioma model (GL261 orthotopic transplant model) reported that CSF1R inhibition led to TAM depletion instead, resulting in reduced tumor invasion [87]. The promising results of these different preclinical studies contributed directly to the investigation of CSF1R inhibitors in glioma patients in ongoing clinical trials [96, 97]. These studies highlighted the potential of CSF1R targeting and the importance of studying this in combination with standard and novel therapies, an aspect that I further investigated as presented in this thesis, where I assessed the effect of other relevant therapies such as anti-angiogenic drugs. In this regard, assessing TAM content, dynamics and phenotype will become a crucial diagnostic tool to support decision-making steps in the clinical management of patients.

4.4 Experimental approaches to image and quantify TAMs

4.4.1 Standard methods and mouse models

Imaging and quantification techniques to study TAMs include standard experimental approaches such as immunofluorescence (IF) staining or fluorescent-activated cell sorting (FACS), that can be applied to both clinical samples and animal models. These techniques are based on antibodies which precisely recognize cell-specific antigens, thereby enabling their detailed phenotyping by different imaging approaches, including microscopy and FACS. More sophisticated methods have been developed to precisely address cell ontogeny in murine models, including of macrophages. Importantly, these cell-lineage tracing models allow the classification of macrophage subpopulations, and discriminate tissue-resident cells from peripheral infiltrating monocytes [63, 66, 98, 99]. Generally, these murine models rely on the ectopic expression of fluorescent proteins under the control of gene promoters which are expressed by either the resident or the peripheral macrophages (Figure 3). One example is the Flt3:Cre; Rosa26:mTmG mouse line [99]. In this model, the fluorescent protein tdTomato is expressed by all cells, but peripheral hematopoietic cells also express the green fluorescent protein (GFP) under the control of the fms-related receptor tyrosine kinase 3 (*Flt3*) promoter [99]. In a recent elegant study, the authors combined the differential expression of the N- and C-terminus of the Cre recombinase enzyme (Cre), an enzyme with the ability to recognize specific ectopic DNA-sequences and excise portions of the genome, in order to direct the enzyme activity in a subset of cells only [63]. Specifically, the Cre C-terminus was expressed in all macrophages under the control of the C-X3-C motif chemokine receptor 1 (*Cx3cr1*) promoter, while the N-terminus was differentially expressed in MG and a subset of perivascular macrophages (PVM), under the control of the MG-specific spalt-like transcription factor 1 (*Sall1*) promoter and the PVM-specific lymphatic vessel endothelial hyaluronan receptor 1 (*Lyve1*) promoter respectively [63]. Other models instead exploit the differences in the natural turnover of MG and MDMs. Cx3cr1:CreERT2-IRES-YFP;Rosa26:lslTdTomato mice express a tamoxifen-inducible Cre (tagged with the yellow fluorescent protein (YFP)) under the control of the *Cx3cr1* promoter [98]. Following tamoxifen treatment and Cre activation in all CX3CR1-positive cells, the expression of tdTomato is induced in both MG and MDM populations. Approximately 3 weeks after tamoxifen treatment, the MDM pool is replenished due to its natural turnover, and all new cells do not express tdTomato since they were not Cre-recombined, while MG maintain the expression of both fluorescent proteins [98]. The application of these lineage-tracing lines to brain tumor models allowed the study of the ontogeny of TAMs, and revealed important differences in the transcriptional programs and

chromatin-organization between MG and MDMs, and also led to the identification of specific cell-surface markers identifying these populations in both murine and human brain tumors [66].

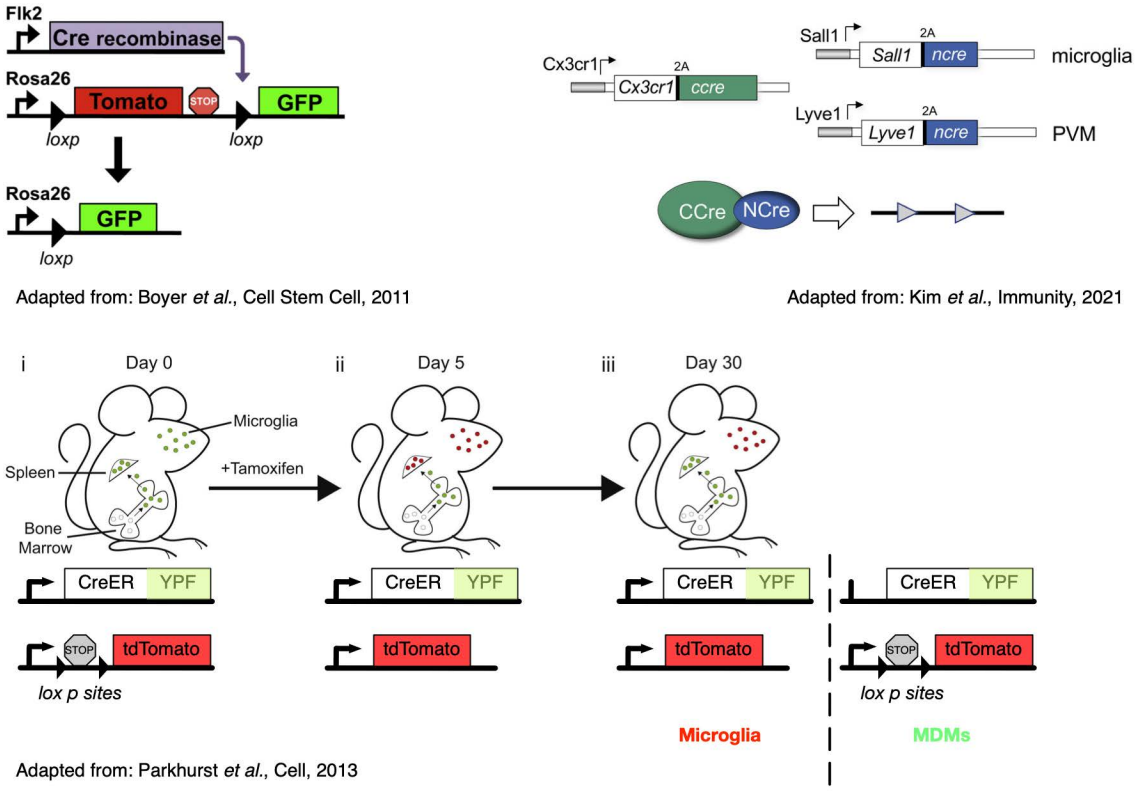

Figure 3

Different cell-lineage tracing models to discriminate tissue-resident vs. infiltrating macrophages. Upper left: graphical illustration of the cell-lineage tracing strategy to discriminate infiltrating from resident immune cells. GFP labelling is restricted to peripheral immune cells expressing the hematopoiesis factor FLT3 (*Flk2*), while resident cells express tdTomato (including MG). Upper right: a binary split Cre transgenesis system allowing the differential imaging of *Cx3cr1*-, *Sall1*-expressing MG and *Cx3cr1*-, *Lyve1*-expressing perivascular macrophages (PVM). Bottom: CreER-YFP expression is driven by the *Cx3cr1* promoter (i). All CX3CR1-positive macrophages are recombined upon tamoxifen treatment (ii). 3 weeks after treatment (iii), the bone marrow-derived macrophages undergo a complete turnover and are therefore tdTomato-negative, while long-lived MG retain the expression of both fluorescent proteins.

4.4.2 Intravital imaging

A critical advance in the imaging field, whereby lineage tracing models have demonstrated their vast potential, has been the implementation of cutting-edge techniques that enable the longitudinal imaging of the same individual mice. These research tools allowed the field to transition from single “static” data of specific time-points to a comprehensive understanding of the TME dynamics over time, as well as the migratory ability of individual cells. One example is two-photon (2p) microscopy: a technique that allows one to image cells in living animals. In conventional microscopy the excitation wavelength is shorter than the emission wavelength

(Figure 4). 2p microscopy instead requires the simultaneous excitation by two photons with a longer wavelength than the measured emission light. Technically, this is achieved by using light in the infra-red (IR) spectrum (with a long wavelength). Practically, the simultaneous excitation by two photons allows less scattering and phototoxicity, while the long NIR wavelengths achieve a high-resolution and high tissue imaging depth (Figure 4) [100]. Moreover, 2p microscopy permits the label-free imaging of collagen-rich structures, a process termed second harmonic generation (SHG) [100]. In order to use 2p microscopy in living animals, a method referred to as intravital imaging (IVM), it is necessary to gain visual access to the tissue. For this purpose, different imaging window techniques have been developed, including cranial imaging windows (CIW) that allow *in vivo* 2p microscopy of the brain and brain tumors [101-103]. For instance, the migratory behavior of fluorescently-labelled cancer cells in the tumor core and margin could be observed in living glioma-bearing mice, allowing the identification of distinct patterns of cancer cell invasion of the surrounding brain. [101]. Another study focused on the morphological and migratory differences between MG and MDMs at fixed timepoints (though not in long-term studies over time) [103]. These authors showed that MG are generally larger and more branched than MDMs, which were smaller and more migratory.

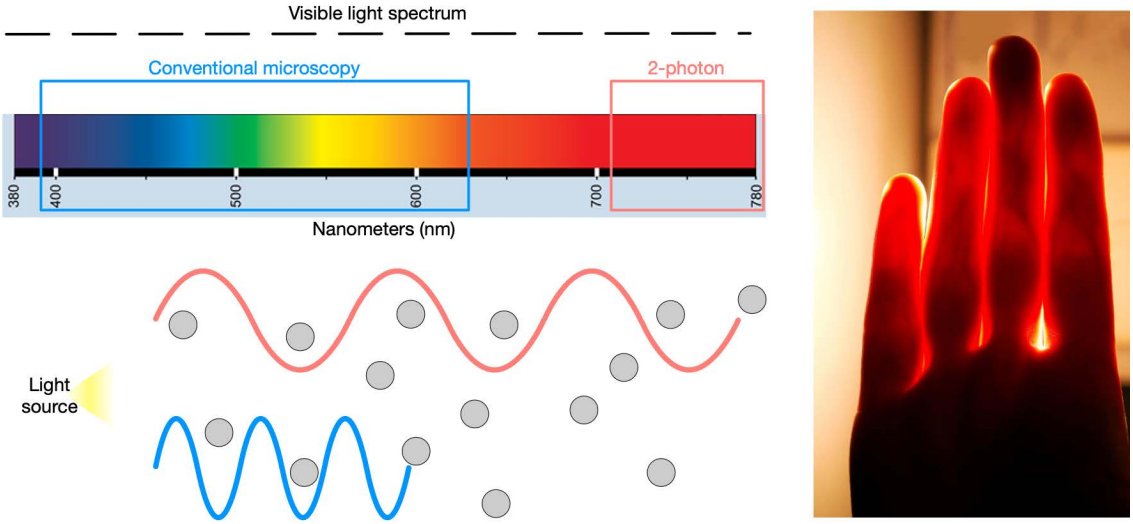

Figure 4

The physical basics of 2-photon microscopy. The light of the visible spectrum can be differentially applied in distinct microscopy techniques. 2-photon microscopy utilizes the near-infrared (NIR) light to excite the tissue. This approach has several advantages. The long NIR wavelength (red) can penetrate deeper into a tissue (illustrated by the gray dots) than a shorter wavelength. Moreover, the low energy level of the photons in the NIR-range accounts for less background fluorescence and photobleaching. As a curiosity, this physical phenomenon also explains why we only see a red-colored light if we shine a light beam through our hand. Images sourced from www.theengineer.co.uk and eyelighting.com respectively.

Together, these studies illustrate the potential of IVM to gain additional information about cell dynamics in the brain TME, with a temporal resolution that would have not been possible with standard methods. These studies also set the stage for advancing the longitudinal

investigation of the same animals over time, as described in this thesis, allowing one to observe the behavior of the cells of interest *in vivo* in their natural environment.

4.4.3 Non-invasive cellular monitoring

Although very powerful, IVM can only be applied to murine models. Investigating cellular dynamics and content in a non-invasive and longitudinal manner in glioma patients is considerably more challenging. Glioblastoma patients do not necessarily undergo a second surgery at recurrence, and it can therefore be difficult to assess changes in the TME composition over time. Importantly, many alterations in the TME are known to happen immediately after therapy, or later during the phase of tumor dormancy, where it is not possible to access the tissue [73, 75]. Moreover, due to tumor heterogeneity, the analysis performed on one piece of biopsy tissue might not necessarily recapitulate the composition of other parts of the same tumor. Ultimately, novel techniques allowing the global assessment of cellular dynamics at any given time-point during disease progression or in response to therapy would provide invaluable additional information, a challenge which I addressed in one of my thesis projects.

4.4.4 Nanoparticle-based non-invasive TAM imaging techniques

Among the different functions of macrophages, phagocytosis is a typical phenotypic trait of these cells [104]. Phagocytosis is by definition a process by which cells are able to engulf external materials, pathogens, or even other cells, and is therefore crucial in the previously mentioned roles of macrophages in regulating tissue homeostasis and immune response [104]. A common denominator of the different techniques that have been applied to image macrophages is the use of biocompatible nanoparticles (NP), which are phagocytosed and allow one to precisely identify these cells [105]. Moreover, NP allow the researcher to load a higher amount of detection/contrast agents, which facilitates the imaging of NP-uptaking cells compared to standard compound administration routes [106]. Different NP designs have been developed, with varying size and coating, which impact the tissue uptake as well as the more or less precise labelling of a particular cell population [105, 107]. Contrast agents are of course also an important component of NP, depending on the imaging technique utilized. For instance, iron-containing magnetic NP have been largely used for magnetic resonance imaging (MRI). Iron-NP have been shown to accumulate in macrophages and disturb the magnetic field upon imaging, thereby enabling their identification [105]. However, one of the challenges of magnetic agents is the correct interpretation of the negative contrast they

produce, which is very sensitive to tissue-related artefacts, such as the presence of tissue hemorrhaging. In the clinic, *in vivo* imaging techniques often rely on positron-emitted tomography (PET), which has the advantage of a relative fast whole body imaging [105]. This technique has been employed also to image macrophages, but accumulation of radioactive tracers limits the ability to perform repeated imaging [108, 109]. Lastly, fluorescently-labelled NP have also been used for clinically-relevant imaging techniques, such as endoscopy or intraoperative imaging [105].

4.4.5 Fluorine isotope 19 MRI

The clinical application of macrophage imaging requires biocompatible and safe agents, and an accurate interpretation of the resulting signal. One approach to visualize myeloid cell infiltration by MRI that fulfils these criteria, involves the use of perfluorocarbon-containing nanoparticles (PFC-NP) [110-112], such as perfluoro-crown-ether (PFCE) or perfluoro-tert-butylcyclohexane (PFTBH) [113, 114], mostly used in the cardiovascular field to date. PFCs are organic compounds highly rich in the fluorine isotope 19 (^{19}F). The ^{19}F isotope is not naturally present in the body, therefore permitting a precise signal detection and quantification upon injection of PFC-containing nanoparticles. Phagocytosing myeloid cells are prone to uptake PFC-NP and the signal has been used as a readout for inflammation-related processes [110-112]. Also, fluorine-based MRI has the main advantage of detecting a signal completely independent from the hydrogen signal, normally used for routine proton MRI and iron detection, thus avoiding potential artefacts. Therefore, ^{19}F MRI represents a precise technique to non-invasively longitudinally image myeloid cells *in vivo* and has also been shown to allow macrophage monitoring in a handful of non-brain tumor models, although several key technical and biological aspects have been minimally investigated [115, 116], which I have therefore addressed in this thesis.

4.5 Aims of the study

Seminal studies have shown the importance of the TME in regulating tumor progression and the response to therapy. Moreover, novel therapeutic approaches targeting TME components have been evaluated in experimental tumor models and in clinical trials, which have led to striking improvements in patient survival for certain types of cancer. Unfortunately, this is not the case for glioblastoma. Nonetheless, pioneering studies have shown the potential of therapeutic targeting of TAMs. Together, this work has set the stage for developing different

projects of my thesis, where I investigated additional levels of complexity of TAMs and the whole TME, including the temporal dynamics, various *in vivo* imaging approaches, and the impact of current and novel therapeutic strategies.

Specifically, I combined different cutting-edge imaging techniques, including ^{19}F MRI and 2p intravital microscopy, to image TAMs in preclinical glioma models. On the one hand, I investigated the technical feasibility of these techniques and fine-tuned the complex experimental setup to our immune-competent murine glioma models. On the other hand, I hypothesized that longitudinal imaging would allow unprecedented biological insights regarding these cell populations. The main focus was to investigate how these cells dynamically change during tumor progression and in response to treatment (IR or CSF1R inhibition), in order to gain insights into their temporal plasticity. Moreover, I also investigated how the genetic background of the tumor can impact these processes. Importantly, I combined both preclinical models and translationally relevant techniques, which could potentially facilitate the clinical application of our findings in the future. Lastly, I interrogated the potential of different therapeutic combinations to target TAMs (using an antibody targeting the extracellular ligand-binding domain of murine CSF1R, termed 2G2 antibody, developed by Roche Pharmaceuticals), the vessels (using the anti-angiogenic A2V antibody from Roche, targeting angiopoietin 2 (Ang2) and the vascular endothelial growth factor A (VEGF-A) signaling) and radiotherapy in preclinical trials with glioma models.

5. Summary of results and contributions

In the following Results Chapters 6.1-3, I present the findings of three projects I conducted during my thesis.

In the first study, we imaged TAMs in murine gliomas using ^{19}F MRI. This imaging approach allowed a non-invasive and longitudinal monitoring of the glioma TME, with potential translational applications. Moreover, we gained new insights into TAMs and tumor biology. The results are presented in a scientific article format, which we will submit for peer-review publication in the coming weeks. Personally, I was directly involved in all data acquisition and the majority of the analysis, the preparation and organization of all figures and the writing of the initial article draft. Importantly, I was supported and guided by my supervisor Prof. Johanna A. Joyce throughout the article preparation and writing, and she also contributed substantially to the editing and writing of this work. The initial raw MRI data which are part of Figures 1, S1, 5, S5, 6 and S6, were initially analysed by Dr. Ruud van Heeswijk, and I subsequently used the data for further analysis and the preparation of all graphs presented in the mentioned Figures. The RNAseq data and graphs presented in Figures 4A, 4B, 4C, S4A and S7C, were analyzed and prepared by Dr. Nadine Zangger.

In the second study, we devised and implemented a multi-modal 2-photon microscopy intravital imaging and MRI pipeline to longitudinally study the dynamics of the brain TME *in vivo*. We monitored mice harboring gliomas with different genetic drivers, and investigated how the TME changed during tumor progression and in response to anti-CSF1R therapy. By applying single cell analysis methods, including dimensionality reduction clustering, we were able to identify different subsets of cells with distinct migratory behaviors. The results are presented in a scientific article format, which we will shortly submit for peer-review publication. The surgical procedure and the monitoring of mice was established by my colleague Dr. Anoek Zomer. I actively performed the surgery and the imaging of the mice, the flow cytometry and immunofluorescence experiments, and data analysis, together with Dr. Zomer. After we analyzed all acquired images, the integration of the data into a single cell analysis pipeline was performed by Dr. Leon van Gurp. I prepared Figures 1, S1, S2, S3, S4. I actively wrote the manuscript together with Dr. Zomer, while being guided and supervised by Prof. Johanna A. Joyce, who also contributed substantially to the editing and writing of this work.

In the third study, I investigated different combinatorial strategies to therapeutically target the TME in glioma models, including CSF1R inhibition, radiotherapy and antiangiogenic treatment. Figure 4A, 4B and 4C were prepared by Dr. Stefan Bissinger. I generated, analyzed and prepared the figures for all other presented data. We do not expect that the results of this project will be published in a peer-reviewed article.

6. Results

6.1 Longitudinal and non-invasive monitoring of the spatial and temporal dynamics of glioma-associated macrophages following radiotherapy

Davide Croci [1,2], Klara Soukup [1,2], Sebastian Temme [3], Nadine Zangger [4], Anoek Zomer [1,2], Roberto Colotti [5], Vladimir Wischnewski[1,2], Ulrich Flögel [3], Ruud B. van Heeswijk [6*] and Johanna A. Joyce [1,2 * #]

[1] Department of Oncology, University of Lausanne, Lausanne, Switzerland
[2] Ludwig Institute for Cancer Research, University of Lausanne, Lausanne, Switzerland
[3] Institute for Molecular Cardiology, Universitätsklinikum Düsseldorf, Heinrich-Heine-Universität Düsseldorf, Düsseldorf, Germany
[4] Bioinformatics Core Facility, SIB Swiss Institute of Bioinformatics, Lausanne, Switzerland
[5] In Vivo Imaging Facility (IVIF), Department of Training and Research, University of Lausanne, Lausanne University Hospital, Lausanne, Switzerland
[6] Department of Radiology, Lausanne University Hospital, University of Lausanne, Lausanne, Switzerland.
* Co-senior authors

[#] Correspondence should be addressed to Johanna A. Joyce: johanna.joyce@unil.ch

---

6.1.1 Introduction

The brain tumor microenvironment (TME) is composed of malignant cells, tissue-resident and peripherally-recruited immune and stromal cells, along with non-cellular components, that collectively orchestrate tumor development and modulate the response to anti-cancer treatments [10, 117]. The precise composition and phenotypes of these cells in the brain TME is dictated by several parameters, including the intracranial or extracranial origin of the tumor, the genetic drivers of the cancer, and the type of therapeutic intervention [33, 34, 75].

The most aggressive primary brain tumors in adults are high-grade gliomas, also termed glioblastoma (GBM) [17]. Despite treatment with standard-of-care therapy, which includes surgical resection, irradiation (IR) and chemotherapy with the alkylating agent temozolomide (TMZ), median survival remains just 14 months following diagnosis, and the five-year survival is <5% [27]. Recent comprehensive analyses of the immune cell composition of diverse brain malignancies, including low- and high-grade gliomas, and brain metastases originating from different primary cancers, revealed disease-specific alterations in both immune cell abundance and functions [33, 34]. The TME of high-grade gliomas, for example, was found to be predominantly populated by tumor-associated macrophages (TAMs), comprising brain-resident microglia (MG) and monocyte-derived macrophages (MDMs) that were recruited from the peripheral circulation [33, 34]. Standard-of-care therapies, including IR and TMZ, have been shown to directly alter the TME composition, with pronounced effects on myeloid cells in particular [40, 75]. Indeed, time course analyses of IR response and recurrence in several murine glioma models (associated with different genetic drivers), showed that MDMs and MG were altered in both their relative abundance and phenotypes in response to radiotherapy [75]. Importantly, the combination of IR with different strategies to therapeutically target TAMs, including via colony stimulating factor-1 receptor (CSF-1R) inhibition to 're-educate' these cells, or depletion of MDMs specifically within the brain, resulted in a significantly prolonged survival of the animals [75]. CSF-1R inhibition, in particular, has been shown to be a promising and translationally relevant approach in several preclinical studies using models of diverse brain cancers [72, 73, 75, 76, 90, 118, 119] and clinical trials are ongoing in patients with advanced cancer, including gliomas (NCT02829723) [96]. The evolving TME was also recently assessed during growth of mesenchymal gliomas, and in response to TMZ chemotherapy, revealing important roles for bone marrow-derived neutrophils, which were phenotypically altered with disease progression [40].

Dynamic monitoring of the cells of the brain TME is therefore crucial in order to fully understand the disease biology and response to treatment. While the analysis of TAMs can be achieved by a multitude of experimental techniques in preclinical models, TAM quantification in patients currently relies mainly on histological staining of tumor biopsies. This approach has several limitations, including the fact that biopsies only represent a small portion of the entire tumor and thus do not necessarily capture the full tissue heterogeneity. Moreover, surgical access to the brain is challenging, which does not facilitate frequent and repeated sampling to study cellular dynamics over time. It is therefore essential to develop new technological strategies that will enable the non-invasive and longitudinal monitoring of multiple aspects of the disease, including changes in the TME composition.

Magnetic resonance imaging (MRI) is a widely used and indispensable imaging modality in neuro-oncology, where it enables important decision-making steps, including tumor diagnosis, a precise guidance for planning surgery and targeted irradiation, and also for monitoring the subsequent response to treatment [120]. Historically, MR images have been primarily used for a qualitative and objective assessment of the tumor by clinicians. However, recent neuroimaging advances have contributed to the development of quantitative MRI techniques [121-123], which have the potential to transform the interpretation and application of imaging results into routine clinical practice. Nonetheless, research on MRI-based biomarkers is still in its early stages, with the major challenges including technical, biological and clinical validation in order to implement robust imaging methods that will enable the acquisition of multiparametric information, thereby revealing tissue heterogeneity and assisting in revealing and executing appropriate therapeutic interventions [120].

The clinical application of macrophage imaging requires safe and biocompatible agents, and an accurate interpretation of the resulting signal. MRI-based non-invasive techniques represent a potentially powerful strategy to visualize myeloid cells [105, 124]. Fluorine isotope 19 MRI (^{19}F MRI) takes advantage of perfluorocarbon-containing nanoparticles (PFC-NP), such as perfluoro-crown-ether (PFCE) or perfluoro-tert-butylcyclohexane (PFTBH) [113, 114], and has been mostly used in the cardiovascular field to date [110, 111]. PFCs are organic compounds that are highly enriched in the fluorine isotope 19 (^{19}F). Given that the ^{19}F isotope is not naturally present in the body, this enables a precise signal detection and quantification upon the injection of PFC-NP. Myeloid cells have a high capacity for phagocytosis, and are thus prone to take up PFC-NP in a directed manner [125, 126], and the resulting signal has been used as a readout for inflammation-related processes [110, 111]. Moreover, fluorine-based MRI has the important advantage of detecting a signal that is completely independent from the hydrogen signal normally used for routine proton MRI (^{1}H MRI), thus avoiding potential imaging artefacts. Due to the critical role of TAMs in brain tumor biology, we decided to investigate ^{19}F MRI as a strategy to non-invasively longitudinally image and monitor TAMs *in vivo* in experimental mouse models of gliomagenesis and brain metastasis. In this study, we report the successful tracking of different TAM populations with integrated cellular, spatial and temporal resolution, which has allowed us to reveal novel biological insights into the dynamic evolution of the TME. This research also serves to highlight the potential of ^{19}F MRI to ultimately complement, or perhaps even replace, the existing histological-based assessment of TAMs in patients.

6.1.2 Results

Multiparametric magnetic resonance imaging (MRI) detects a tumor-restricted perfluoro-crown-ether-containing nanoparticles (PFCE-NP) accumulation in glioma- and brain metastasis-bearing mice.

We began by assessing whether multiparametric ^{1}H and ^{19}F MRI can be used in conjunction for molecular imaging of preclinical brain tumor models. We first analyzed a genetically-engineered mouse model (GEMM) of gliomagenesis, in which nestin-positive progenitor cells are engineered to overexpress the oncogenic platelet-derived growth factor-β (PDGF-β) by taking advantage of the transgenic RCAS-tva delivery strategy [36]. High-grade gliomas develop in a highly penetrant manner when this model is crossed into an *Ink4a/Arf* tumor suppressor-deficient background (termed PDG-Ink4a/Arf KO GEMM) [36, 66, 73, 75, 127]. Tumor-bearing mice were injected with 10 µL/g of a 10% PFCE-NP emulsion and imaged 48h later using a clinical 3T MRI (Prisma, Siemens) equipped for both ^{1}H and ^{19}F sequential imaging (Fig. 1A). We detected a robust ^{19}F signal and PFCE accumulation inside the gliomas which were anatomically defined by standard ^{1}H MRI (Fig. 1B). By contrast, the contralateral healthy brain, as well as the brain of control non-tumor bearing mice, did not show any ^{19}F signal (Fig. S1A). We also observed ^{19}F signal in the liver (Fig. 1A and S1A), in agreement with a previous description of its function in PFCE uptake and excretion [113]. Interestingly, the ^{19}F signal-to-noise ratio (SNR) quantification inside the tumor area showed a broad distribution of the ^{19}F SNR values, potentially indicating a heterogeneous accumulation of the PFCE-NP (Figure S1B). Of note, brain tumors can display diverse anatomical features by ^{1}H MRI, which may indicate functionally discrete regions [128]. We therefore analyzed the extent of the ^{19}F distribution in detail, and found that the proportion of the total tumor volume covered by ^{19}F signal varied considerably and showed distinct patterns in different animals (Fig. 1C and fig. S1C).

We next asked whether this imaging strategy could also be applied to other brain cancer models, and evaluated the ^{1}H-^{19}F MRI pipeline in a breast-to-brain metastasis (BrM) mouse model, termed PyMT-BrM3. We generated the PyMT-BrM3 cell line from the sequential *in vivo* selection of a metastatic cell line that was originally derived from the MMTV-PyMT mammary tumor model (BL/6 background). Intracardiac injection of PyMT-BrM3 cells in BL/6 mice results in the seeding and outgrowth of multiple lesions throughout the brain parenchyma. By comparison with the PDG-Ink4a/Arf KO gliomas, the ^{19}F coverage of these metastatic lesions was low, as reflected by the lower PFCE concentration in the 99LN-BrM model (Fig. S1D and S1E). Nonetheless, in both models we found a positive correlation

between the ^{19}F signal and tumor volume as defined by ^{1}H MRI (Fig. 1D and S1F). Together, these results demonstrate that multiparametric MRI is technically feasible in different models of brain cancer and can be used to reveal valuable molecular information in addition to conventional ^{1}H MRI. The heterogenous ^{19}F pattern observed in the glioma and BrM models, and the higher total amount of PFCE in larger tumors, suggested that a specific cellular composition as well as functionally distinct regions within the tumor could potentially underly the ^{19}F signal distribution, which we then investigated in further detail.

PFCE-NP accumulate in tumor-associated microglia and macrophages in gliomas enabling their specific imaging by ^{19}F MRI.

^{19}F MRI has been utilized in different models of inflammatory disease, where myeloid cells at the site of inflammation have been shown to take up injected PFC-NP [111, 115, 116]; however, this powerful imaging approach has not yet been widely applied to assess the dynamics of cancer-associated inflammation. Brain tumor development and progression can result in heterogenous breakdown of the blood-brain barrier (BBB), facilitating the entry of peripheral immune cells, mainly of myeloid origin, which along with the various brain-resident cells contribute to form a complex and diverse brain tumor microenvironment (TME) [10, 33, 34]. We therefore assessed whether the ^{19}F signal we observed in the PDG-Ink4a/Arf KO GEMM was the result of PFCE-NP uptake by any specific cellular population. To do so, we injected glioma-bearing mice with fluorescent rhodamine-labelled PFCE-NP (Rhodamine-PFCE-NP), allowed the NP to circulate for 24 hours, and analyzed the cellular composition of the tumors by flow cytometry at the end of the experiment. As previously described for this mouse model [36, 66, 73, 75, 127], we observed a high infiltration of myeloid cells in gliomas (Fig. S2A), which is similar to analyses of patient samples [33, 34]. Myeloid cells accounted for the majority of the Rhodamine-PFCE-NP^{+} cells (Fig. 2A and S2B), in line with previous reports showing an accumulation of PFCE-NP mainly in this population in animal models of arteriosclerotic plaques, head and neck carcinoma, and mammary tumor and lung metastasis [111, 115, 116]. TAMs, together with a smaller proportion of monocytes, constituted the Rhodamine-PFCE-NP^{+} myeloid pool (Fig. 2B and 2C). Importantly, while we also detected Rhodamine-PFCE-NP in some non-immune cells, the median fluorescence intensity (MFI) of rhodamine was substantially higher in both resident microglia (MG) and recruited monocyte-derived macrophages (MDMs) (Fig. 2D), the two major cellular subsets constituting TAMs, indicating a substantial enrichment of nanoparticles specifically in these cells.

We then assessed the proportion of each different cell type that was Rhodamine-PFCE-NP^{+} (Fig. 2E, S2C and S2D), and found that only a small percentage of the different myeloid cell

types accumulated the Rhodamine-PFCE-NP. TAMs had a higher frequency of Rhodamine-PFCE-NP$^+$ cells compared to monocytes (Fig. 2E), while in cells of lymphoid or non-immune origin the uptake was generally low (Fig. S2D). Interestingly, CD31$^+$ endothelial cells showed a slightly higher frequency of Rhodamine-PFCE-NP$^+$ cells, which could indicate a role for the vasculature in the distribution of NP. Given that the TME composition can change dynamically over time, as a consequence of the infiltration of newly-recruited immune cells from the periphery, we also assessed the uptake of Rhodamine-PFCE-NP in myeloid cells in the blood and the bone marrow. However, we did not find a significant accumulation of the compound in these settings (Fig. S2E), and thus consider it unlikely that cells recruited *de novo* from outside the brain would substantially impact the ^{19}F signal in the days following PFCE-NP injection. Together, we were able to identify TAMs as the major cellular contributor to the pool of Rhodamine-PFCE-NP$^+$ cells, showing both a higher accumulation and MFI signal. Therefore, we conclude that TAMs are the major source of the ^{19}F signal detected by MRI.

PFCE-NP accumulate in proximity to dysmorphic vessels.

MR imaging revealed a ^{19}F signal only in the tumor and not in the contralateral healthy brain, suggesting an inflammatory milieu specifically in the diseased tissue area. While the BBB protects the brain from entry of exogenous substances and pathogens under normal homeostasis, thereby constituting a potential hurdle for PFCE-NP distribution, it can be compromised in brain malignancies [4]. Given that only a small percentage of cells showed accumulation of the Rhodamine-PFCE-NP (Fig. 2E and S2D), and the heterogenous ^{19}F signal within the tumor (Fig. 1C), we reasoned that the abnormal nature of the brain tumor vascular network could impact PFCE-NP distribution. We therefore induced green-fluorescent protein (GFP)$^+$ PDG-Ink4a/Arf KO gliomas, enabling precise visualization of the tumor mass, and investigated the distribution pattern of Rhodamine-PFCE-NP. To image the vasculature, we injected DyLight649-fluorescent lectin intravenously and allowed it to circulate for 5 minutes. As the Rhodamine-PFCE-NP signal can be sensitive to degradation post-tissue processing [129], we imaged fresh 425 μm-thick tissue slices *ex vivo* with a 2-photon microscope, immediately after harvesting and slicing of the brain. We observed a heterogenous pattern of NP accumulation, whereby distinct regions within the same tumor showed a differential distribution of the rhodamine signal (Fig. 3A).

We reconstructed the imaged slices using *Imaris* software and first assessed whether the accumulation was similar to the flow cytometry results discussed above (Fig. S3A). Indeed, we found that only a minor proportion of the rhodamine$^+$ foci were also GFP$^+$ (indicating tumor cells) (Fig. S3B), and similarly, only a small percentage of GFP$^+$ cells showed a rhodamine signal (Fig. S3C). We then examined how the tumor vasculature might impact the degree of

accumulation of the Rhodamine-PFCE-NP. Image reconstruction using *Imaris* enabled a multi-parametric analysis of the tumor vessels, including vessel dendrite morphology, orientation and branching (Fig. S3D). A principal component analysis of all vascular morphological parameters indicated the independent clustering of Rhodamine^{HIGH} areas with respect to the healthy brain parenchyma, adjacent to the tumor (Fig. 3B). Together, these analyses revealed a heterogenous vascular morphology within the tumor, ranging from "healthy brain-like" vessels to a completely dysmorphic vasculature, which precisely correlated with the amount of Rhodamine-PFCE-NP accumulation.

To extend these results *in vivo*, we sought to longitudinally assess the kinetics of Rhodamine-PFCE-NP distribution by intravital microscopy (IVM) in living animals. We therefore induced tumors in the GFP$^+$ PDG-Ink4a/Arf KO GEMM, where a cranial imaging window (CIW) was surgically implanted in the skull at the site of tumor induction (see Results Chapter 2). Following tumor detection by conventional ^{1}H MRI, mice were imaged by 2-photon microscopy enabling longitudinal live imaging within the GFP$^+$-tumor area precisely below the CIW (Fig. 3C). Immediately after injection of the Rhodamine-PFCE-NP, we analyzed the dynamics of the Rhodamine signal inside the blood vessels, which were highlighted by the circulating fluorescent nanoparticles (Fig. 3D and S3E). We found that the rhodamine signal was almost completely cleared from the blood circulation 6 hours after NP injection. In line with our results above showing a heterogenous pattern of Rhodamine$^{LOW/HIGH}$ regions, we were able to detect a clear signal directly below the CIW in 1 out of 5 mice that were imaged (Fig. 3D).

Given the higher NP uptake in regions with dysmorphic vessels, we next sought to address whether the NP were subsequently distributed effectively into the tumor mass. We therefore analyzed the distance of the Rhodamine$^+$ foci to the vessels (and GFP$^+$ cancer cells to the vessels) in tumor-bearing brain slices and found that the NP accumulation occurred in proximity to the vasculature (Fig. 3E). GFP$^+$ cancer cells with a detectable rhodamine signal were also closer to the vessels (Fig. S3F). Since the positioning of TAMs relative to the vasculature affects their phenotype and oxidative metabolism [130], we asked whether the specific distribution pattern of Rhodamine-PFCE-NP$^+$ TAMs could reflect a precise subpopulation. We used fluorescence-activated single cell sorting (FACS) to collect Rhodamine-PFCE-NP$^+$ and Rhodamine-PFCE-NP$^-$ TAMs respectively and performed RNA sequencing (RNA-seq) (Fig. S4A). Interestingly, in line with their perivascular location, gene-set enrichment analysis (GSEA) revealed a higher oxidative phosphorylation activity in the Rhodamine-PFCE-NP$^+$ population (Fig. 4A), consistent with an altered metabolism. GSEA network analysis also showed several mitochondrial components to be enriched (Fig. 4B), and central enzymes of the tricarboxylic acid (TCA) cycle were up-regulated in Rhodamine-PFCE-

NP^+ TAMs, including *Dlat*, *Dld*, *Idh1*, *Idh2* and *Phda1* (Fig. 4C). To validate the RNA sequencing results, we stained glioma tissue sections by immunofluorescence (IF) for the macrophage marker CD68 and the metabolic enzyme IDH2 (Fig. 4D). We identified two TAM subpopulations: a $IDH2^+$ subset in proximity to $CD31^+$ endothelial cells and a larger proportion of $IDH2^-$ TAMs which were more distant from the vessels (Fig. 4E and S4B). Moreover, $IDH2^+$ $CD68^-$ cells tended to be closer to the vessels, indicating a broad effect of the vasculature proximity on oxidative metabolism of the cells (Fig. S4C), potentially related to a higher availability of oxygen [130]. Together, these results indicate that Rhodamine-PFCE-NP^+ TAMs are characterized by an oxidative metabolic signature, including *Idh2* upregulation, and are localized in perivascular niches.

^{19}F MRI allows the non-invasive and longitudinal monitoring of TAM dynamics in gliomas following irradiation (IR) treatment.

We next asked whether ^{19}F MRI could be used to monitor changes in the TME following therapeutic intervention in a non-invasive and longitudinal manner. IR is part of the standard of care therapy for glioma patients [27], and has been shown to dynamically alter the composition of the glioma TME [69, 75]. Notably, the overall abundance and phenotypes of TAMs have been shown to be substantially impacted by IR treatment, in addition to alterations in the relative proportions of recruited MDMs versus resident MG [75].

We analyzed TAM dynamics after IR treatment (single dose of 10 Gy) (Fig. 5A). Consistent with previous reports employing fractionated IR [75], we found a transient increase in the abundance of all TAMs following single dose IR, with a peak at 7 days after treatment (Fig. 5A). PFCE-NP uptake occurred in a subset of these TAMs, and we thus sought to address whether this population could be indicative and representative of general TAM dynamics following IR. We injected glioma-bearing mice with a single dose of PFCE-NP, which has been previously reported to be slowly cleared [113], in order to specifically track the dynamics of the initial TAM pool only. Mice were then imaged by ^{1}H and ^{19}F MRI, to determine the baseline PFCE concentration and tumor volume before IR, and then imaged weekly until tumor recurrence (Fig. 5B).

Single dose IR treatment led to an initial tumor debulking followed by a quiescent phase, and eventually all tumors relapsed (Fig. 5C). We analyzed the short-term ^{19}F dynamics in the 7 days following treatment. We quantified the PFCE concentration over time as a readout of TAM abundance and found a significant increase 7 days after IR (Fig. 5D), consistent with the observed abundance of TAMs by IF staining (Fig. 5A). Normalization of the tumor PFCE

concentration to the liver PFCE concentration, as a measure of potential compound clearing, confirmed the increase following IR (Fig. S5A). The absolute compound concentration (measured as the total PFCE amount normalized to the ^{1}H tumor volume) also increased after treatment (Fig. S5B). Importantly, the PFCE concentration was stable in the liver over the full time course, indicating a slow clearing of PFCE (Fig. S5C and S5D), consistent with previous reports [113]. Moreover, we did not observe changes in the amount of PFCE inside the tumor (Fig. S5E), indicating a cellular labelling only after compound administration, in line with our results from flow cytometry and IVM that showed no peripheral PFCE-NP uptake and a rapid clearance from the blood stream (Fig. S2E and S3E). Overall, these results showed that ^{19}F MRI can be used to track the initial TAM dynamics at 7 days post-IR treatment.

We also investigated whether the ^{19}F changes over the full trial length could be indicative of the long-term TAM dynamics we observed by IF staining at different timepoints (Fig. 5A), where overall TAM abundance returns to the baseline level at tumor recurrence. First, we addressed if the tumor PFCE concentration was returning to the initial levels (Fig. S5F). We found that the tumor PFCE concentration indeed tended to decrease in the subset of mice that could be imaged until 28 days post-IR, although this was not statistically significant (Fig. S5F). Importantly, one needs to account for a decreased total PFCE amount in the tumor, probably related to local clearing, that consequently affects the PFCE concentration (Fig. S5G). Together, these results showed that after an initial precise monitoring of the IR-mediated TAM increase, long-term ^{19}F MRI did not enable a comprehensive assessment of TAM dynamics over the full time course of the trial, which we then sought to address further.

Multispectral ^{19}F MRI identifies spatial- and temporally-distinct cellular populations in IR recurrent tumors.

To evaluate TAM changes during the whole trial length, we began by analyzing the variation of the ^{19}F signal volume (Fig. 6A and 6B). After an initial volume reduction followed by a quiescent phase, we never observed an increase in ^{19}F signal volume as was clearly evident for ^{1}H MRI (Fig. 5C and 6A). This could potentially indicate the existence of different TAM clusters at recurrence (Fig. 6B). We therefore analyzed the composition of TAMs in untreated and IR-recurrent PDG-Ink4a/Arf KO gliomas in Cx3cr1:CreERT2-IRES-YFP;Rosa26:lslTdTomato mice that allow one to distinguish MG (YFP^{+}/tdTomato^{+}) and MDMs (YFP^{+}/tdTomato^{-}) (termed CX3CR1 lineage tracing model) [66, 98], and by IF staining of the pan-macrophage marker Iba1 and the MG-specific marker P2RY12 (Fig. 6C and S6A). We observed a shift in the major TAM populations between untreated and IR-recurrent tumors, consistent with previous findings in the context of fractionated IR [75]. While MG are the

predominant TAM population in untreated gliomas, at recurrence the tumor is substantially infiltrated by peripheral MDMs, which are unlikely to be detected by ^{19}F MRI based on the lack of peripheral cell labelling by PFCE-NP (Fig. S2E). As such, we reasoned that an initial PFCE-NP^{+} TAM population (likely MG predominantly) remains in the residual tumor bed following IR treatment and forms a discrete TAM cluster, while the recurrent outgrowing glioma is infiltrated by new (PFCE-NP-unlabeled) myeloid cells originating from the periphery.

Therefore, in order to visualize the integrated cellular, temporal and spatial complexity of TAM dynamics until recurrence, we decided to investigate the potential use of multispectral ^{19}F MRI [131]. Glioma-bearing mice were injected with a single dose of PFCE-NP (10 µL/g of a 10% PFCE-NP emulsion) before IR (single dose of 10 Gy), and monitored by conventional ^{1}H MRI until glioma recurrence. Mice were then injected with a second, distinct perfluorocarbon-containing nanoparticle (Perfluoro-tert-butylcyclohexane (PFTBH)-NP, 3.3 µL/g of a 60% PFTBH-NP emulsion), which has been shown to emit a fluorine resonance peak at a distinct frequency than PFCE, and a final ^{1}H and ^{19}F MRI was performed (Fig. 6D and S6B) [114]. Interestingly, we found that the ^{19}F signal from PFTBH-NP covered a region of the tumor that did not show signal from the original PFCE-NP (Fig. 6E and 6F). Moreover, the cumulative ^{19}F signal volume was significantly higher than the PFCE-NP ^{19}F signal volume alone, showing a volumetric dynamic which was similar to conventional ^{1}H MRI monitoring, where larger tumor volumes were detected at recurrence (Fig. 5C). Interestingly, while the ^{19}F SNR of the two compounds was similar in the liver, it was higher for PFCE in the tumor, possibly as a consequence of the initial PFCE concentration after IR (Fig. S6C and S6D). Accordingly, we concluded that TAMs not only shift their relative proportion between MG and MDMs following IR treatment, but ^{19}F MRI revealed that their spatial organization could potentially differ in untreated and recurrent gliomas, which we then investigated further.

The distribution pattern of TAMs within tumors changes following IR treatment.

We further explored how the spatial and temporal distribution of TAMs changes following IR treatment by analysis of tissue sections. IF staining of PDG-Ink4a/Arf KO gliomas in the CX3CR1 lineage tracing model showed a different spatial distribution of TAMs between untreated and recurrent tumors, where substantial MDM-rich areas could be observed specifically at recurrence (Fig. 7A). In order to quantify this observation, we analyzed the average distance between MDMs and MG (Fig. 7B), and found that MDMs were significantly more distant from MG in recurrent tumors compared to untreated gliomas. To assess a potential mutual exclusion between the two cell types spatially, we analyzed the frequency of MG in a region of interest defined around MDMs (termed MDM-ROI) in untreated and recurrent

tumors (Fig. 7C), and found a significantly lower abundance of MG in MDM-rich areas at recurrence (Fig. 7D). Collectively, these results showed that while MDMs and MG are generally evenly distributed within untreated tumors, at recurrence we observe the emergence of clusters of distinct TAM populations, as indicated by the ^{19}F MRI analyses.

While these analyses revealed different spatial patterns of TAMs in untreated versus IR-recurrent tumors, it did not enable the temporal discrimination of the sequence of cell infiltration throughout the experimental time course. Given that IR has been reported to lead to hemolysis and hemoglobin release in other contexts [132, 133], we assessed whether this process is also evident in gliomas following IR, and if iron uptake by specific cells could thereby mark them in a temporal manner. We therefore stained PDG-Ink4a/Arf KO glioma sections with Prussian Blue (PB) to visualize iron deposition. While there were only rare PB$^+$ cells in untreated tumors, we found a peak of PB$^+$ cells at 7 days after IR, which then somewhat decreased in recurrent tumors (Fig. 7E). To identify the cellular source of the PB signal, we multiplexed PB and IF staining (Fig. S7A) and found MDMs to be the main cell type accumulating iron, while no PB$^+$ MG were observed (Fig. S7B). To confirm these findings, we analyzed a published gene expression dataset of MG and MDMs in untreated, 5 days irradiated and IR-recurrent gliomas [75]. GSEA indeed showed increased iron uptake-related processes at 5 days post-IR and at recurrence specifically in MDMs, but not in MG, thus supporting our observation of an increased frequency of PB$^+$ cells following IR treatment (Fig. S7C). Together, these results revealed the emergence of a temporally-defined PB$^+$ population (mainly MDMs) only after IR.

We then investigated if the PB$^+$ cells remained in proximity to one another at recurrence. We analyzed their frequency in the whole tumor area as well as in a defined ROI around PB$^+$ cells (termed PB$^+$ ROI) (Fig. S7D). We found that the frequency of PB$^+$ cells in the PB$^+$ ROI was higher in recurrent than untreated tumors (Fig. 7F), indicating that these cells cluster together during tumor outgrowth and form a spatially defined niche, despite their overall low abundance (Fig. 7E). In sum, we showed that in recurrent tumors there is a higher infiltration of MDMs which localize distally from MG. PB$^+$ cells (mainly MDMs) are enriched after IR treatment and also cluster together in larger recurrent tumors. These results indicate that different TAM populations, in addition to dynamically changing their relative abundance, also vary in spatial distribution in a time-dependent manner, as suggested by our multispectral ^{19}F MRI data (Fig. 7G).

6.1.3 Discussion

MRI is indispensable in neuro-oncology practice, yet standardized and robust MRI-based biomarkers are currently sparse [120]. Recent clinical studies demonstrated the potential of MRI in predicting the response to antiangiogenic treatment in pediatric and adult brain tumors [134, 135]. Quantitative characterization of vascular properties is a common MRI application in the image of brain tumors, due to the ability of the contrast agent gadolinium to penetrate and enhance those tumor regions with a disrupted BBB [136, 137]. Nonetheless, the vasculature is just one component of the complex brain TME [10]. Despite the high abundance of TAMs in gliomas [33, 34], and their importance in establishing a immunosuppressive TME [77], with potential direct consequences on the effectiveness of novel immunotherapeutic strategies in patients [50], their abundance and distribution can only be rarely assessed following an invasive surgical procedure to remove the tumor.

In this study, we harnessed the power of ^{19}F MRI in preclinical glioma and brain metastasis models to show the technical feasibility of longitudinally and non-invasively imaging small inflamed brain tumors with a clinical machine at high resolution. These results highlight the translational potential of this strategy to expand the MRI repertoire used to classify diverse brain malignancies [121]. Interestingly, we indeed found substantial differences in the ^{19}F signal distribution between the preclinical glioma and brain metastasis models, underlining a potential relevance to distinguish these two brain tumor types. This finding is supported by the lower overall TAM abundance observed in both preclinical models and human brain metastasis tissues [33, 34, 138], which can account for the observed lower accumulation of PFCE-NP in the brain metastasis model.

To date, the application of PFCs to image immune cells in cancer has largely relied on the *ex vivo* labelling of specific cell types in the context of monitoring cell-based therapies, such as adoptive T-cell transfer and DC-based cancer vaccination [139, 140]. *In vivo*, only a handful of studies have explored the distribution of injected PFC-NP to image myeloid cells [115, 116, 141], and the sub-cellular composition of the labelled myeloid cells has been minimally investigated [142]. Moreover, the extent of brain microenvironment heterogeneity has been underscored by recent single cell analyses, with potential translational implications [143]. In this study, we found that the myeloid-specific labelling with PFCE-NP in preclinical glioma models included several cell subpopulations, mostly comprising resident MG and peripheral MDMs. Importantly, both populations were labelled directly in the tumor and were not replenished by newly infiltrating cells, which were shown to not uptake PFCE-NP. Indeed,

gene expression analysis of Rhodamine-PFCE-NP$^+$ TAMs revealed the enrichment of specific metabolic signatures, which may impact their phenotypic and functions [130, 144], and was correlated with their presence in the perivascular niche. These findings emphasize the importance of a detailed characterization of the PFCE-up-taking TAM subsets, and highlight the benefit of future studies exploring the role of additional macrophage populations, including CNS border-associated macrophages [64].

Our data also showed that TAMs are the predominant, though not the sole cell population up-taking PFCE-NP. Non-immune cells were the second largest PFCE-NP$^+$ cluster, including endothelial cells, thereby showing a potential active role of these cells in the trafficking of the NP *in vivo*. Uptake in other non-immune cells included a small proportion of cancer cells. Indeed, rapidly dividing cells have been shown to actively uptake nanoparticles by macropinocytosis [145, 146]. Moreover, brain-resident astrocytes also have phagocytic ability [147]. Thus, future studies will be important to further explore the precise ontogeny of the non-immune cell types up-taking the NP, as well as the underlying phagocytic mechanism. While multiple studies demonstrated a clear role for phagocytosis and macropinocytosis in PFC-NP uptake *in vitro* [125, 126], further research is required to better understand this process *in vivo*. As such, the IVM method presented in this study might be a valuable approach to address these open questions and aid in designing cell type-specific NP to selectively target only the population of interest.

TAM content and composition is in constant flux and adaptation during tumor growth and in response to therapies [40, 75]. In this context, ^{19}F MRI represents a powerful strategy to temporally and spatially track distinct inflammatory dynamics in IR-recurrent tumors by applying multispectral compound imaging with PFCE-NP and PFTBH-NP. This allowed us to shed light on the presence of different TME niches not only before treatment and at recurrence, but also during tumor dormancy, which is known to be a key step in the emergence of TAM-mediated resistant mechanisms in response to different therapeutic interventions [73, 75], although a non-invasive clinical assessment of TAMs in dormant tumors has not been achievable to date. Thus, our analyses revealed that gliomas not only shift the ratio of MDM:MG in response to IR [75], but also differ in the spatial distribution of these cells. This finding has relevance for understanding the complexity of the brain TME, by integrating critical temporal and spatial variables. In this context, it will be important to assess if these TAM-defined niches respond differently to specific treatments, for example. Moreover, we also identified an IR-triggered iron-rich TAM population that occupies a specific niche from 7 days after therapy until recurrence. Iron is an essential metal micronutrient and its metabolism in tumors is regulated by TAMs, with a direct impact on tumor growth and on the immune

response of macrophages themselves [148]. Interestingly, high iron influx in macrophages has been associated with an antitumorigenic phenotype of these cells [148]. Thus, future single cell analyses will be of interest to fully understand the alterations and adaptation of TAMs in response to IR.

Nanoparticle-based drug delivery and anti-angiogenic treatments have been widely studied in brain tumors. The first, to improve the delivery of compounds with a poor pharmacokinetic profile, can lead to continuous drug release and potentially reduce drug side-effects [106]. The second, can normalize the vasculature and thereby result in improved drug delivery [4]. The unique structure of the BBB, however, requires a careful and meticulous investigation of the effect of vascular integrity on drug delivery [4]. Vessel normalization has been shown to enhance the efficacy of chemotherapeutic agents in preclinical glioma models [149]. However, a study of multiple pediatric brain tumor models, driven by distinct oncogenic alterations, revealed a differential impairment of the BBB, which resulted in effective chemotherapy delivery only in medulloblastoma with disrupted vessels [150]. Our findings in this study were able to connect the heterogeneity of the vasculature with the extent of PFCE-NP accumulation. The NP only accumulated in areas of dysmorphic vessels, highlighting the notion that vessel normalisation in brain tumors needs to take into consideration the type and size of any additional combinatorial treatments. Additionally, ^{19}F MRI can represent a potential MRI-based method to gain important information regarding the extent and heterogeneity of BBB leakage, which is conventionally assessed using gadolinium at present.

In conclusion, we propose ^{19}F MRI as a powerful strategy to non-invasively and longitudinally explore brain TME composition and functionality. In the future, it will be of great interest to assess its predictive role on brain malignancy-related processes, such as pseudo-progression, pseudo-regression, and necrotic inflammation to inform the clinical management of the disease, as well as its ability to predict therapy response to targeted treatments, including in other CNS diseases.

6.1.4 Acknowledgments

We thank members of the Joyce lab for insightful discussion, Lucie Tillard and Dr. Mara Kornete for technical support. We are grateful to the In Vivo Imaging Facility and the Flow Cytometry Facility at the University of Lausanne for assistance and advice, in particular Dr. A. Benechet and Danny Labes. This research was supported in part by the Swiss Cancer

Research Foundation (KFS-3390-08-2016; KFS-5280-02-2021), Charlie Teo Foundation, Ludwig Institute for Cancer Research, and University of Lausanne (to JAJ).

6.1.5 Materials and Methods

Study design

The aim of this study was to longitudinally and non-invasively monitor TAM dynamics in response to irradiation with ^{19}F MRI. The sample size for longitudinal imaging trials (n=8 to 15 mice) was based on previous experience with these glioma models [66, 72, 73, 75] and planned using the statistical program OpenEpi [151]. ^{19}F signal monitoring was the primary outcome of these experiments. These data were supported by tissue staining, flow cytometry, *ex vivo* and *in vivo* imaging and RNA sequencing to further understand the kinetics and distribution of the nanoparticles and the underlying biological mechanisms of the MRI-based observations. The choice of defined individual time points for these analyses was based on previously published data on nanoparticle kinetics [113, 129] and sample size (n=3 to 8) was defined as described above. Age-matched mice were assigned to experimental cohorts based on matching tumor volumes, and data presented include all outliers. Investigators were not blinded when monitoring the animals. Blinding was applied during all data analysis. Biological replicates are indicated in the figure legends by *n*, together with the statistical analysis applied. Two or more independent trials or experiments were performed. All animal studies were reviewed and approved by the Institutional Animal Care and Use Committees of the University of Lausanne and Canton Vaud, Switzerland.

Animals, cells and tumor models

Animals

The Nestin-Tv-a;*Ink4a/Arf*$^{-/-}$ mouse line has been previously described [152] and was generously provided by Dr. Eric Holland, USA. *Cx3cr1*:CreER-IRES-YFP mice (C57BL/6 background; Jackson Labs) were crossed with Rosa26:lsl-TdTomato reporter mice (C57BL/6 background; Jackson Labs), and with Nestin-Tv-a;*Ink4a/Arf*$^{-/-}$mice [66]. For the Cx3cr1:CreER-IRES-YFP Rosa26:lsl-TdTomato lineage tracing system, 3 to 4 week-old mice were injected twice, 48 hours apart, intraperitoneally with 1 mg of tamoxifen citrate (Sigma-Aldrich) dissolved in sunflower seed oil (Sigma). Mice were used for intracranial injection surgery 3 weeks after tamoxifen administration (see “Glioma model” section below). All mice were bred within the University of Lausanne animal facilities, and all animal studies were first

approved by the Institutional Animal Care and Use Committees of the University of Lausanne and Canton Vaud, Switzerland.

Cells

For glioma induction, DF1 chicken fibroblasts were obtained from ATCC. RCAS vectors expressing PDGFB-HA or PDGFB-HA-SV40-GFP were kindly provided by Dr. Tatsuya Ozawa and Dr. Eric Holland, USA [37, 153]. DF1 cells were transfected with the RCAS vectors using FuGENE 6 (Promega) according to the manufacturer's instructions. PDGFB-HA-SV40-GFP DF1 cells were sorted by flow cytometry to collect GFP^+ cells and subsequently culture a stable GFP-positive glioma cell line. All cell lines were cultured in DMEM (Life Technologies) supplemented with 10% fetal bovine serum (Life Technologies) under standard conditions. For brain metastasis induction, the murine parental 99LN cell line was derived from a metastatic lymph node lesion that arose in the MMTV-PyMT (murine mammary tumor virus; Polyoma middle T antigen) breast cancer model (C57BL6/J background) [154]. This cell line was sequentially selected *in vivo* for brain-homing capacity [66], for a total of three times, resulting in the new PyMT-BrM3 variant used herein. The PyMT-BrM3 cell line was maintained in DMEM/F-12 medium containing 10% fetal bovine serum with 1% l-glutamine and 1% penicillin/streptomycin.

Glioma model

4.5 to 7 week-old mice were intracranially injected as previously described [66, 72, 73, 155]. Briefly, mice were fully anesthetized using isoflurane inhalation anesthesia (2% isoflurane/O_2 mixture), and a mixture of 2% lidocaïne (Streuli Pharma) and 0.5% bupivacaine (Carbostesin; Aspen Pharma Schweiz) was applied as a local anesthetic (50 µl per mouse), and 0.3 mg/ml buprenorphine (Temgesic; Indivior Schweiz) was given subcutaneously as a systemic anesthetic (100 µl per mouse). Using a stereotactic apparatus, cells were injected into the right frontal cortex (2 mm frontal, 1.5 mm lateral from bregma, 2 mm deep). Mice were injected with 2 x 10^5 RCAS-PDGFB-HA or PDGFB-HA-SV40-GFP DF1 cells. The skin incision was sealed with Vetbond tissue adhesive (3M), and the mouse was placed on a heating pad and monitored until fully recovered from anesthesia. Finally, Bepanthen cream (Bayer) was applied on the incision site before placing the animal back in the cage, and following each mouse by regular monitoring.

Generation of experimental brain metastasis

The initiation of brain metastasis from the PyMT-BrM3 line was performed as previously described for other BrM derivatives [66, 156, 157]. Briefly, PyMT-BrM3 cells were

resuspended in HBSS (Life Technologies) and 1×10^5 cells were inoculated into the left cardiac ventricle of 6-10 week-old female C57BL6/J mice.

Cranial window surgery

Mice were fully anesthetized using isoflurane inhalation anesthesia (2% isoflurane/O_2 mixture) and prepared for surgery by shaving and cleaning the head with 70% ethanol pads (Fisher Healthcare) and 10% betadine pads (Purdue Products L.P.). A mixture of 2% lidocaïne (Streuli Pharma) and 0.5% bupivacaine (Carbostesin; Aspen Pharma Schweiz) was applied as a local anesthetic (50 µl per mouse), and 0.3 mg/ml buprenorphine (Temgesic; Indivior Schweiz) was given subcutaneously as a systemic anesthetic (100 µl per mouse). A longitudinal incision of the skin was made between the occiput and forehead, and the skin covering the skull was cut in a circular manner, by removing approximately 3 mm of the skin edges on each side. After cleaning and drying the skull with a cotton swab, the bone was etched mechanically with a scalpel (by making a pattern of crosses) and chemically by applying 35% phosphoric acid solution (Santa Cruz Biotechnology) with a cotton swab. The skull was then cleaned several times with Ringer's solution (Dutscher), and the mouse was placed into a stereotactic device with a three-axis micromanipulator and an integrated heating pad (Stoelting). A 3-mm craniotomy was made using a 3-mm biopsy punch (Integra Miltex), ensuring precise fitting of the imaging window. The exposed cortical surface was kept moist with Ringer's solution. Tumor cells were injected into the brain parenchyma at the craniotomy site as described in the previous section. The brain surface was sealed with a 0.085-mm-thick 3-mm diameter coverslip (Multichannel Systems) that was glued to a 0.085-mm-thick 5-mm diameter coverslip (Multichannel Systems) using Norland optical adhesive 61 (AMP Technica). The outer edges of the 5-mm coverslip were used to fix the imaging window to the skull using super glue (Loctite). A small head bar was fixed using super glue (Loctite), allowing later fixation of the mouse's head during the intravital imaging experiments. Lastly, dental acrylic glue (Kulzer) was applied on the skull surface, covering also a small rim of the 5-mm coverslip. The animal was then placed on a heating pad and monitored until it had fully recovered and was returned to the cage, followed by regular monitoring.

Treatments

Perfluorocarbons

An initial PFC emulsion based on 10% weight/volume (wt/vol) perfluoro-15-crown-5 ether (PFCE) was prepared in-house as described previously [113, 129]. The emulsion contains nanoparticles with a mean size of 200 nm, and produces a single spectral line at -92.8 ppm. A second, similar PFCE emulsion was prepared with rhodamine in order to perform

histological validation and cell sorting. A third PFC emulsion based on 60% wt/vol perfluoro-t-butylcyclohexane (PFTBH) [158] was provided by Aurum Biosciences (Glasgow, United Kingdom).

Intravenous injections

A red heat lamp (Beuer) was placed at 15 to 20 centimeters (cm) distance from the cages housing the mice to be injected. After 15 minutes, a mouse was removed from the cage and placed into a restrainer (Indulab) and held in a firm position through the nose holder, allowing proper breathing and minimal movement of the animal. The tail was gently cleaned with 70% ethanol pads (Fisher HealthCare) to disinfect the skin and better visualize the tail vein. The mouse was injected with a 29-gauge (G) needle syringe (BD Medical) in the right or left lower tail vein. For PFCE-NP and Rhodamine-PFCE-NP, 10 µL/g were injected. For PFTBH-NP 3.3 µL/g were injected. The difference in the amount of NP injected accounts for 1) the difference in wt/vol %, and 2) the different amount of fluorine atoms contributing to the ^{19}F signal. For lectin Dylight649 (Vector), 100 µL was injected via the tail vein for each mouse.

Irradiation

Tumor-bearing mice were fully anaesthetized using isoflurane inhalation anaesthesia (2% isoflurane/O_2 mixture). Irradiation of the head was performed with a X-RAD SmART instrument (Precision X-Ray) equipped with 1x1 cm collimator to limit irradiation to the tumor area only. First, a live-imaging CT scan of the head was performed to place the collimator in the correct position to irradiate the brain (cerebellum and the upper respiratory tract were left outside the field of view). A beam of 5 Gy was dosed laterally for the animal, from the right side and the left side respectively, for a total of 10 Gy.

Tissue analysis

Brain slice harvesting and confocal imaging

Mice were sacrificed by terminal anesthesia using pentobarbital (CHUV, Lausanne, Switzerland), followed by transcardial perfusion with PBS. Tumor-bearing brains were harvested and placed on ice in “slicing medium” (minimum essential media 2 mM l-glutamine (MEM GlutaMAX, Life Technologies), 4.5 mg/mL glucose (Life Technologies), 100 U/mL penicillin-streptomycin (P/S, Life Technologies)). When possible, the tissue was kept in the dark to preserve the fluorophores. The brain was then fixed on the specimen plate of a vibratome (Leica) with super glue (Loctite). The brain was held in place with 2% agar cubes to additionally support the tissue while slicing, and submerged into “slicing medium” in the buffer tray. The vibratome was set at a moving speed of 0.5 mm/s, a vibration amplitude of 1

µm, and 425-µm-thick coronal slices were cut sequentially and placed into “culturing medium” (MEM GlutaMAX, 4.5 mg/mL glucose, 100 U/mL P/S, 25% HBSS (Life Technologies), 25% heat-inactivated normal horse serum; re-supplement: 1X GlutaMAX (Life Technologies), 1X non-essential amino acids (Life Technologies), 1:50 1M HEPES (Life Technologies)) on ice. 3 to 4 slices per mouse were placed on a microscope slide (Fisher Scientific) and enclosed by a layer of Dowsil 732 multi-purpose sealant (Dow) to create a small bucket which was then filled with a small amount of culturing medium, and finally enclosed by a coverslip (Menzel-Gläser). Images were acquired using an upright Leica TCS SP8 DIVE multi-photon microscope (Mannheim, Germany) equipped with a 16× (HC FLUOTAR L N.A. 0.6 FWD 2.5 mm) multi-immersion objective. GFP and Rhodamine were excited with a wavelength of 960 nm, and detected between 500-540 nm and 580-650 nm respectively. Lectin DyLight649 was excited with a wavelength of 810 nm and detected at 690-800 nm (a second detector was set as “empty channel” on 300-475 nm to detect any broad autofluorescence signals).

Flow cytometry

Mice were sacrificed by terminal anesthesia using pentobarbital (CHUV, Lausanne, Switzerland), followed by transcardial perfusion with PBS. When possible, the tissue was kept in the dark to preserve the fluorophores. The brain tumor was macro-dissected and dissociated using the Brain Tumor Dissociation Kit (Miltenyi). The dissociated tissue was filtered through a 40 µm mesh filter and then underwent myelin removal using the Myelin Removal Beads Kit (Miltenyi). The resulting myelin-free single cell suspension underwent red blood cell lysis for 10 minutes on ice using 10x red blood cell lysis buffer (Biolegend). The single cell suspension was stained with the Zombie-near-infrared fixable viability kit (Biolegend) for 20 minutes at room temperature (RT), washed with FACS buffer (2 mM EDTA (Life Technologies) and 0.5% BSA (Jackson ImmunoResearch) in PBS (Bichsel) and then FC-blocked (BD Biosciences) for 30 minutes on ice. After washing with FACS buffer, cells were incubated with directly-conjugated antibodies (table 1). Stained samples were washed 3 times with FACS buffer and acquired on a BD Fortessa at the Flow Cytometry Core Facility of University of Lausanne. FlowJo v10.7.1 (BD) was used for analysis.

Tissue section immunofluorescence staining and imaging

10 µm tissue sections were thawed for 10’, and circles were drawn around the tissue with a PAP pen (Daido Sangyo). After 5’ wash with 1X PBS (Bichsel), the slides were permeabilized with 0.1% Triton X-100 (AppliChem) diluted in 1X PBS for 10’ at room temperature (RT). Slides were then washed 3x5’ with 1X PBS and then incubated with filtered blocking buffer for 1 hour at RT (1X PBS, 0.2% bovine serum albumin (Jackson ImmunoResearch), 10% donkey normal serum (EMD Millipore), 10% goat normal serum (Merck) – when using goat primary

antibodies, BSA and goat serum were omitted from the blocking buffer mix). Sections were then incubated with the 250 µL/section primary antibodies mix (table 1) in dilution buffer (1:1 mix of 1X PBS and blocking buffer) at 4°C overnight. The day after, slides were washed 3x10' with 1X PBS and then incubated with the secondary antibody mix (table 1) in dilution buffer including 1:5000 DAPI (Life Technologies) for 1h at RT. Slides were eventually washed 3x10' with 1X PBS and mounted with a coverslip (Menzel-Gläser) and Dako mounting medium (Agilent). Stained tissue sections were imaged with an Axio Scan.Z1 slide scanner (Zeiss) equipped with a Colibri 7 LED light source (Zeiss) using a Plan-Apochromat 20x/0.8 DIC M27 coverslip-corrected objective (Zeiss). All slides from the same staining panel were digitalized using the same acquisition settings. All washes were performed in a slide bucket, while all incubation steps were performed in a humified chamber. One section was stained with primary antibodies, while the adjacent section on the same slide was stained with secondary antibodies alone to assess unspecific antibody binding and signal.

Prussian Blue staining and imaging

Prussian blue (PB) staining was performed on freshly-thawed 10 µm sections, or after IF staining for multiplexing analysis. Sections were washed 2x10' with deionized H_2O and then incubated 15' with a 1:1 solution of freshly mixed hydrochloric acid solution (Abcam) and potassium ferrocyanide solution (Abcam). After 2x5' washes with deionized H_2O, sections were stained 3' with nuclear fast red solution (Abcam). Sections were finally washed 4x5' with deionized H_2O and dehydrated with 95% and 100% ethanol solutions (Reactolab) and xylene (Reactolab), before mounting with Pertex mounting medium (Histolab) and a coverslip (Menzel-Gläser). Slides were left to dry for 24h before imaging with an Axio Scan.Z1 slide scanner (Zeiss) equipped with a Colibri 7 LED light source (Zeiss) using a Plan-Apochromat 20x/0.8 DIC M27 coverslip-corrected objective (Zeiss).

In vivo mouse imaging

^{1}H and ^{19}F MR imaging acquisition

All MRI experiments were performed on a 3T clinical system (MAGNETOM Prisma, Siemens Healthineers, Erlangen, Germany). A 35 mm-diameter transmit/receive birdcage radiofrequency (RF) coil tunable to both the ^{19}F and ^{1}H frequencies (Rapid Biomedical, Rimpar, Germany) was used for both excitation and signal detection. Two days after the PFC-NP injection, the animals were anesthetized with 2.5% isoflurane in oxygen for 1–2 minutes. Anaesthesia was maintained with 1.5–2% of isoflurane for the duration of the scan. The body temperature was monitored with a rectal probe and maintained at 37.0±0.5 °C with a tubing system circulating warm water, while the respiratory activity was monitored by means of a

respiration pillow placed below the mouse abdomen (all SA Instruments, Stony Brook, NY, USA). An external reference tube with a known concentration of PFCE-NP (18.95 mM) in 2% wt/vol agar gel (Life Technologies) was created and used for absolute quantification. The tube was carefully placed diagonally below and to the side of the brain of the animal (i.e. at the level of the shoulders) such that signal emitted from this reference did not interfere with the signal from the brain. In the dual-PFC experiments, a second probe with PFTBH-NP (40 mM) was placed next to the other shoulder of the animal. Multi-planar low-resolution scout scans were then performed for anatomic localization.

For glioma imaging, a high-resolution T_2-weighted 3D turbo spin echo (TSE) scan was acquired in an axial orientation. The following pulse sequence parameters were used: repetition time TR = 4500 ms, echo time TE = 80 ms, echo train length (ETL) = 32, pixel bandwidth BW = 130 Hz/pixel, field of view (FOV) = 60 × 60 × 32 mm^3, voxel size = 0.16 × 0.16 × 1 mm^3, number of slices = 32, slice oversampling = 12.5%, acquisition time T_{acq} = 32min19s.

For metastasis imaging, mice were injected intraperitoneally (i.p.) with 150 µl Gadobutrol (Gadovist, 1 mmol/mL, Bayer) 10 min before the measurement. A high-resolution T_1-weighted 3D gradient-recalled echo (GRE) scan was acquired with the following parameters: TR = 280 ms, TE = 3.4 ms, BW = 320 Hz/pixel, FOV = 60 × 60 × 20 mm^3, voxel size = 0.21 × 0.21 × 1 mm^3, number of slices = 20, slice oversampling = 10%, T_{acq} = 29min33s.

^{19}F MR images of PFCE were obtained with a 3D TSE pulse sequence with the following sequence parameters optimized for maximal SNR in 30 minutes [159]: TR = 2460 ms, TE = 13 ms, BW = 130 Hz/pixel, ETL = 43, FOV = 100 × 100 × 16 mm3, voxel size = 0.78× 0.78 × 1 mm3, number of slices = 16, slice oversampling = 12.5%, number of signal averages NA = 14, T_{acq} = 30min57s. The center of the 3D volume was placed at the same position as the ^1H 3D volume. When PFTBH was imaged, the ^{19}F resonance frequency was shifted to the appropriate frequency and the same 3D TSE pulse sequence was used, but with TR = 2850 ms, NA = 9, ETL = 35, and T_{acq} = 30min44s.

Non-quantitative MRI monitoring

Monitoring of tumor growth for non-quantitative MR imaging was performed using a 3 Tesla Small Animal MR Scanner (Bruker BioSpec) with a volume coil as transmitter and a 2x2 channel surface coil for signal reception. The mouse was fully anaesthetized with 1-2% isoflurane/oxygen inhalation and placed on the imaging bed with the head held in place below the surface coil, while monitoring respiratory rate and temperature. Data acquisition was performed using the Paravision 360 v2.0 software (Bruker). A 3-slice localizer was performed to assess the mouse head position. For glioma-bearing mice, 2D T_2-weighted acquisition was performed (turbo rapid acquisition relaxation enhancement (Turbo-RARE), repetition time

(TR) 3000 ms, echo time (TE) 75 ms, number of averages (NA) 6, number of slices 10, slice thickness (ST) 0.7 mm, FOV 20 x 20 mm, pixel size 156 x 156 µm, echo train length (ETL) 12, acquisition time (AT) 3min0sec) with images being acquired in axial planes. After imaging, the mouse was returned to the cage and monitored until it regained consciousness. Volumetric analysis of the gliomas was performed on MR images DICOM files using the MIPAV software (National Institutes of Health, USA). For BrM-bearing mice, animals were injected intraperitoneally (i.p.) with 150 µl Gadobutrol (Gadovist, 1 mmol/mL, Bayer) 10 min before the measurement. T_1-weighted images were acquired (fast low angle shot magnetic resonance imaging (T_1-FLASH), repetition time (TR) 253.3 ms, echo time (TE) 6.288 ms, number of averages (NA) 6, number of slices 10 , slice thickness (ST) 0.7 mm, FOV 20 x 20 mm, pixel size 156 x 156 µm, echo train length (ETL) 1, acquisition time (AT) 3min14sec).

Intravital imaging

Mice were sedated using isoflurane inhalation anesthesia (3% isoflurane/O_2 mixture). Mice were fixed with a head-bar to a custom-designed mouse holder, and the concentration of isoflurane was lowered to 0.8-1.2% to keep the mice lightly sedated, characterized by a constant and non-forced breathing pattern. The mouse was placed in the climate chamber surrounding the microscope, keeping the entire stage of the microscope and the objectives at 34°C. Imaging was performed on an upright Leica TCS SP8 DIVE multi-photon microscope (Mannheim, Germany) with an InSight X3 tunable laser (Spectra Physics) and two non-descanned hybrid 4Tune detectors. GFP and Rhodamine were excited with a wavelength of 960 nm, and detected between 500-540 nm and 580-665 nm respectively. All images were acquired with a 16× (HC FLUOTAR L N.A. 0.6 FWD 2.5 mm) multi-immersion objective. The objective lens was corrected for imaging with Immersol W 2010 (Carl Zeiss) and a coverslip thickness of 0.17 mm. For each mouse, a tile scan of the whole cranial imaging window (CIW) was taken before, immediately after, 6h and 24h after PFCE-NP injection.

Data analysis

MR Image Analysis

^{1}H images produced by the MR scanner in dicom format were copied, while the ^{19}F images were reconstructed from raw data in Matlab (the Mathworks, Natick, MA, USA) in order to ensure that the background noise was correctly digitized. All subsequent image analyses were then performed in Matlab. The ^{1}H and ^{19}F MR images were post-processed in several semi-automated steps in order to obtain reproducible PFC quantifications. The visible tumor volume was manually delineated in the high-resolution ^{1}H images to calculate the ^{1}H tumor volume. The slice numbers that visually contained tumor tissue were retained to constrain the ^{19}F

calculations. In the stack of ^{19}F images, a rectangular region of interest (ROI) was drawn at the edge of the image to determine the background noise level for subsequent thresholding. The ^{19}F images were then flattened into a maximum intensity projection (MIP) on which rough very inclusive ROIs were drawn around the tumor, reference tube, and liver. These MIP ROIs were then copied to all slices. Simultaneously, the ^{19}F images were automatically thresholded at 6 times the standard deviation of the previously determined noise level in order to generate a mask that only contains voxels with a high ^{19}F signal. The retained slices, manually drawn MIP ROIs and the mask were then multiplied to reproducibly generate selective tumor, liver, and reference tube ROIs. The average ^{19}F signal in these ROIs was divided by the noise standard deviation to calculate the tumor, liver, and reference tube ^{19}F signal-to-noise ratio (SNR). The ^{19}F signal, SNR and ROI volume of each animal was retained, and used to calculate the PFC concentration.

2p microscopy image analysis

3D-images from the high-resolution imaging of brain tumor-bearing slices were imported into Imaris version 9.7.2 (Bitplane). For each sample, 3 to 6 volumes-of-interest (VOI) were analyzed, including one VOI of the healthy contralateral brain adjacent to the tumor. Before cell/structure classification and segmentation, images were corrected for bleed-through using the "channel arithmetic" plugin. The following signal corrections were performed: "lectin DyLight649"-"rhodamine" to clean the lectin signal from the rhodamine bleed-through; "rhodamine"-" empty channel", to clean the rhodamine signal from broad autofluorescence. Rhodamine foci and cancer cells were classified and segmented using the "surface" creation tool. Vessels were first defined using the "surface" creation tool, and then the network composition was reconstructed with the "filament" creation tool. Vessel parameters included dendrite area, length, orientation angle, straightness, volume, diameter, ratio segments and branching points, and vessel coverage. For each VOI, vessel parameters and Rhodamine-PFCE-NP uptake were Z-score normalized and the principal-component analysis (PCA) was performed using the R package "devtools". FlowJo v10.7.1 (BD) was used to analyze single cell/foci data.

For IVM quantification, high-resolution 3D tilescan images were imported into Imaris version 9.7.2 (Bitplane). Blood vessel location was identified at time point 1h by visualization of the circulating Rhodamine-PFCE-NP, and additional landmarks were annotated (cancer cells, second harmonic generation (SHG)) to identify the same location in the timepoints 0h, 6h and 24h.

Alignment workflow of PB and IF images

IF and PB image FOVs were exported as 8-bit BigTiff files from the ZEN 2.6 blue edition software (Zeiss). Image J (National Institutes of Health, USA) was used for imaging processing. First, PB images were rescaled by a factor of 0.676923076923077 to correspond to the IF images. The Bigwarp plugin was used to align the nuclei of the IF and PB images, based on the DAPI nuclear staining and Nuclear red staining respectively, by defining at least 10 reference matching points. All channels were then concatenated, the voxel size set to 0.325x0.325 µm and a voxel depth of 2, and eventually an hyperstack was created. All RGB channels were inverted and a ome.tif file was exported for analysis with VIS image Analysis Software (Visiopharm, see next section).

Image analysis and cell type identification

Image quantification was performed using the VIS image Analysis Software (Visiopharm). For each staining panel a specific application was designed. The tumor area was outlined based on the DAPI signal. Aberrant signals resulting from air bubbles or dust particles were manually excluded. Nuclear masks and cell marker masks were created using the application creator plugins and commands. Cell types were defined using a hierarchical decision tree based on manual thresholds of the nuclear signal and the proximity of marker masks to the nucleus. Vessels were defined based on the CD31 mask alone. “MDM-ROI” and “PB-ROI” were established by generating an ROI of 150 pixels (48.75 µm) around a positive nucleus. Cell count data and distance measurements were exported for each cell type.

Fluorescence-activated cell sorting, RNA sequencing and bioinformatics

Single cell suspensions of brain tumors were stained as indicated in the “flow cytometry” section. $CD45^{+}/Cd11b^{+}/Ly6C^{-}/Ly6C^{-}$ $Rhodamine^{+/-}$ TAMs (>2000 cells) were sorted directly into TRIzol LS (Thermo Fischer Scientific) and immediately snap frozen in liquid nitrogen. RNA extraction, library preparation and sequencing were performed by Genewiz (South Plainfield, New Jersey, USA) on an Illumina HiSeq 2500 (Illumina). Adapter sequences and low-quality ends were removed with cutadapt, trimming for TrueSeq and polyA sequences. Reads were aligned to the mouse genome build mm10 using HISAT2 aligner. Samples were normalized with TMM method (edgeR package) and log2 transformed with voom (limma package). Differential expression was computed with limma, after filtering out genes with average FPKM (fragments per kilobase million) < 1. Pathway analysis was performed with mSigDB v7.0 using four collections: hallmark, canonical pathways, GO biological process and GO cellular components. Publicly available raw RNA-seq data were retrieved from GEO (number GSE99537) [75].

Statistics

R version 4.1.0 was used to perform statistical analysis and graphically plot all data (ggplot package). Parametric data were analyzed by a two-tailed Student's t-test (paired or unpaired depending on the experimental setup). Non-parametric data were analyzed by a Mann-Whitney test on ranks (paired or unpaired depending on the experimental setup). $P<0.05$ was considered as statistically significant. Each specific statistical test is reported for each experiment in the figure legends. Boxplots are used to present the data, showing median and the 25^{th} to 75^{th} percentiles.

Table 1: Antibodies used in the study

Antibodies							
Target	**Species**	**Antibody**	**Manufacturer**	**Clone**	**Category number**	**Dilution**	**Application**
Ly-6C	Rat	Anti-mouse Ly-6C Brilliant Violet 711	BioLegend	HK1.4	128037	1:800	Flow cytometry panel #1 and #3
Ly-6G	Rat	Anti-mouse Ly-6G Brilliant Violet 605	BioLegend	1A8	127639	1:160	Flow cytometry panel #1 and #3
CD11b	Rat	Anti-mouse CD11b BUV661	BD Biosciences	M1/70	612977	1:800	Flow cytometry panel #1 and #2
CD45	Rat	Anti-mouse CD45 FITC	BD Biosciences	30-F11	553080	1:200	Flow cytometry panel #1, #2 and #3
CD49d	Rat	Anti-mouse CD49d PE/Cy7	BioLegend	R1-2	103618	1:160	Flow cytometry panel #1
CD3	Hamster	Anti-mouse CD3e BUV395	BD Biosciences	145-2C11	563565	1:75	Flow cytometry panel #1 and #2
NK-1.1	Mouse	Anti-mouse NK-1.1 Brilliant Violet 421	BioLegend	PK136	108741	1:640	Flow cytometry panel #1
NK-1.1	Mouse	Anti-mouse NK-1.1 Brilliant Violet 711	BioLegend	PK136	108745	1:640	Flow cytometry panel #2
CD19	Rat	Anti-mouse CD19 Brilliant Violet 605	BioLegend	6D5	115539	1:320	Flow cytometry panel #2
CD31	Rat	Anti-mouse CD31 PE/Cy7	BioLegend	390	102418	1:100	Flow cytometry panel #2
CD11b	Rat	Anti-mouse CD11b APC	Invitrogen	M1/70	17-0112-81	1:800	Flow cytometry panel #3
CD31	Goat	Anti-mouse CD31	R&D systems	Polyclonal	AF3628	1:100	Immunofluorescence panel #1
CD68	Rat	Anti-mouse CD68	Bio-Rad	FA-11	MCA1957	1:500	Immunofluorescence panel #1
IDH2	Rabbit	Anti-mouse IDH2	Cell Signaling Technology	D8E3B	56439S	1:100	Immunofluorescence panel #1
Iba1	Goat	Anti-mouse Iba1	Abcam	Polyclonal	ab5076	1:300	Immunofluorescence panel #2
P2RY12	Rabbit	Anti-mouse P2RY12	Anaspec	Polyclonal	AS-55043A	1:300	Immunofluorescence panel #2
YFP	Chicken	Anti-GFP (cross-reactive to YFP)	Abcam	Polyclonal	ab13970	1:1000	Immunofluorescence panel #3
Goat IgG (H+L)	Donkey	Anti-goat IgG Alexa Fluor 555	Invitrogen	Polyclonal	A21432	1:500	Immunofluorescence panel #1 and #2
Rabbit IgG (H+L)	Donkey	Anti-rabbit IgG Alexa Fluor 647	Invitrogen	Polyclonal	A31573	1:500	Immunofluorescence panel #1 and #2
Rat IgG (H+L)	Donkey	Anti-rat IgG DyLight 755	Invitrogen	Polyclonal	SA5-10031	1:500	Immunofluorescence panel #1
Chicken IgG (H+L)	Donkey	Anti-chicken IgG Alexa Fluor 488	Jackson ImmunoResearch	Polyclonal	703-545-155	1:500	Immunofluorescence panel #3

Flow cytometry panel #1 has been used in experiments presented in figures: 2 and S2
Flow cytometry panel #2 has been used in experiments presented in figures: 2 and S2
Flow cytometry panel #3 has been used in experiments presented in figures: 4 and S4
Immunofluorescence panel #1 has been used in experiments presented in figures: 4 and S4
Immunofluorescence panel #2 has been used in experiments presented in figures: 5, S6, S7
Immunofluorescence panel #3 has been used in experiments presented in figures: 6, 7

6.1.6 Figures

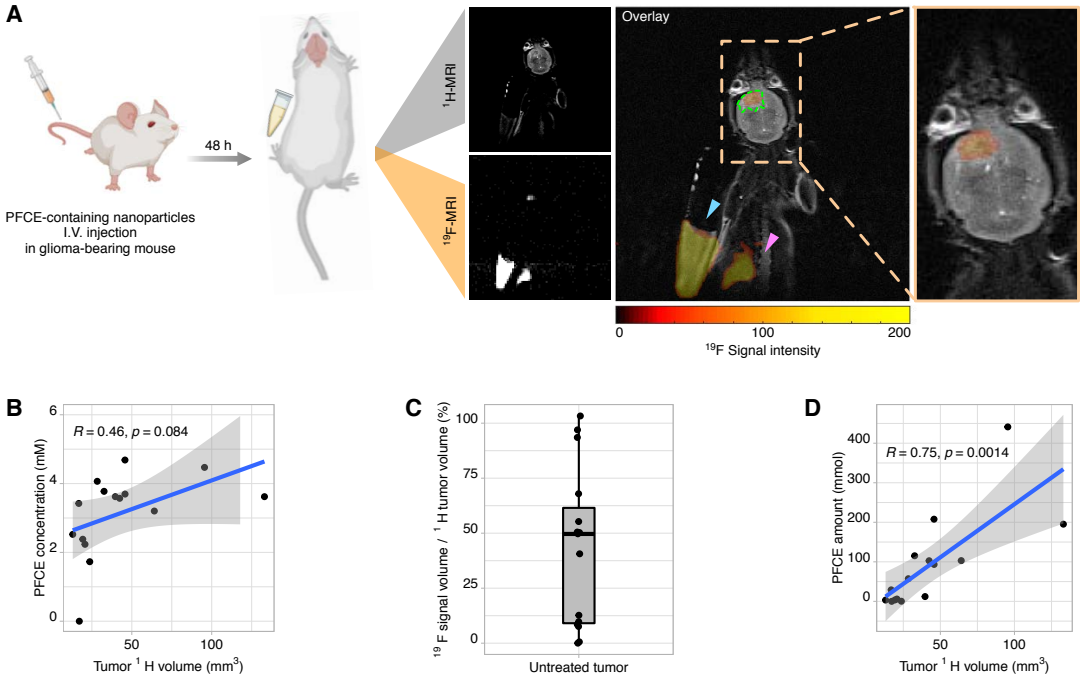

Figure 1. ^{19}F MRI allows the non-invasive imaging of glioma-associated inflammation. (**A**) ^{19}F MR imaging workflow: PDG-Ink4a/Arf KO glioma-bearing mice were injected with perfluoro-crown-ether-containing nanoparticles (PFCE-NP) and then imaged 48h later by conventional ^{1}H MRI to visualize the anatomical location of the tumor, in addition to molecular ^{19}F MRI. The overlay (right) shows the ^{19}F signal in the tumor (dashed green line), but not in the contralateral healthy brain, in the liver (pink arrow) and in a PFCE-NP-containing reference tube (cyan arrow) placed adjacent to the mouse which allows the absolute quantification of the tumor signal into a PFCE amount/concentration. Imaging was performed using a clinical 3T MRI (Prism, Siemens) at the local hospital (Centre Hospitalier Universitaire Vaudois, Lausanne). (**B**) Correlation of the PFCE concentration and ^{1}H tumor volume. (**C**) Percentage of ^{19}F signal coverage of the total tumor ^{1}H volume. (**D**) Correlation of the total PFCE amount and ^{1}H tumor volume. Mouse silhouette, syringe and reference tube drawings in (A) were sourced from https://app.biorender.com/biorender-templates. PDG-Ink4a/Arf KO model: n=15 mice. Regression analysis: linear model.

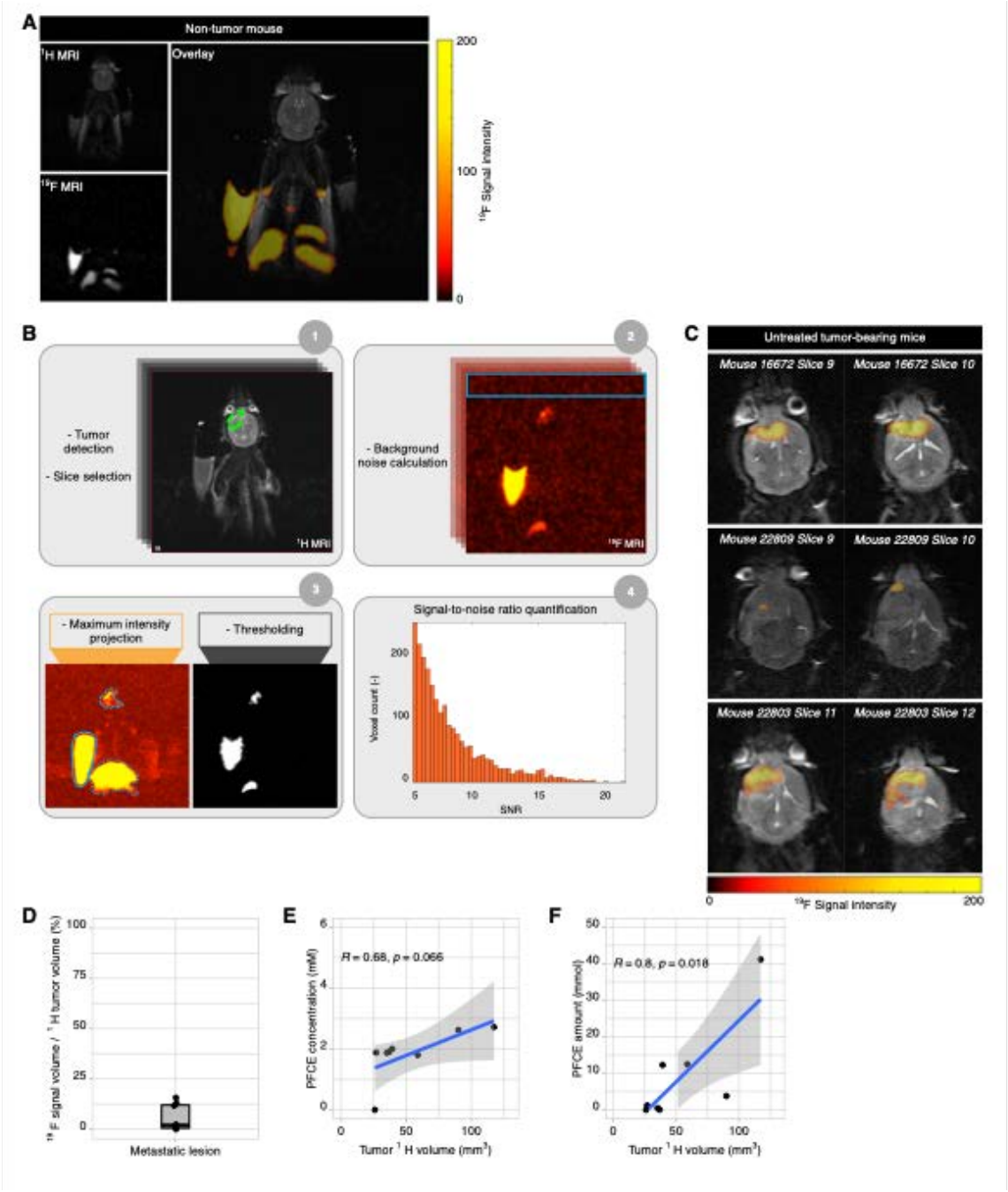

Supplementary Fig. 1. ^{19}F signal is heterogenous and tumor-restricted in glioma and brain metastasis models. (**A**) Representative images of a healthy control mouse injected with PFCE-NP and imaged by ^{1}H and ^{19}F MRI. (**B**) Quantification pipeline and histogram of the ^{19}F signal-to-noise ratio (SNR) inside a representative example of a PDG-Ink4a/Arf KO glioma. *1.* The visible tumor volume is manually delineated in 3D T2-weighted ^{1}H images. The slice numbers that visually contain tumor tissue are retained. *2.* A region of interest (ROI) is drawn at the edge of the 3D ^{19}F image to determine the background noise level for subsequent thresholding. *3.* The ^{19}F images are then flattened into a maximum intensity projection (MIP) on which approximate and inclusive ROIs are drawn for the tumor, reference tube, and liver.

Simultaneously, the 19F images are automatically thresholded to generate a mask. The retained slices, manually drawn ROI and mask are then multiplied to generate a final tumor ROI. *4.* A histogram of the signal-to-noise ratio (SNR=signal divided by the noise standard deviation) of the pixels in the final tumor ROI. (**C**) Representative images of ^{19}F-^{1}H MRI overlay in different glioma-bearing mice. (**D**) Percentage of ^{19}F signal coverage of the total tumor ^{1}H volume (sum of all metastatic lesions) in the PyMT-BrM3 model. (**E**) Correlation of the ^{1}H tumor volume with the PFCE concentration and (**F**) PFCE total amount respectively in the PyMT-BrM3 model. PyMT-BrM3 mice: n=8. Regression analysis: linear model.

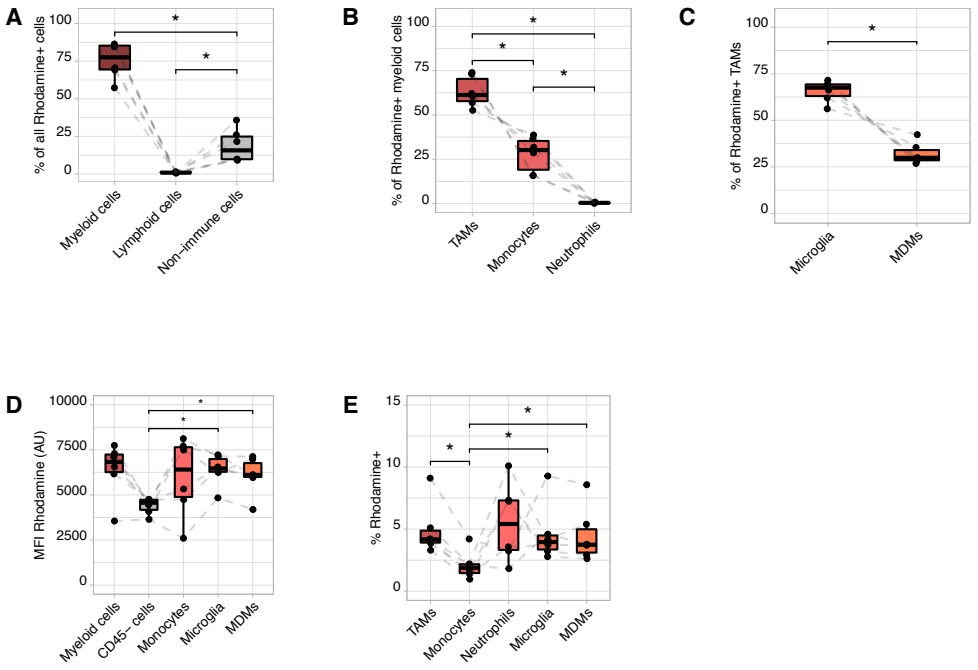

Figure 2. PFCE-NP cellular accumulation occurs predominantly in the TAM compartment. (**A**) Flow cytometry characterization of the fluorescent rhodamine-labelled PFCE-NP positive (Rhodamine-PFCE-NP$^+$) cell pool in PDG-Ink4a/Arf KO gliomas, showing a higher proportion of the myeloid compartment (CD45$^+$/CD11b$^+$ cells) than non-immune cells (CD45$^-$/CD11b$^-$) and lymphoid cells (CD45$^+$/CD11b$^-$). (**B**) Depiction of all Rhodamine-PFCE-NP$^+$ myeloid cells showing tumor-associated macrophages (TAMs) (CD45$^+$/CD11b$^+$/Ly6G$^-$/Ly6C$^-$), monocytes (CD45$^+$/CD11b$^+$/Ly6G$^-$/Ly6C$^+$) and neutrophils (CD45$^+$/CD11b$^+$/Ly6G$^+$/Ly6C$^+$). (**C**) Delineation of Rhodamine-PFCE-NP$^+$ TAMs between microglia (MG) (CD49d$^-$) and monocyte-derived macrophages (MDMs) (CD49d$^+$). (**D**) Median fluorescence intensity (MFI) of the rhodamine signal in the different myeloid cell types. (**E**) Quantification of the percentage of Rhodamine-PFCE-NP$^+$ cells in the different myeloid populations. n=6 mice; * P<0.05, ** P<0.01, *** P<0.001, paired Wilcoxon test.

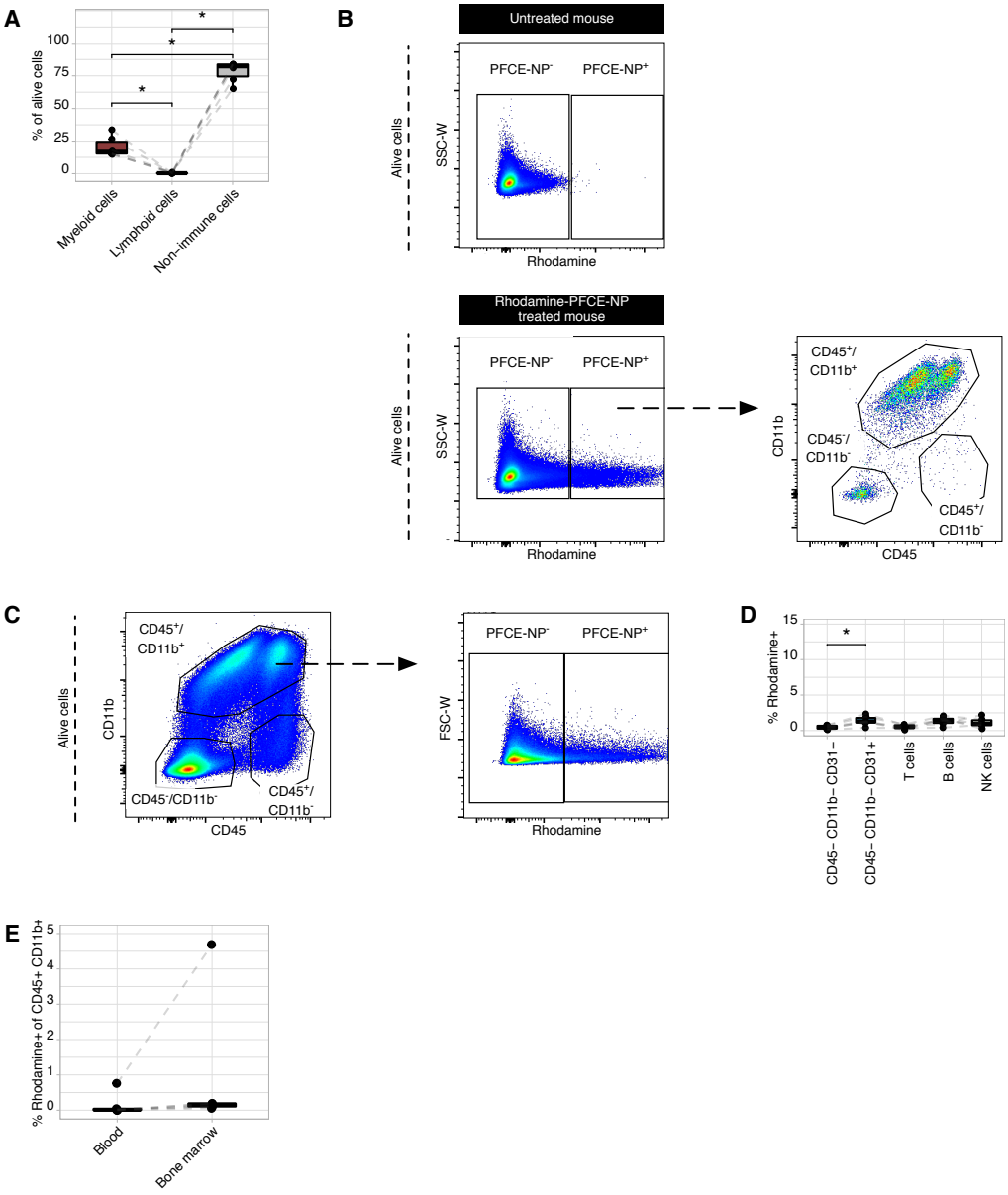

Supplementary Fig. 2. PFCE-NP labelling of myeloid cells occurs *in situ* in the tumor. (**A**) Flow cytometry analysis of the brain tumor microenvironment (TME) composition of PDG-Ink4a/Arf KO gliomas. (**B**) Representative plots of the gating strategy to characterize the cell types in the Rhodamine-PFCE-NP$^+$ cell pool. A glioma sample of an untreated mouse (upper dot plot) was used to define the boundaries of the Rhodamine-PFCE-NP$^+$ alive cells gate, which were then characterized by CD11b and CD45 expression and further stratified using Ly6G, Ly6C, CD49d, CD31, CD3, CD19 and NK1.1 markers (see Materials and Methods for the detailed gating strategy). (**C**) Representative plots of the gating strategy to quantify the frequency of Rhodamine-PFCE-NP$^+$ cells in the CD45$^+$/CD11b$^+$ compartment. The same gating approach was used for the other cell types (see Materials and Methods for the detailed gating strategy). (**D**) Quantification of the percentage of Rhodamine-PFCE-NP$^+$ cells in non-

immune cells ($CD45^-/CD11b^-/CD31^-$), endothelial cells ($CD45^-/CD11b^-/CD31^+$), T cells ($CD45^+/CD11b^-/CD3^+$), B cells ($CD45^+/CD11b^-/CD19^+$) and NK cells ($CD45^+/CD11b^-/NK1.1^+$). (**E**) Quantification of the percentage of Rhodamine-PFCE-NP^+ cells in the myeloid compartment of the blood and bone marrow (BM) of glioma bearing mice. n=6 mice; * P<0.05, ** P<0.01, *** P<0.001, paired Wilcoxon test.

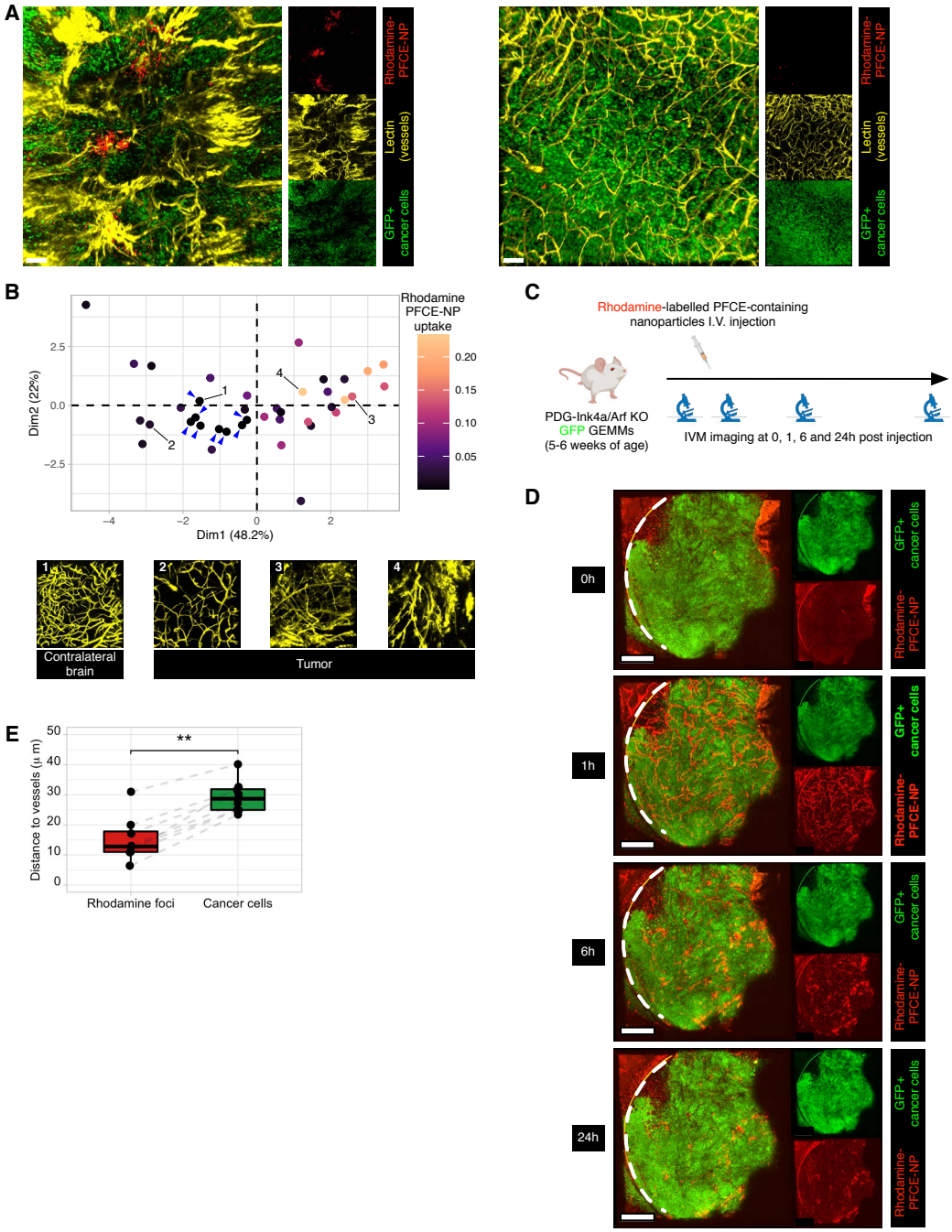

Figure 3. PFCE-NP accumulate in proximity to dysmorphic vessels. (**A**) Representative 2-photon microscopy images of brain slices showing GFP-expressing cancer cells (green), the DyLight649-lectin-labeled vasculature (yellow), and Rhodamine-PFCE-NP^{+} foci (red) in two distinct areas of the same tumor. Scale bar: 100 µm (**B**) Principal component analysis (PCA) based on 9 different vessel parameters (Z-score normalized) of different volume-of-interest (VOI) (3 to 6 VOI/mouse; n=8) in different tumor areas and healthy contralateral brain adjacent to the tumor (blue arrows). The color bar shows the Rhodamine-PFCE-NP uptake (total rhodamine^{+} foci volume normalized to the total VOI volume). Images *1*, *2*, *3* and *4* show

representative VOIs of the vascular morphology in the healthy contralateral brain (*1*) and the tumor (*2* to *4*, ranked by Rhodamine-PFCE-NP uptake). (**C**) Experimental design of the intravital microscopy (IVM): GFP-PDG-Ink4a/Arf KO glioma-bearing were imaged before Rhodamine-PFCE-NP administration (t=0h), 1h, 6h and 24h later. (**D**) Longitudinal imaging of the same glioma-bearing mouse by 2-photon microscopy through a cranial imaging window (CIW – white dashed line). Representative images of the glioma area below the CIW were taken at different time points before (t=0h) and after (t=1h, 6h, 24h) injection of the Rhodamine-PFCE-NP, initially showing the circulation of the NP in the bloodstream (t=1h) followed by a gradual accumulation of Rhodamine^{+} foci in the tumor (t=6h and 24h). Scale bar: 500 µm (**E**) Quantification of the average distance to the DyLight649-lectin^{+} vessels of Rhodamine-PFCE-NP^{+} foci and all GFP-expressing cancer cells respectively. n=8 mice; * P<0.05, ** P<0.01, *** P<0.001, paired Wilcoxon test.

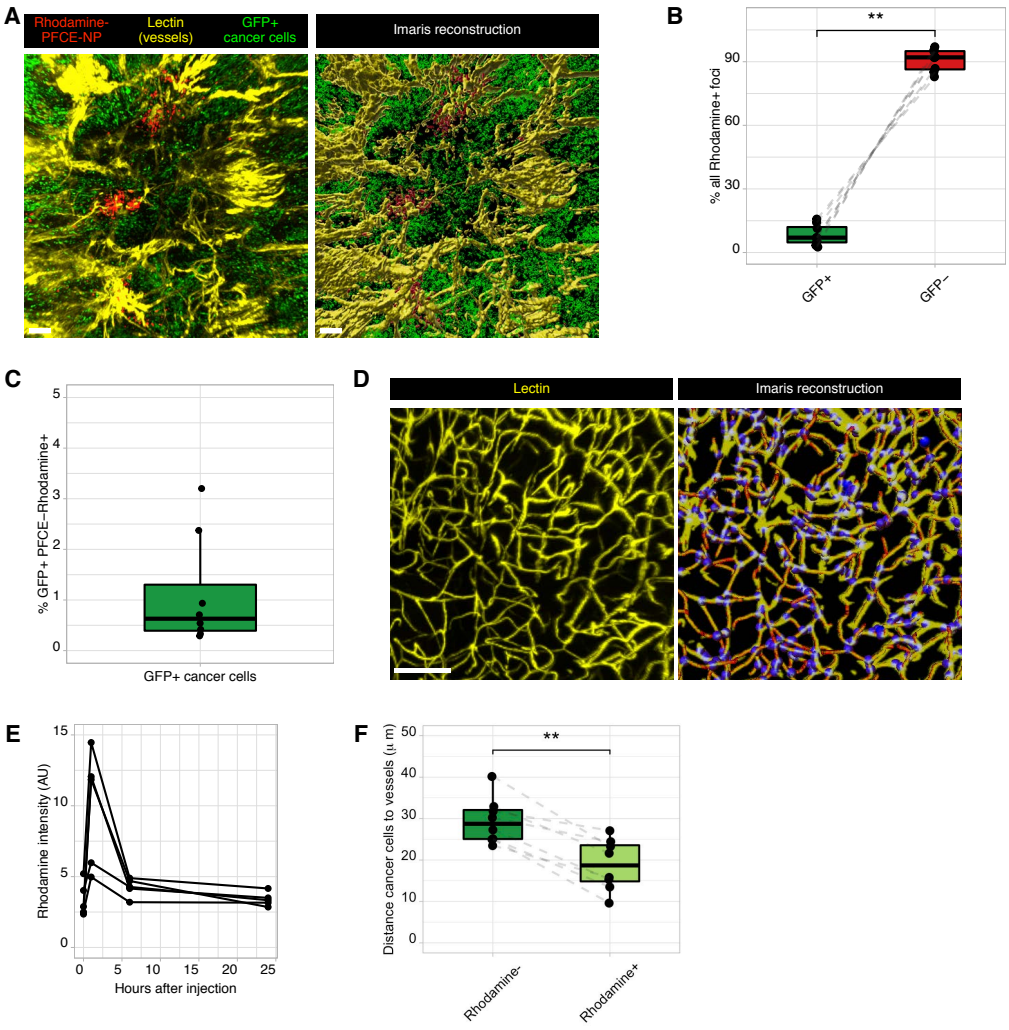

Supplementary Fig. 3. Reconstruction of *ex vivo* slice images. (**A**) Representative reconstruction using *Imaris* software showing GFP-expressing cancer cells (green), DyLight649-lectin^{+} vessels (yellow) and Rhodamine-PFCE-NP^{+} foci (red). Scale bar: 100 µm. (**B**) Subsetting of all Rhodamine-PFCE-NP^{+} foci based on the GFP signal intensity levels. n=8 mice. (**C**) Quantification of the rhodamine^{+} proportion of all GFP-expressing cells. n=8 mice. (**D**) Representative image of the vascular network (left, DyLight649-lectin^{+} signal) reconstructed in *Imaris* (right) showing the lectin-based mask (yellow), vessel dendrites (red) and branching points (blue). Scale bar: 100 µm. (**E**) Quantification of the rhodamine signal intensity measured by 2-photon microscopy inside the tumor vessels of GFP-PDG-Ink4a/Arf KO mice at the different time points after Rhodamine-PFCE-NP injection. n=5 mice. (**F**) Quantification of the average distance to the DyLight649-lectin^{+} vessels of Rhodamine-PFCE-NP$^{-/+}$ GFP-expressing cancer cells. n=8 mice; * P<0.05, ** P<0.01, *** P<0.001, paired Wilcoxon test.

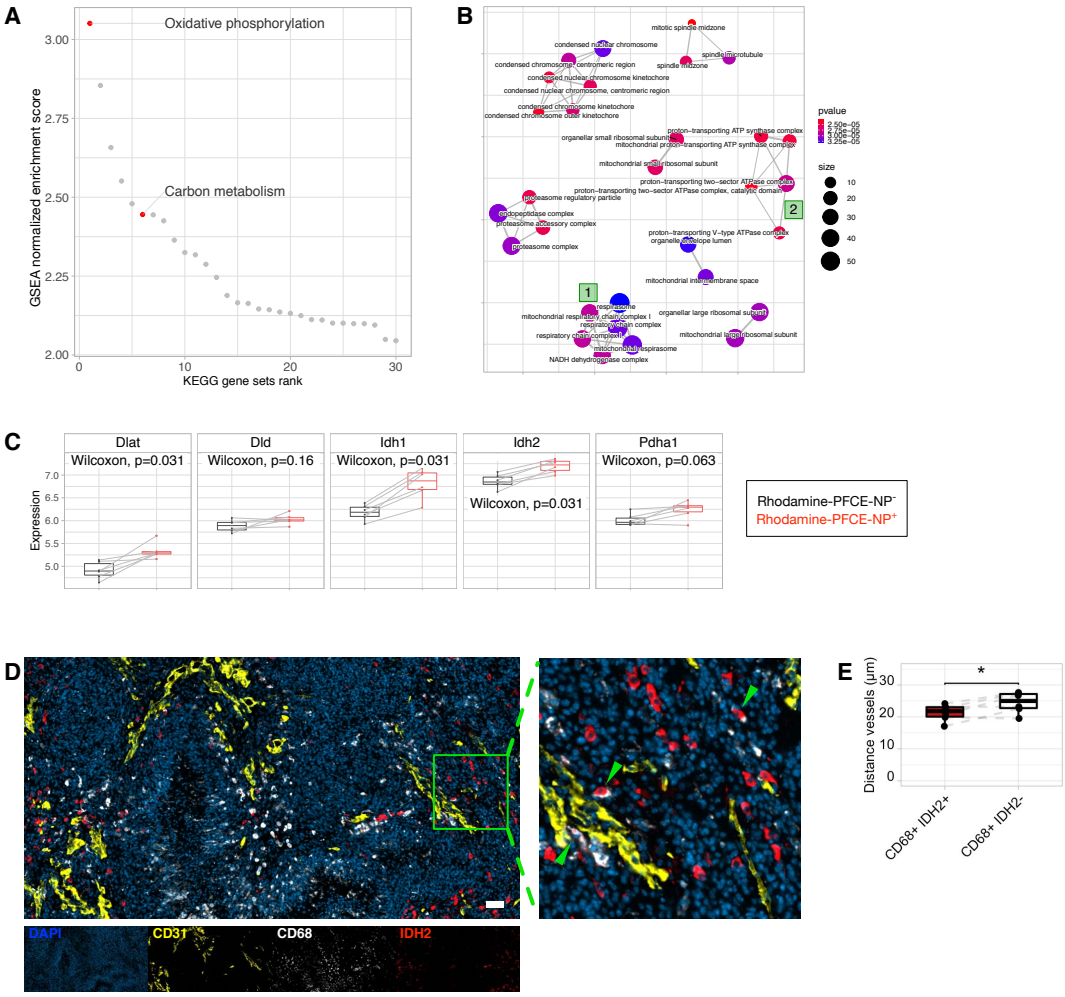

Figure 4. PFCE-NP label a TAM subpopulation associated with high oxidative metabolic potential. (**A**) Gene-set enrichment analysis (GSEA) shows an enrichment of oxidative metabolism-related pathways in the Rhodamine-PFCE-NP^{+} TAMs (KEGG pathway database). (**B**) GSEA network analysis of the top 30 enriched cellular components in the Rhodamine-PFCE-NP^{+} TAMs (GO cellular component database), showing different clusters including several factors involved in mitochondrial oxidative respiration (clusters “1” and “2” in the green squares). The dot size represents the gene set size, while the color bar indicates the p-value. (**C**) Box plots depicting normalized log2 gene expression values for *Dlat*, *Dld*, *Idh1*, *Idh2* and *Phda1* in Rhodamine-PFCE-NP$^{+/-}$ TAMs. n=6 mice. (**D**) Representative immunofluorescence (IF) staining of a PDG-Ink4a/Arf KO glioma showing DAPI^{+} cell nuclei (blue), CD68^{+} TAMs (white), IDH2^{+} cells (red) and CD31^{+} endothelial cells. The green arrows on the magnification (right) indicate CD68^{+}/IDH2^{+} cells. Scale bar: 50 µm. (**E**) IF-based *Visiopharm* quantification of the distance to the vessels (CD31^{+}) of CD68^{+} IDH2^{+} and CD68^{+} IDH2^{-} TAMs. n=6 mice; * P<0.05, ** P<0.01, *** P<0.001, paired Wilcoxon test.

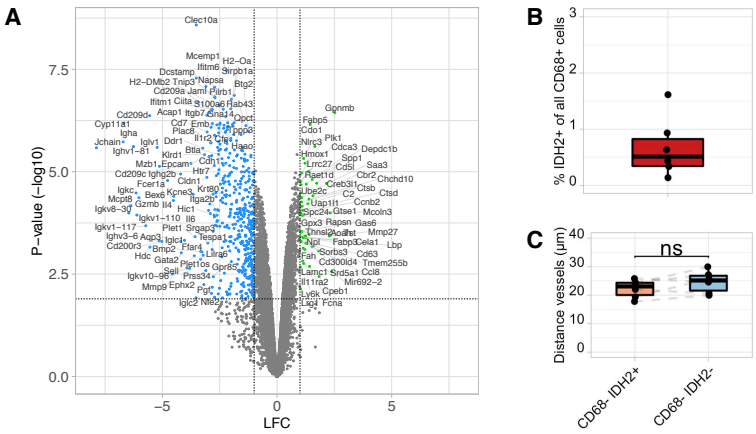

Supplementary Fig. 4. IDH2 is a marker of perivascular TAMs. (**A**) Volcano plot analysis of the RNA-sequencing (RNA-seq) data depicting log2 fold change (x axis) vs. significance (-log10(p-value)) (y axis) of downregulated (blue) and upregulated genes (green) in Rhodamine-PFCE-NP^{+} vs. Rhodamine-PFCE-NP^{-} TAMs. n=6 mice. (**B**) IF-based *Visiopharm* quantification of the frequency of IDH2^{+} cells of all CD68^{+} TAMs. n=6 mice. (**C**) IF-based *Visiopharm* quantification of the distance to the vessels (CD31^{+}) of CD68^{-} IDH2^{+} and CD68^{-} IDH2^{-} cells. n=6 mice.

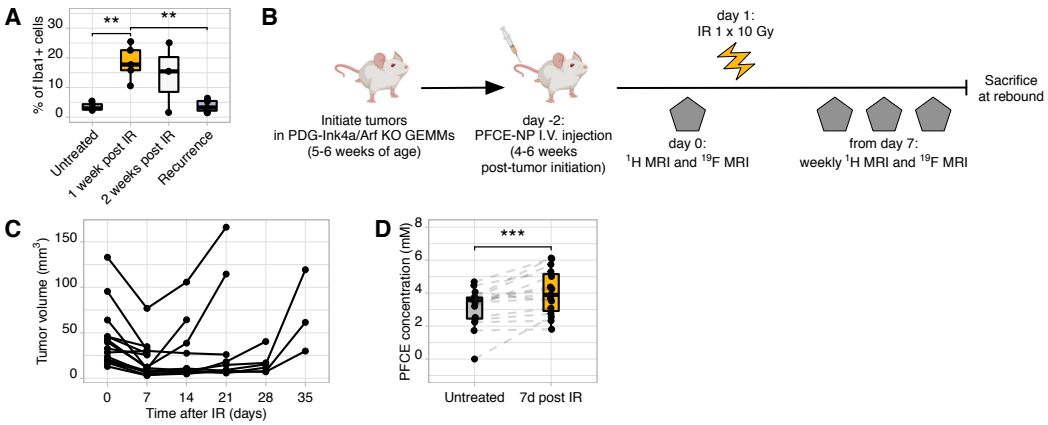

Figure 5. The TAM increase upon radiotherapy can be longitudinally monitored by ^{19}F MRI. (**A**) IF quantification of TAMs using the pan-macrophage marker Iba1, in untreated (n=5 mice), 7 days (n=5 mice), 14 days post-irradiation (IR) (n=3 mice) and recurrent (n=7 mice) PDG-Ink4a/Arf KO glioma tissue sections. ** P<0.01, unpaired Mann-Whitney test. (**B**) Experimental design to monitor TAM dynamics after IR by ^{19}F MRI. At tumor detection, PDG-Ink4a/Arf KO glioma-bearing mice were injected with PFCE-NP and imaged with both conventional ^{1}H and ^{19}F MRI to monitor tumor volume and assess the baseline ^{19}F signal. After the first ^{19}F MRI session, mice were irradiated with a single dose of 10 Gy and then imaged weekly until tumor recurrence by ^{1}H and ^{19}F MRI. (**C**) ^{1}H tumor growth curves in PDG-Ink4a/Arf KO glioma-bearing mice treated with 10 Gy IR. (**D**) Quantification of the tumor PFCE concentration before and 7 days after IR (n=15). Experimental trial described in (B): n=15 mice. * P<0.05, ** P<0.01, *** P<0.001, paired Wilcoxon test.

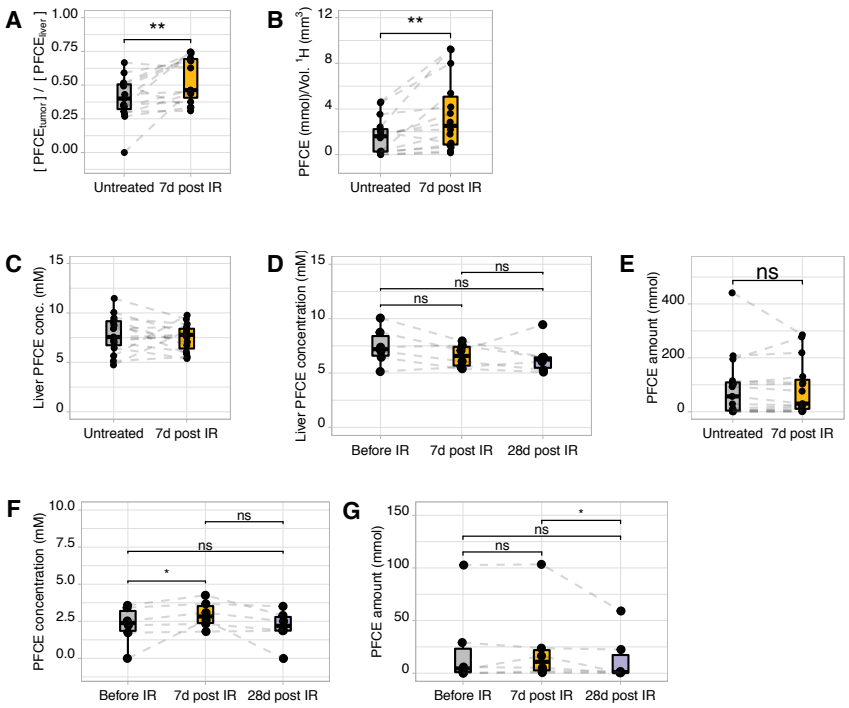

Supplementary Fig. 5. Assessment of tumoral and systemic PFCE concentration dynamics. (**A**) Quantification of the PFCE concentration in the tumor normalized to the concentration in the liver as measure of PFCE clearance (n=15 mice). (**B**) Absolute tumor PFCE concentration calculated from the total PFCE amount and the total ^{1}H tumor volume (n=15 mice). (**C**) Quantification of the liver PFCE concentration before and 7 days after IR and (**D**) in a subset of animals that have been imaged until 28 days after IR (n=6 mice). (**E**) Total tumor PFCE amount before and 7 days after IR (n=15). (**F**) PFCE concentration quantification and (**G**) total PFCE amount in the tumors of a subset of mice that were imaged until 28 days after IR (n=6 mice). * P<0.05, ** P<0.01, *** P<0.001, paired Wilcoxon test.

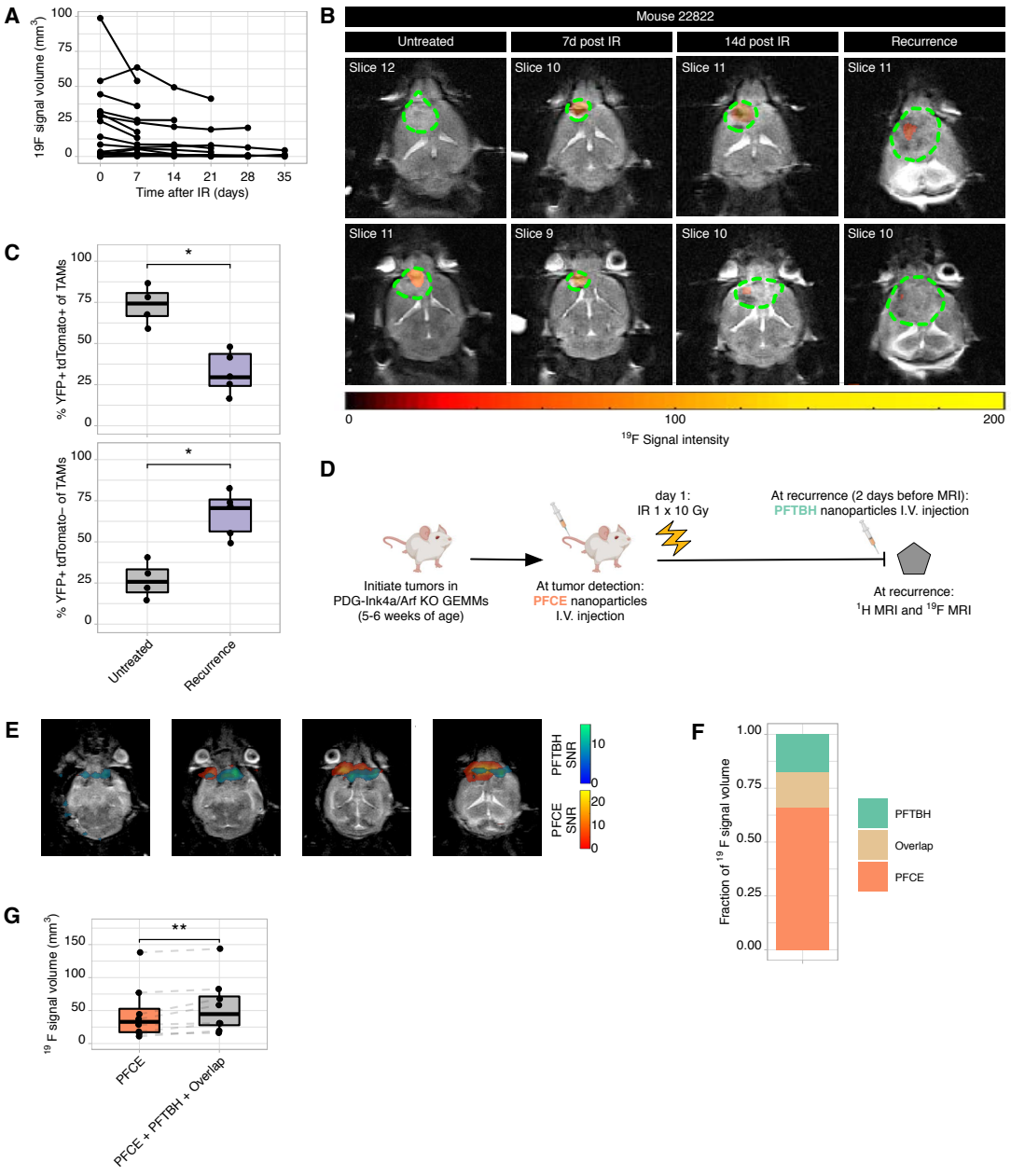

Figure 6. Multispectral ^{19}F MRI identifies temporally-distinct inflamed niches in recurrent gliomas. (**A**) Tumor ^{19}F signal volume curves in PDG-Ink4a/Arf KO glioma-bearing mice treated with 10 Gy IR. n=15 mice. (**B**) Representative ^{19}F and ^{1}H MRI overlay images of the same mouse showing the tumor (green dashed line) and the PFCE ^{19}F signal (orange mask) over the full length of the trial. (**C**) IF-based quantification of MG (upper panel) and MDMs (lower panel) in untreated and recurrent glioma sections. To identify MG and MDMs respectively, we used Cx3cr1:CreERT2-IRES-YFP;Rosa26:lslTdTomato mice that express tdTomato in *Cx3cr1*-expressing cells (MG and circulating blood monocytes) upon tamoxifen injection. Three weeks after tamoxifen-induced labeling, when blood monocytes are replenished by tdTomato^{-} cells and only MG remain tdTomato^{+}, PDG-Ink4a/Arf KO gliomas

were induced. (**D**) Experimental design to monitor TAM temporal dynamics following IR by dual-compound ^{19}F MRI. Glioma bearing mice were injected with PFCE-NP before IR and monitored weekly with conventional ^{1}H MRI. At detection of recurrence, mice were injected with perfluoro-tert-butylcyclohexane-containing nanoparticles (PFTBH-NP) and imaged 2 days later with ^{1}H and ^{19}F MRI, sequentially acquiring both PFCE and PFTBH signals. (**E**) ^{1}H and ^{19}F MRI overlay images of the same animal showing the distinct PFCE ^{19}F signal-to-noise (SNR) (red to yellow mask) and the PFTBH ^{19}F SNR (blue to green mask). (**F**) Quantification of the individual compound fraction from the total ^{19}F signal volume. (**G**) Quantification of the ^{19}F signal volume of PFCE only and the cumulative ^{19}F volume respectively. * $P<0.05$, ** $P<0.01$, *** $P<0.001$, unpaired Mann-Whitney test in (C), and paired Wilcoxon test in (G).

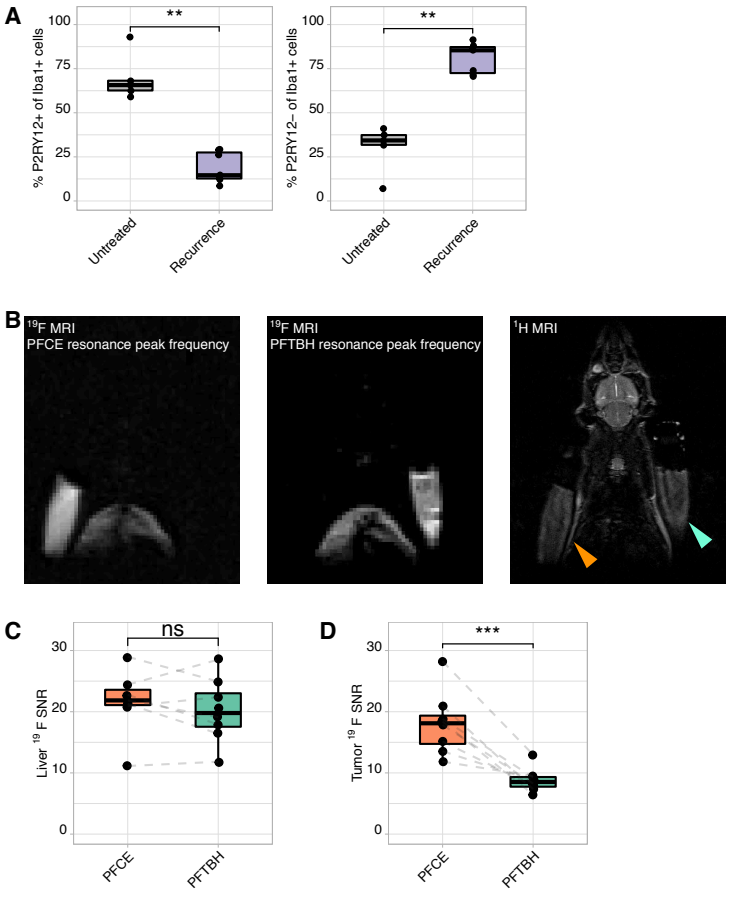

Supplementary Fig. 6. Distinction between PFCE-NP- and PFTBH-NP-associated ^{19}F signals. (**A**) IF quantification of Iba1^{+} P2RY12^{+} MG (left panel) and Iba1^{+} P2RY12^{-} MDMs (right panel) in untreated and IR-recurrent tumors. (**B**) Representative ^{19}F images (left and middle) showing the distinct acquisition of the ^{19}F signal emitted from PFCE-NP-containing reference tube (orange arrow in the ^{1}H MRI image, right) and the PFTBH-NP-containing reference tube respectively (cyan arrow in the ^{1}H MRI image, right). (**C**) Quantification of the ^{19}F signal-to-noise ratio (SNR) of PFCE and PFTBH inside the liver and (**D**) the tumor. * P<0.05, ** P<0.01, *** P<0.001, unpaired Mann-Whitney test in (A) and paired Wilcoxon test in (C) and (D).

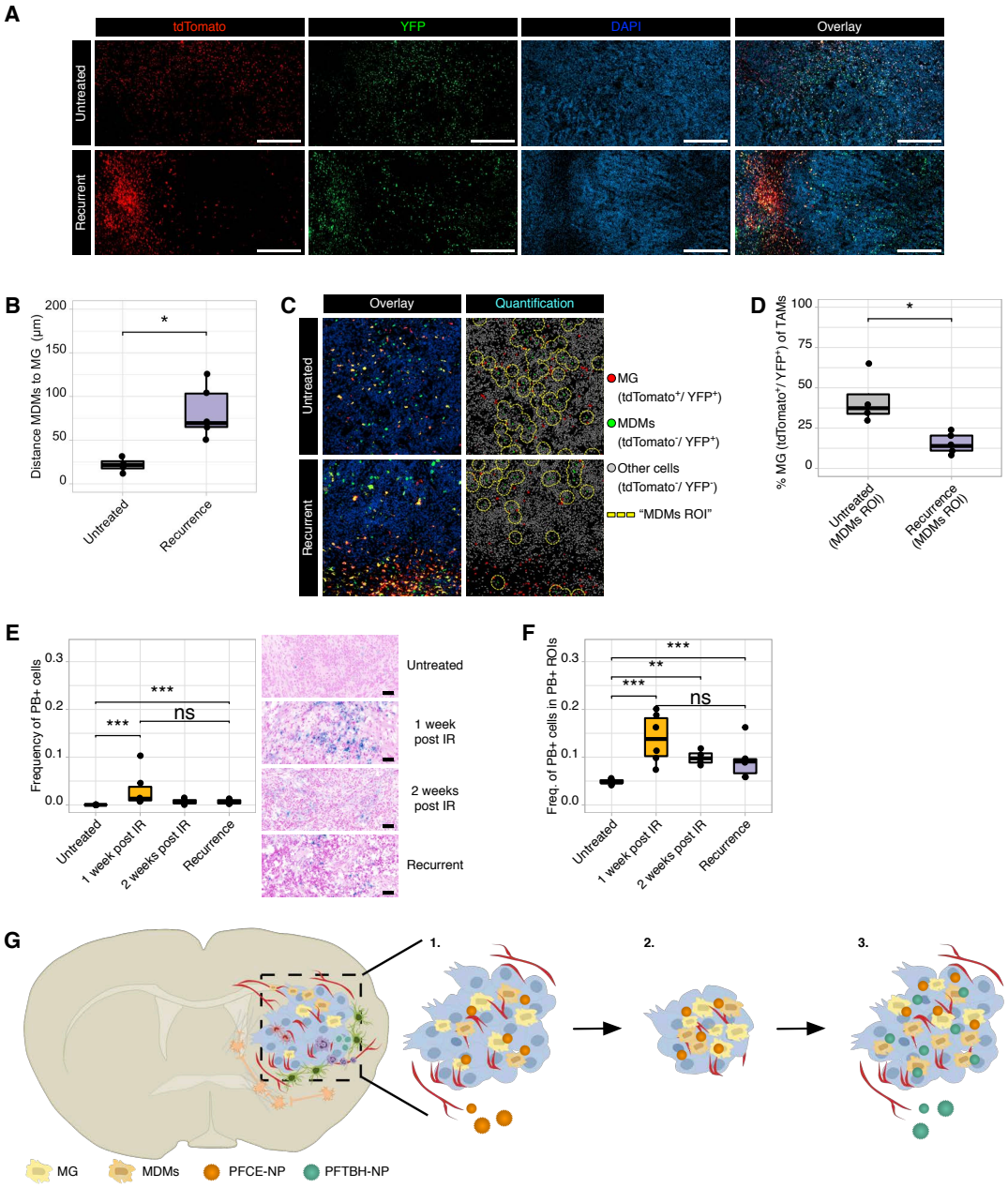

Figure 7. MG and MDMs are differentially distributed in untreated and recurrent gliomas. (**A**) Representative IF images of the MG-specific tdTomato expression and the pan-TAM YFP expression in untreated (above) and IR recurrent (below) PGD-Ink4a/Arf KO gliomas in the CX3CR1 lineage tracing model. Scale bar: 500 µm. (**B**) IF-based quantification of the average distance of YFP^+/$tdTomato^-$ MDMs to YFP^+/$tdTomato^+$ MG. (**C**) *Visiopharm* quantification pipeline showing YFP^+/$tdTomato^+$ MG (red), YFP^+/$tdTomato^-$ MDMs (green) and other non-TAM YFP^-/$tdTomato^-$ cells. The dashed yellow line outlines the "MDM ROI" defined around each MDM nucleus. (**D**) IF quantification of YFP^+/$tdTomato^+$ MG in the "MDM ROI" in untreated and IR-recurrent tumors. (**E**) Prussian blue (PB) staining quantification of PB^+ cells

in tumor tissues at different time points pre- and post-IR and corresponding representative images. Scale bar: 50 µm. (**F**) PB staining quantification of PB^+ cells inside the "PB^+ ROI". (**G**) Schematic model of the cellular, spatial and temporal dynamics of TAMs and their monitoring with PFC-NP and ^{19}F MRI (illustrations were adapted from [10]). *1.* PFCE-NP injection allows the specific labelling of an initial TAM population in the tumor. *2.* Irradiation leads to tumor shrinkage, while TAMs and consequently PFCE-NP become more concentrated. *3.* At tumor recurrence, the TAM subpopulations undergo a subpopulation shift and spatial changes, whereby MDMs become more abundant and distant from MG. The newly infiltrating MDM population is detected by the PFTBH-NP injected at recurrence. * $P<0.05$, ** $P<0.01$, *** $P<0.001$, unpaired Mann-Whitney test.

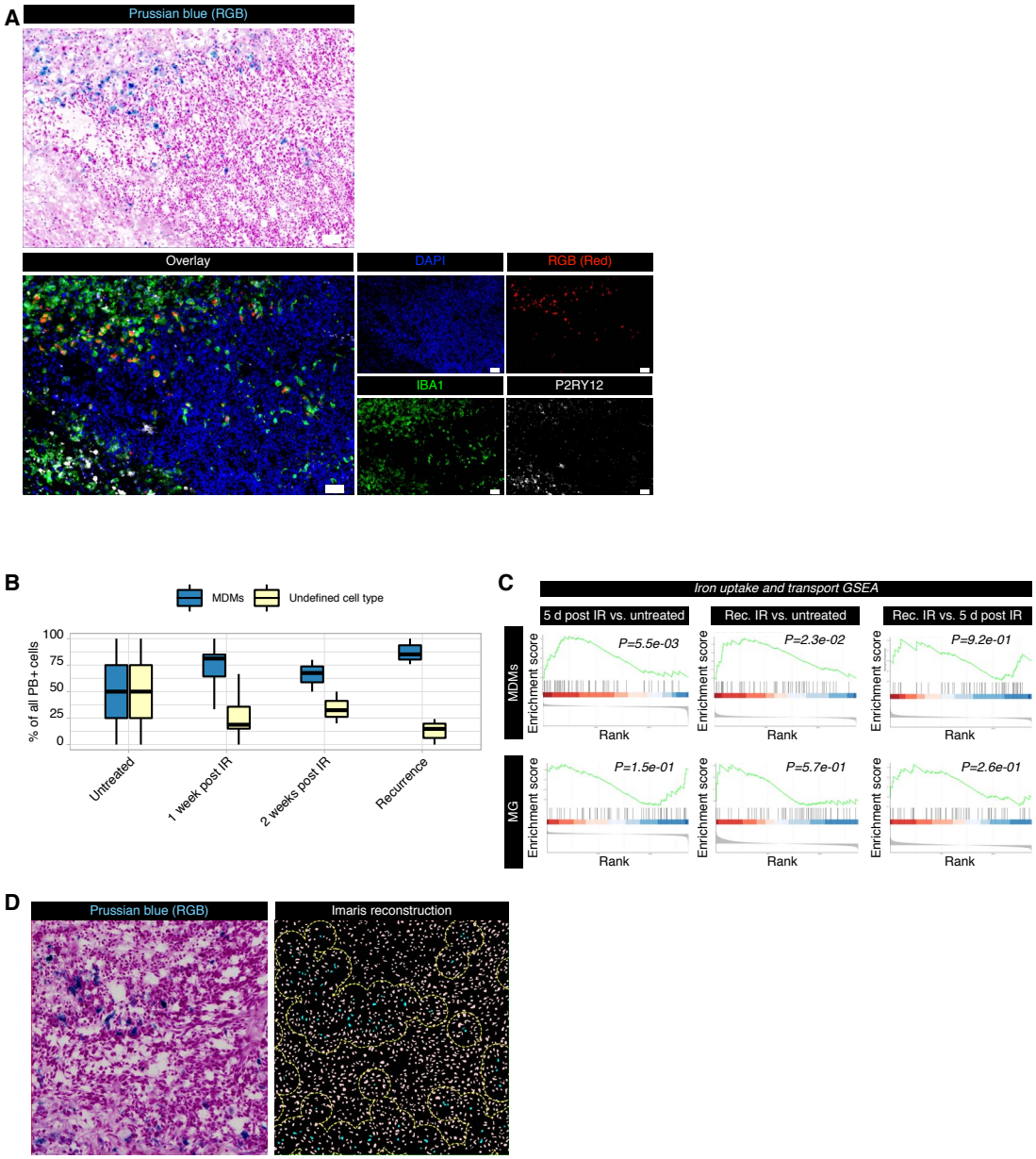

Supplementary Fig. 7. MDMs are the major cellular population involved in iron uptake. (**A**) Representative Prussian blue (PB) images and overlay with IF staining. The red channel from the brightfield PB (red) image was overlaid on the IF staining of Iba1 (green) and P2RY12 (white) allowing the characterization of PB^+ cells. Scale bar: 50 µm. (**B**) Quantification of the cellular origin of PB^+ cells. (**C**) Gene set enrichment analysis (GSEA) results of iron uptake and transport related genes comparing different treatment groups (untreated, 5 days post-IR, IR-recurrent; dataset from [75]) in MDMs and MG. (**D**) *Visiopharm* quantification pipeline showing PB^+ nuclei (cyan) outlined by a "PB^+ ROI" (dashed yellow line) defined around PB^+ nuclei.

6.2 Multimodal imaging of the dynamic brain tumor microenvironment during glioma progression and in response to treatment

Anoek Zomer [1,2] *, Davide Croci [1,2] *, Joanna Kowal [1,2], Leon van Gurp [3], and Johanna A. Joyce [1,2] #

[1] Department of Oncology, University of Lausanne, Lausanne, Switzerland

[2] Ludwig Institute for Cancer Research, University of Lausanne, Lausanne, Switzerland

[3] Department of Genetic Medicine and Development, iGE3 and Centre facultaire du diabète, Faculty of Medicine, University of Geneva, Geneva, Switzerland

* Indicates equal contribution

Correspondence should be addressed to Johanna A. Joyce: johanna.joyce@unil.ch

---

6.2.1 Article text

Cancers develop and progress within complex environments, involving multiple interactions with the surrounding healthy tissue along with newly infiltrating immune cells, which collectively contribute to the regulation of tumor progression and metastasis [160]. The interaction between malignant and non-malignant cells is constantly evolving, impacting disease progression and response to treatment [117]. Given the increasing application of immunomodulatory drugs for the treatment of cancer patients, it is crucial to gain a deeper understanding into dynamically evolving processes within the tumor microenvironment (TME); for example, to determine the optimal therapeutic window for specific anti-cancer treatments, and to reveal mechanisms of acquired or intrinsic resistance [44, 161]. Here we describe a novel multimodal longitudinal imaging approach for high-grade glioma that allows one to study the ongoing interactions between different components of the TME and cancer cells during disease progression and in response to treatment (Fig. 1a). For the first time, we have combined a translationally relevant diagnostic technique, magnetic resonance imaging (MRI) [120], with the power of high-resolution two-photon intravital microscopy (IVM) in the same individuals, to reveal insights into the brain TME at a macroscopical and microscopical level respectively over many weeks (Fig. 1b,c).

To image orthotopic brain tumors in long-term multimodal MRI-IVM experiments, we developed a metal-free cranial imaging window (CIW) setup that is compatible with MRI (Fig. 1b and Supplementary Fig. 1). The CIW was surgically implanted in 4-7-week-old mice, and platelet-derived growth factor-β (PDGF-β)-driven gliomas were simultaneously induced (Supplementary Fig. 2a) [36]. First, a 3-mm diameter craniotomy was made using a biopsy punch and the bone flap was evaluated for the presence of dura mater residuals to confirm that the dura mater and the native environment of the brain remained intact. Subsequently, the site of the craniotomy was sealed with two coverslips that are glued together: one of 3-mm diameter that completely covers the craniotomy and prevents skull regrowth, and one of 5-mm diameter that was used to fix the CIW to the skull. Lastly, a metal-free head bar was placed for the fixation of the mouse under the two-photon microscope and to position the CIW perpendicular to the objective, and the exposed skull was sealed using dental cement. Importantly, the surgical procedure minimally impacted animal welfare, and all the mice had completely recovered before starting to develop tumors 3.5 weeks after induction (Supplementary Fig. 2b,c,d,e).

Analysis of total immune cell infiltrates in glioblastoma patients has revealed that macrophages represent the major immune cell constituent [33, 34] and their accumulation correlates with higher tumor grade [71]. These tumor-associated macrophages (TAMs) include brain-resident microglia (MG) and peripherally-recruited monocyte-derived macrophages (MDMs) [33, 34, 66], which are morphologically distinct and have been shown to display differential migratory behavior *in vivo* [162]. In order to study the longitudinal dynamics of MG and peripherally-recruited immune cells in detail, we employed two different cell-lineage tracing strategies (Supplementary Fig. 3a,b) [66]. To specifically label MG, we used Cx3cr1:CreERT2-IRES-YFP;Rosa26:lslTdTomato mice that express TdTomato in Cx3cr1-expressing cells (MG and circulating monocytes) upon tamoxifen injection [98] (termed CX3CR1 lineage-tracing model). Three weeks after tamoxifen-induced labeling, when blood monocytes are replenished by $TdTomato^-$ cells and only MG remain $TdTomato^+$, we induced green-fluorescent protein $(GFP)^+$ PDGF-β-driven gliomas in order to detect cancer cells in the same model (Supplementary Fig. 3a). Additionally, blood vessels were imaged using fluorescently-labelled dextran, and the extracellular matrix (ECM) was visualized by two-photon second harmonic generation (SHG) imaging (Supplementary Fig. 3a), providing complementary insights into other cellular and non-cellular components of the TME. Finally, by incorporating another lineage-tracing model we sought to investigate the contribution of recruited peripheral immune cells. We therefore used Flt3:Cre; Rosa26:mTmG mice in which all cells of the hematopoietic lineage are labelled with membrane-localized GFP, whereas all

other cells express cell membrane-localized tdTomato (termed FLT3 lineage-tracing model) (Supplementary Fig. 3b) [66, 99].

We first determined whether the implantation of the CIW impacts the composition of the glioma TME or potentially induces an inflammatory response. Flow cytometry analysis of gliomas that developed in the presence or absence of a CIW showed an equal abundance of the major immune cell types, indicating that the CIW surgery does not affect the TME composition (Supplementary Fig. 3c,d,e).

Emerging evidence indicates that the TME can be differentially educated depending on specific genetic alterations in cancer cells [163]. However, how the complex TME changes dynamically over the course of tumor progression and in response to therapy in genetically distinct cancers remains to be fully explored. Therefore, we applied our multimodal imaging method to first investigate the dynamics of MG in PDGF-β–driven gliomas that are deficient for either of the tumor suppressor genes *Ink4a/Arf* or *p53* (Fig. 1a). These tumors closely mimic the genetic profile of patient glioblastomas, in which deletion of *CDKN2A* (encoding for both p16INK4A and p14ARF) is observed in 57.8% of patients, and *p53* mutation/deletion occurs in 27.9% [36, 37, 164].

At 3.5 weeks after glioma initiation and CIW implantation in the CX3CR1 lineage-tracing model, we started weekly MRI to screen for the presence of tumors. As soon as small tumors were detected (<10 mm^3), mice were subjected to weekly MRI and IVM to monitor cellular dynamics during disease progression (Fig. 1a,c and Fig. 2a). Subsequently, advanced gliomas (>30 mm^3) were treated with BLZ945, a potent and highly selective small-molecule inhibitor of the colony-stimulating factor-1 receptor (CSF-1R), that targets macrophages specifically and depletes MG in healthy brain tissue [72]. We have previously shown that secreted factors in the glioma TME protect TAMs from BLZ945-mediated depletion in the PDGF-β; *Ink4a/Arf* deficient model, and consequently, that these surviving TAMs then become anti-tumorigenic [72]. Consequently, we found that BLZ945 treatment regresses high-grade gliomas and significantly prolongs survival in multiple murine glioma models [72, 73].

In the multimodal imaging experiments herein, mice were imaged up to three weeks into the BLZ945 trial, the timepoint at which we observed maximal tumor regression (Fig. 2a). Together, we collected data during the course of three weeks of tumor progression, and three subsequent weeks of response to treatment. To locate the same subpopulation of cells in an individual mouse during each of the IVM sessions, we initially acquired a tile scan of the entire tumor area under the CIW, followed by visual identification of the previously imaged fields-of-view (FOVs) (Fig. 1c). The selected FOVs were intravitally imaged for 30 minutes (time interval = 1 to 2 minutes, Z-step size = 5 µm) to monitor the migration behavior of MG (Supplementary

Movies 1-4). In total, we recorded 80 IVM movies, segmented the different components of the TME (the dura mater as measured by SHG imaging (Supplementary Fig. 4), cancer cells, and MG), tracked the migration of MG, and extracted data for quantification (Fig. 2b). To efficiently analyze the single-cell measurements across the different glioma models and progression/treatment timepoints, we employed the R software environment. We used the SingleCellExperiment Bioconductor software package to store and retrieve information collected from 76,036 MG, including migration speed, morphological features, and normalized dimensionality reduction, along with metadata including MRI-based information (Fig. 2b). Clustering analysis revealed five major clusters (Fig. 2c), and when we investigated the features that distinguish these clusters, we found that cluster 3 is characterized by migratory MG (Fig. 2d), defined as MG that migrate ≥0.05 µm/sec which is equivalent to a track length of 90 µm in a 30-minute time-lapse experiment (Supplementary Fig. 5). Similarly, we analyzed the dataset from the FLT3 lineage-tracing model (Supplementary Fig. 6a,b), but migration speed was not a feature defining any specific cluster (Supplementary Fig. 6c).

It is well-known that in response to injury, MG become activated and migrate to the site of damage where they phagocytose dead cells and debris [165, 166]. Interestingly, we observed that in response to BLZ945, MG become gradually more migratory in both *Ink4a/Arf* and *p53*-deficient gliomas (Fig. 2e, and Supplementary Movies 1-4). These results are in line with earlier experiments, where we found that glioma TAMs become antitumorigenic in response to CSF-1R inhibition by down-regulating M2-like macrophage markers and enhancing phagocytosis [72, 90]. Interestingly, we also identified differences between MG from *Ink4a/Arf* versus *p53*-deficient gliomas. First, MG in *Ink4a/Arf*-deficient gliomas are more migratory compared to MG in *p53*-deficient gliomas, both in advanced lesions before treatment, and in response to BLZ945 (Fig. 2e). Second, whereas MG remain present in both tumor models following treatment initiation, in line with our previous data where we showed that the glioma TME protects MG from BLZ945-mediated depletion in the *Ink4a/Arf*-deficient model [72], MG in *p53*-deficient gliomas were better protected compared to MG in *Ink4a/Arf*-deficient gliomas (Supplementary Fig. 7a). Further analyses revealed that in *p53*-deficient gliomas, the number of tumor cells is more substantially reduced in response to BLZ945 treatment (Supplementary Fig. 7b), suggesting that the abundance of anti-tumorigenic MG in BLZ945-regressing tumors may correlate with treatment response. Future studies will be important to fully elucidate the potential translational implications of these findings.

The combined use of MRI and IVM through a CIW as described herein represents a powerful multimodal platform not only for investigating evolving brain malignancies, but also for any longitudinal studies of progressive neurological disorders. Depending on the choice of the lineage-tracing mouse model and/or other labeling strategies, a plethora of cell types known

to be involved in neuropathology can be visualized, including MG and other immune cells, neurons, astrocytes, oligodendrocytes, and (peri)vascular cells, while simultaneously monitoring the disease by MRI. Moreover, we applied a Bioconductor software package, initially developed for the analysis of single cell RNA sequencing data, to the analysis of large IVM datasets. This will enable more complex and large-scale analyses in this field, for example to predict disease outcome or response to treatment.

6.2.2 Acknowledgements

We thank members of the Joyce lab for insightful discussion, Lucie Tillard and Dr. Marta J.C Jordão for technical support, and Novartis Switzerland for providing BLZ945. We are grateful to the In Vivo Imaging Facility at the University of Lausanne for assistance and advice, in particular Dr. A. Benechet. We thank Dr. E. Holland for generously providing the RCAS vectors and Nestin-Tva mice, and Dr. C. Forsberg for the Flt3:Cre Rosa26:mTmG mice. This research was supported in part by the Swiss Cancer Research Foundation (KFS-3390-08-2016; KFS-5280-02-2021), Charlie Teo Foundation, Ludwig Institute for Cancer Research, and University of Lausanne (to JAJ). AZ was supported in part by a fellowship from the Human Frontier Science Program (LT000240/2017-L).

6.2.3 Materials and Methods

Animals, cells and tumor models

Animals

The Nestin-Tv-a;*Ink4a/Arf*$^{-/-}$ mouse line has been described previously [152] and was generously provided by Dr. Eric Holland. The Nestin-Tv-a and Nestin-Tv-a;*Ink4a/Arf*$^{-/-}$ mouse lines were bred to a C57BL/6 background for 10 generations. *Flt3*:Cre;Rosa26:mTmG mice (C57BL/6 background) were kindly provided by Dr. Camilla Forsberg (UCSC) [99, 167, 168] and bred to Nestin-Tv-a or Nestin-Tv-a;*Ink4a/Arf*$^{-/-}$mice [66]. Only male mice showed expression or transmittance of Cre, and as such only male mice could be used for these experiments. *Cx3cr1*:CreER-IRES-YFP mice (C57BL/6 background; Jackson Labs) were crossed with Rosa26:lsl-TdTomato reporter mice (C57BL/6 background; Jackson Labs), and with Nestin-Tv-a or Nestin-Tv-a;*Ink4a/Arf*$^{-/-}$mice [66]. For the Cx3cr1:CreER-IRES-YFP Rosa26:lsl-TdTomato lineage tracing system, 3-4 week-old mice were injected twice, 48 hours apart, intraperitoneally with 1 mg of tamoxifen citrate (Sigma-Aldrich) dissolved in sunflower seed oil (Sigma). Mice were used for intracranial injection of DF1 cells 3 weeks after tamoxifen

administration (see “Glioma model” section below). All mice were bred within the University of Lausanne animal facilities, and all animal studies were approved by the Institutional Animal Care and Use Committees of the University of Lausanne and Canton Vaud, Switzerland.

Cells

DF1 chicken fibroblasts were obtained from ATCC. RCAS vectors expressing PDGFB-HA, PDGFB-HA-SV40-GFP, or a short hairpin against mouse p53 (shP53) were kindly provided by Dr. Tatsuya Ozawa and Dr. Eric Holland [37, 153]. DF1 cells were transfected with the RCAS vectors using FuGENE 6 (Promega) according to the manufacturer’s instructions. PDGFB-HA-SV40-GFP DF1 cells were sorted for GFP-positive cells by flow cytometry to create a stable GFP-positive DF1 cell line. All cell lines were cultured in DMEM (Life Technologies) supplemented with 10% fetal bovine serum (Life Technologies), and penicillin and streptomycin (Life Technologies) under standard conditions.

Glioma model

4.5 to 7 week-old mice were intracranially injected as previously described [66, 72, 73, 155]. Briefly, mice were fully anesthetized using isoflurane inhalation anesthesia (2% isoflurane/O_2 mixture), and a mixture of 2% lidocaïne (Streuli Pharma) and 0.5% bupivacaine (Carbostesin; Aspen Pharma Schweiz) was applied as a local anesthetic (50 µl per mouse), and 0.3 mg/ml buprenorphine (Temgesic; Indivior Schweiz) was given subcutaneously as a systemic anesthetic (100 µl per mouse). Using a stereotactic apparatus, cells were injected into the right frontal cortex (2 mm frontal, 1.5 mm lateral from bregma, 2 mm deep). For the *p53*-deficient glioma model, 3 x 10^5 DF1 cells (a 1:1 mixture of RCAS-PDGFB-HA/PDGFB-HA-SV40-GFP DF1 cells and RCAS-shP53 DF1 cells) were injected, and for the *Ink4a;Arf*-deficient glioma model, mice were injected with 2 x 10^5 RCAS-PDGFB-HA/PDGFB-HA-SV40-GFP DF1 cells. The skin incision was sealed with Vetbond tissue adhesive (3M), and the mouse was placed on a heating pad and monitored until fully recovered from anesthesia. Finally, Bepanthen cream (Bayer) was applied on the incision site before placing the animal back in the cage, and subsequently following each mouse by regular monitoring.

Cranial window surgery

Mice were fully anesthetized using isoflurane inhalation anesthesia (2% isoflurane/O_2 mixture) and prepared for surgery by shaving and cleaning the head with 70% ethanol pads (Fisher Healthcare) and 10% betadine pads (Purdue Products L.P.). A mixture of 2% lidocaïne (Streuli Pharma) and 0.5% bupivacaine (Carbostesin; Aspen Pharma Schweiz) was applied as a local anesthetic (50 µl per mouse), and 0.3 mg/ml buprenorphine (Temgesic; Indivior Schweiz) was given subcutaneously as a systemic anesthetic (100 µl per mouse). A longitudinal incision of

the skin was made between the occiput and forehead, and the skin covering the skull was cut in a circular manner, by removing approximately 3 mm of the skin edges on each side. After cleaning and drying the skull with a cotton swab, the bone was etched mechanically with a scalpel (by making a pattern of crosses) and chemically by applying 35% phosphoric acid solution (Santa Cruz Biotechnology) with a cotton swab. The skull was then cleaned several times with Ringer's solution (Dutscher), and the mouse was placed into a stereotactic device with a three-axis micromanipulator and an integrated heating pad (Stoelting). A 3-mm craniotomy was made using a 3-mm biopsy punch (Integra Miltex), ensuring precise fitting of the imaging window. The exposed cortical surface was kept moist with Ringer's solution. Tumor cells were injected into the brain parenchyma at the craniotomy site as described in the previous section. The brain surface was sealed with a 0.085-mm-thick 3-mm diameter coverslip (Multichannel Systems) that was glued to a 0.085-mm-thick 5-mm diameter coverslip (Multichannel Systems) using Norland optical adhesive 61 (AMP Technica). The outer edges of the 5-mm coverslip were used to fix the imaging window to the skull using super glue (Loctite). A small head bar was fixed using super glue (Loctite), allowing later fixation of the mouse's head during the intravital imaging experiments. Lastly, dental acrylic glue (Kulzer) was applied on the skull surface, covering also a small rim of the 5-mm coverslip. The animal was then placed on a heating pad and monitored until it had fully recovered and was returned to the cage, followed by regular monitoring.

Monitoring and scoring

Upon recovery from anesthesia after the cranial window surgery, mice underwent visual observation every few hours for the first 24 hours. To ensure pain relief, paracetamol (Bristol-Myers Squibb) was added to the drinking water (500 mg/250 ml) for 7 days post-operatively. Mice were monitored at least once a day for any signs of distress as well as for brain tumor symptoms, including lethargy, poor grooming, weight loss, and in rare instances macrocephaly or hemiparesis. For each sign, a severity-dependent score of 1 to 3 was given. In case of a cumulative score of 10, or any individual score of 3, mice were immediately euthanized.

BLZ945 treatments

BLZ945 was obtained from Novartis, Switzerland, in solid state (BLZ945-AA (HCL Salt)). For in vivo experiments, BLZ945 was dissolved in 20% Captisol (w/v) (Ligand Pharmaceuticals) in H_20 and stirred overnight to obtain a clear solution. Dissolved BLZ945 was administered daily at 200 mg/kg by oral gavage.

Tissue analysis

Brain slice harvesting and imaging

Mice were sacrificed by terminal anesthesia using pentobarbital (CHUV, Lausanne, Switzerland), followed by transcardial perfusion with PBS. Tumor-bearing brains were harvested and placed on ice in “slicing medium” (minimum essential media 2 mM l-glutamine (MEM GlutaMAX, Life Technologies), 4.5 mg/mL glucose (Life Technologies), 100 U/mL penicillin-streptomicin (P/S, Life Technologies)). The brain was then fixed on the specimen plate of a vibratome (Leica) with super glue (Loctite). The brain was held in place with 2% agar cubes to additionally support the tissue while slicing, and submerged into “slicing medium” in the buffer tray. The vibratome was set at a moving speed of 0.5 mm/s, a vibration amplitude of 1 µm, and 425-µm-thick coronal slices were cut sequentially and placed into “culturing medium” (MEM GlutaMAX, 4.5 mg/mL glucose, 100 U/mL P/S, 25% HBSS (Life Technologies), 25% heat-inactivated normal horse serum; re-supplement: 1X GlutaMAX (Life Technologies), 1X non-essential amino acids (Life Technologies), 1:50 1M HEPES (Life Technologies)) on ice. 3 to 4 slices per mouse were placed on a microscope slide (Fisher Scientific) and enclosed by a layer of 732 multi-purpose sealant (Dow) to create a small bucket which was then filled with a small amount of “culturing medium”, and finally enclosed by a coverslip (Menzel-Gläser). Images were acquired using an upright Leica TCS SP8 DIVE multi-photon microscope (Mannheim, Germany) equipped with a 16x (HC FLUOTAR L N.A. 0.6 FWD 2.5 mm) multi-immersion objective with the same imaging parameters as for IVM (see “Intravital imaging” section below).

Flow cytometry

Mice were sacrificed by terminal anesthesia using pentobarbital (CHUV, Lausanne, Switzerland), followed by transcardial perfusion with PBS. The brain tumor was macrodissected and dissociated using the Brain Tumor Dissociation Kit (Miltenyi). The dissociated tissue was filtered through a 40 µm mesh filter and then underwent myelin removal using the Myelin Removal Beads Kit (Miltenyi). The resulting myelin-free single cell suspension underwent red blood cell lysis for 10 minutes on ice using 10x red blood cell lysis buffer (Biolegend). The single cell suspension was stained with the Zombie-near-infrared fixable viability kit (Biolegend) for 20 minutes at room temperature (RT), washed with FACS buffer (2 mM EDTA (Life Technologies) and 0.5% BSA (Jackson ImmunoResearch) in PBS (CHUV hospital Lausanne, Switzerland)) and then FC-blocked (BD Biosciences) for 30 minutes on ice. After washing with FACS buffer, cells were incubated with directly-conjugated antibodies (table 1). Stained samples were washed 3 times with FACS buffer and acquired on a BD Fortessa at the Flow Cytometry Core Facility of University of Lausanne.

Immunofluorescence staining and imaging of the dura mater

Mice were sacrificed by terminal anesthesia using pentobarbital (CHUV, Lausanne, Switzerland), followed by transcardial perfusion with PBS. The skull was collected and fixed overnight in periodate-lysine-paraformaldehyde (PLP) buffer at 4°C. The dura mater was then manually removed from the skull bone, placed in a 24-well plate and washed for 10 minutes in 500 µL of PBS on a shaker at RT. The dura mater was then permeabilized and blocked for 2 hours with TritonX-100 0.5% (AppliChem) and 5% normal donkey serum (NDS) (EMD Millipore) in PBS (CHUV, Lausanne, Switzerland) on a shaker at RT. After removal of the permeabilization/blocking buffer, the dura mater was incubated for 20 hours in 300 µL of primary antibody mix (table 1) diluted in 5% NDS/PBS on a shaker at 4°C. After washing 3 times (10 minutes each) in 500 µL PBS on a shaker at RT, the sample was incubated for 2 hours with 300 µL of secondary antibody mix (table 1) diluted in 5% NDS/PBS on a shaker at RT (protected from the light). After washing 3 times (10 minutes each) in 500 µL PBS on a shaker at RT, the sample was incubated for 15 minutes in 300 µL DAPI (Life Technologies) (1:5000 in PBS) on the shaker at RT. The dura mater was placed on a glass slide (Fisher Scientific), mounted with Dako fluorescence mounting medium (Agilent), and covered with a coverslip (Menzel-Gläser). Images were acquired using an upright Leica TCS SP8 DIVE multi-photon microscope (Mannheim, Germany) equipped with a 16x (HC FLUOTAR L N.A. 0.6 FWD 2.5 mm) multi-immersion objective corrected for imaging with H_2O. The imaging parameters were similar to the parameters used for IVM (to visualize SHG signal, GFP and tdTomato - see “Intravital imaging” section below), and the 633 nm laser was used to visualize the collagen type I antibody that was labeled with AF647.

In vivo imaging of mice

Magnetic resonance imaging (MRI)

MR imaging was performed using a 3 Tesla Small Animal MR Scanner (Bruker BioSpec) with a volume coil as transmitter and a 2x2 channel surface coil for signal reception. The mouse was fully anesthetized with 1-2% isoflurane/oxygen inhalation and placed on the imaging bed with the head hold in place below the surface coil, while monitoring respiratory rate and temperature. Data acquisition was performed using the Paravision 360 v2.0 software (Bruker). A 3-slice localizer was performed to assess the mouse head position, followed by a 2D T2-weighted acquisition (turbo rapid acquisition relaxation enhancement (Turbo-RARE), repetition time (TR) 3000 ms, echo time (TE) 75 ms, number of averages (NA) 6, number of slices 10, slice thickness (ST) 0.7 mm, FOV 20 x 20 mm, pixel size 156 x 156 µm, echo train length (ETL) 12, acquisition time (AT) 3 min) with images being acquired in axial planes. After

imaging, the mouse was returned to the cage and monitored until it regained consciousness. Volumetric analysis of the gliomas was performed on MR image DICOM files using the MIPAV software (National Institutes of Health, USA).

Intravital 2-photon imaging

Mice were sedated using isoflurane inhalation anesthesia (3% isoflurane/O_2 mixture) and mice that were used for vascular imaging were intravenously injected with Pacific Blue-labeled 500 kDa dextran (both Thermo Fisher Scientific, and prepared according to the manufacturers' instructions). Mice were fixed with their head-bar to a custom-designed mouse holder, and the concentration of isoflurane was lowered to 0.8-1.2% to keep the mice lightly sedated, characterized by a constant and non-forced breathing pattern. This level of isoflurane is optimal for imaging sessions up to several hours, and it minimizes motion-induced image deformation caused by irregular breathing. The mouse was placed in the climate chamber surrounding the microscope, keeping the whole stage of the microscope and the objectives at 34°C. Imaging was performed on an upright Leica TCS SP8 DIVE multi-photon microscope (Mannheim, Germany) with an InSight X3 tunable laser (Spectra Physics) and two non-descanned hybrid 4Tune detectors. SHG imaging was performed using a wavelength of 810 nm for excitation, and 380-420 nm for detection. GFP and tdTomato were excited with a wavelength of 960 nm, and detected between 500-540 nm and 570-670 nm respectively. Pacific Blue-labeled dextran was excited using a wavelength of 810 nm, and detected between 435-480 nm. All images were acquired with a 16x (HC FLUOTAR L N.A. 0.6 FWD 2.5 mm) multi-immersion objective. The objective was corrected for imaging with Immersol W 2010 (Carl Zeiss) and a coverslip thickness of 0.17 mm. For each mouse, a tile scan of the whole CIW was taken. Afterwards, two individual time-lapses of 30 minutes each were acquired. The exact location of previously acquired fields-of-view was retrieved by visual identification of clear landmarks such as SHG imaging patterns and vasculature, as well as by using previously saved coordinates of the stage of the microscope.

Data analysis

Imaris

High-resolution three-dimensional time-lapse images were imported into Imaris version 9.7.2 (Bitplane). Before cell/structure classification and segmentation, images were corrected for bleed-through using the channel arithmetic function. MG, tumor cells, and ECM (as measured by SHG imaging) were classified and segmented using the surface creation tool. Features of individual surfaces were exported as .csv files for each individual time-lapse.

Data import into R

Individual .csv files per imaging session were loaded into R version 4.0.2, using R Studio version 1.4.1103. For each imaging session, the following features were extracted per cell: shortest distance of MG to SHG, shortest distance of MG to tumor cells, displacement length, track duration, ellipticity oblate, ellipticity prolate, intensity of GFP, intensity of tdTomato, track length, number of surfaces, track position, track speed, volume, sphericity, and track straightness. For the features “shortest distance of MG to SHG” and “shortest distance of MG to tumor cells”, a measurement was made for each imaged timepoint during that imaging session. From these individual values, a mean value was calculated of all timepoints using the dplyr package version 1.0.3. All other features were exported from Imaris as mean values of all timepoints. Thus, a single value was obtained for each feature and for each cell per imaging session. All cells from all imaging sessions of all mice were then agglomerated, with annotation for track position (x, y and z), number of surfaces, track duration, imaging date, mouse ID, imaging position, surface, tracing model, tumor model, tumor volume as measured by MRI, BLZ945 start date, the day relative to BLZ945 start date, uniform timepoint, and comments in the metadata. This resulted in a dataset of 76,036 MG with 12 features, and 16 metadata categories.

Scaling, dimensionality reduction and clustering

Data were loaded into an S4 object of the SingleCellExperiment class, using the SingleCellExperiment package version 1.10.1, with the data added to the counts assay and metadata loaded in colData. For dimensionality reduction and clustering, data were scaled and centered. For missing data (some imaging timepoints were missing data for shortest distance to SHG or tumor cells), NAs were replaced with the mean for that feature of all other cells. Scaled data were added to the normcounts assay of the SingleCellExperiment class object. PCA was performed using the prcomp function, and UMAP dimensional reduction was calculated using the RunUMAP function from the Seurat package version 4.0.1, both using default settings. Both dimensional reductions were added to the SingleCellExperiment class object. Clustering was performed by consecutively running the FindNeighbors (k.param set to 30) and FindClusters (resolution set to 0.19) functions from the Seurat package version 4.0.1 on the scaled data. Clustering classifications were added as ‘clust’ to the colData of the SingleCellExperiment class object.

Data visualization

Data were plotted using GraphPad Prism version 9.0.1 or in R using the ggplot2 package, version 3.3.3. Labels were plotted using the ggrepel package, version 0.9.1, and color

schemes were used from viridis package, version 0.6.0. For visualization, the data in the counts assay, not the scaled data in the normcounts assay, were plotted.

Statistics

GraphPad Prism version 9.0.1 or R Studio was used for all data analysis. Parametric data were analyzed by a two-tailed Student's t-test. Non-parametric data were analyzed by a Mann-Whitney test on ranks. $P<0.05$ was considered as statistically significant in all cases. Adoption of one statistical test or the other is indicated for each experiment in the figure legend.

Table 1: Antibodies used in the study

Antibodies							
Target	**Species**	**Antibody**	**Manufacturer**	**Clone**	**Category number**	**Dilution**	**Application**
Ly-6C	Rat	Anti-mouse Ly-6C Brilliant Violet 711	BioLegend	HK1.4	128037	1:800	Flow cytometry panel #1
Ly-6G	Rat	Anti-mouse Ly-6G Brilliant Violet 605	BioLegend	1A8	127639	1:160	Flow cytometry panel #1
CD11b	Rat	Anti-mouse CD11b BUV661	BD Biosciences	M1/70	612977	1:800	Flow cytometry panel #1, Flow cytometry panel #2
CD49d	Rat	Anti-mouse CD49d PE/Cy7	BioLegend	R1-2	103618	1:160	Flow cytometry panel #1
CD45	Rat	Anti-mouse CD45 Alexa Fluor 700	BioLegend	30-F11	103128	1:200	Flow cytometry panel #1, Flow cytometry panel #2
CD3	Hamster	Anti-mouse CD3e BUV395	BD Biosciences	145-2C11	563565	1:75	Flow cytometry panel #1 and #2
NK-1.1	Mouse	Anti-mouse NK-1.1 Brilliant Violet 421	BioLegend	PK136	108741	1:640	Flow cytometry panel #1
CD19	Rat	Anti-mouse CD19 Brilliant Violet 605	BioLegend	6D5	115539	1:320	Flow cytometry panel #2
NK-1.1	Mouse	Anti-mouse NK-1.1 Brilliant Violet 711	BioLegend	PK136	108745	1:640	Flow cytometry panel #2
Collagen I	Rabbit	Anti-mouse collagen I	Abcam	Polyclonal	ab34710	1:100	Immunofluorescence panel #1
YFP	Chicken	Anti-GFP (cross-reactive to YFP)	Abcam	Polyclonal	ab13970	1:1000	Immunofluorescence panel #1
Chicken IgG (H+L)	Donkey	Anti-chicken IgG Alexa Fluor 488	Jackson ImmunoResearch	Polyclonal	703-545-155	1:500	Immunofluorescence panel #1
Rabbit IgG (H+L)	Donkey	Anti-rabbit IgG Alexa Fluor 647	Invitrogen	Polyclonal	A31573	1:500	Immunofluorescence panel #1

Flow cytometry panels #1 and #2 have been used in experiments presented in figure S3
Immunofluorescence panel #1 has been used in experiments presented in figure S4

6.2.4 Figures

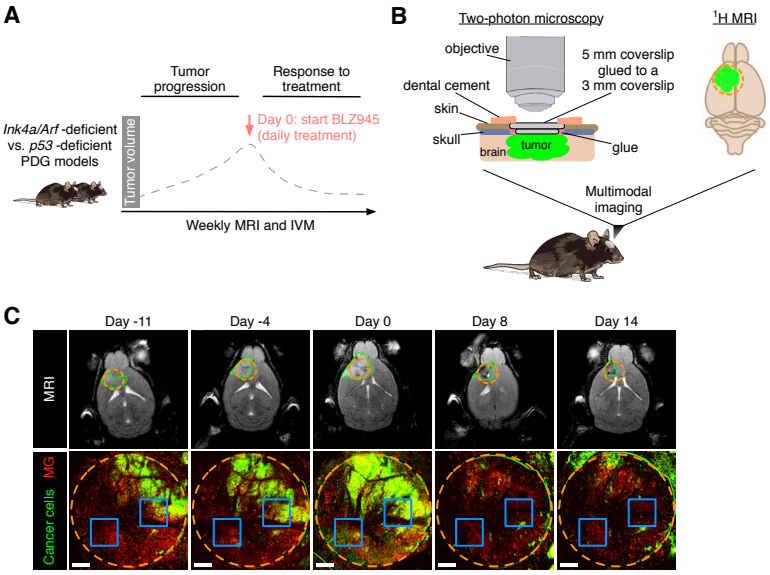

Figure 1. Multimodal IVM-MRI imaging to visualize dynamics of the brain TME over multiple weeks. (**A**) Schematic showing the experimental design used to investigate TME dynamics during tumor progression and in response to BLZ945 treatment in *Ink4a/Arf*-deficient and *p53*-deficient gliomas. Mice were imaged weekly to assess tumor growth by MRI and to monitor TME dynamics by IVM. The dashed gray line indicates an illustrative tumor growth curve. (**B**) In order to obtain visual access to the brain tumor and perform multimodal IVM-MRI, a CIW was surgically implanted in the mouse skull at the site of tumor induction (left). The use of metal-free components allowed the concomitant use of MRI (right). The dashed orange circle indicates the position of the CIW on the top of the tumor (green). (**C**) Representative example of longitudinal multimodal imaging of the same mouse by MRI and IVM before and after treatment with BLZ945 (treatment start at day 0). The upper MRI images show the anatomical location of the tumor (green line) and the projection of the CIW position (dashed orange circle). The lower panels show matching two-photon microscopy tile scans visualizing the dynamics of GFP^+ cancer cells (green) and $tdTomato^+$ MG (red) through the CIW (dashed orange circle). The blue squares indicate an example of the location of two FOVs that were used to record time-lapses throughout the duration of the longitudinal IVM-MRI imaging experiment. Scale bars: 400 µm. Brain silhouette in (B) was sourced from https://scidraw.io/.

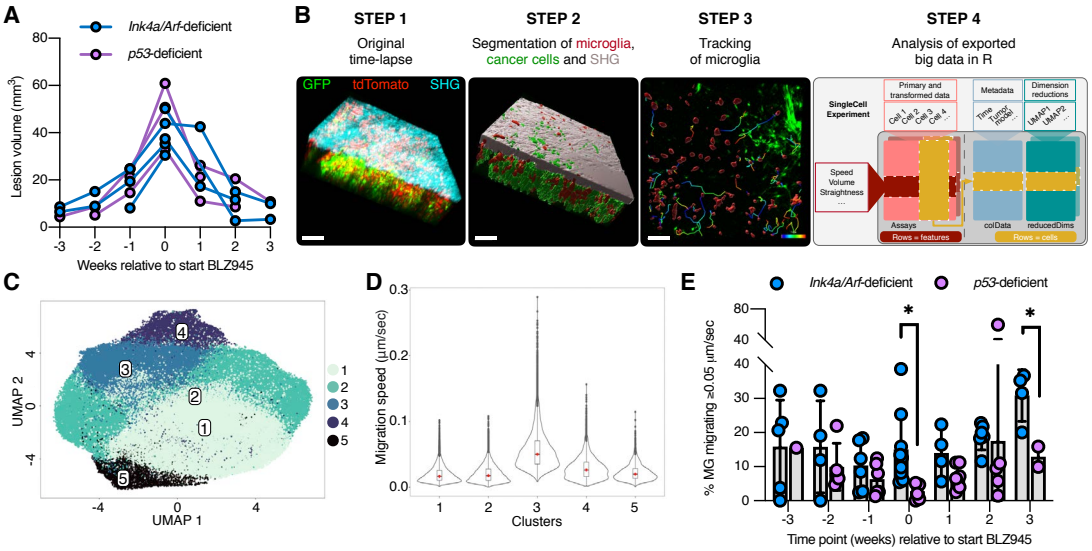

Figure 2. Analysis of a large IVM dataset reveals temporal dynamics of MG during the treatment of high-grade glioma. (**A**) Tumor volume curves from weekly MRI of *Ink4a/Arf*- or *p53*-deficient glioma-bearing mice. Two key phases can be observed: tumor growth in the 3 weeks preceding BLZ945 treatment (start = timepoint 0), and tumor regression in the 3 weeks post-treatment initiation. (**B**) Analysis pipeline of IVM data collected from *Ink4a/Arf*- or *p53*-deficient glioma-bearing mice (CX3CR1 lineage tracing model) that were intravitally imaged at different stages of tumor progression or therapy response. After segmentation of the different components of the glioma TME in each of the 30-minute time-lapse experiments (step 1 and 2), MG are tracked (step 3). Of note, we did not observe migration of cancer cells in the total duration of the time-lapse. We extracted data from 80 movies that were collected from 5 *Ink4a/Arf*-deficient gliomas and from 3 *p53*-deficient gliomas, measuring in total 76,036 MG, and used the SingleCellExperiment Bioconductor package to store, organize and analyze the data. Scale bars: 100 µm. (**C**) UMAP visualization of MG clusters. (**D**) Violin plots show the migration speed of MG in each of the clusters (the cluster numbers correspond to the IDs shown in (C)). (**E**) Percentage of migrating MG in *Ink4a/Arf*- or *p53*-deficient gliomas at each of the stages of tumor progression (timepoints -3, -2, -1 and 0) and in response to BLZ945 (timepoints 1, 2 and 3) (Student's t-test, * indicates P<0.05). Each dot represents one FOV.

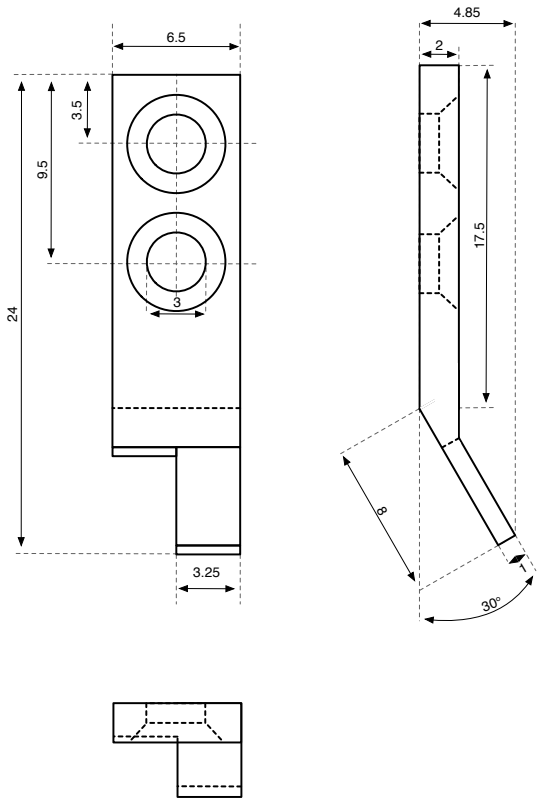

Supplementary Fig. 1. Head-bar schematic. Head bars were made from polyether ether ketone (PEEK) and were produced by 3D printing. Metric unit: mm.

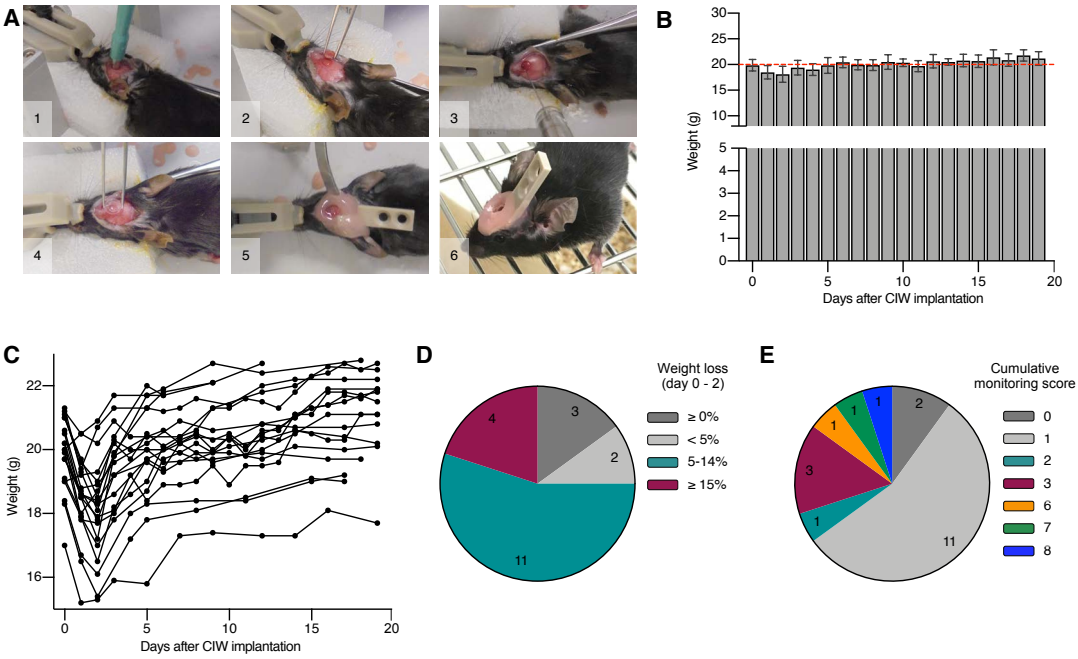

Supplementary Fig. 2. Mice show a rapid and full recovery after CIW implantation. (**A**) Fully anaesthetized mice are placed on a heated stereotactic frame. A 3 mm biopsy punch is used to remove a circular fragment of the skull (images 1 and 2). DF1 cells are then injected with a high-precision Hamilton's syringe to induce tumor formation (image 3). Afterwards, the skull is closed by applying the cranial imaging window which is fixed with super-glue and dental cement. Simultaneously, a head-bar is placed which will allow the mouse's head to be stabilized at the two-photon microscope and to avoid breathing-associated movements (image 4 and 5). The mouse is then returned to the cage and monitored while recovering from the surgery and anesthesia (image 6). (**B**) Mouse weight monitoring after surgery and (**C**) individual weight curves (n=20), showing a rapid recovery of body weight. The dashed red line shows the mean weight on the day of surgery. (**D**) Weight loss 2 days after surgery showing only 2 out of 20 mice with a weight loss greater than 15% of their initial weight. (**E**) Evaluation of the overall mouse welfare 2 days post-surgery (see Methods for a detailed description of the monitoring scoring system).

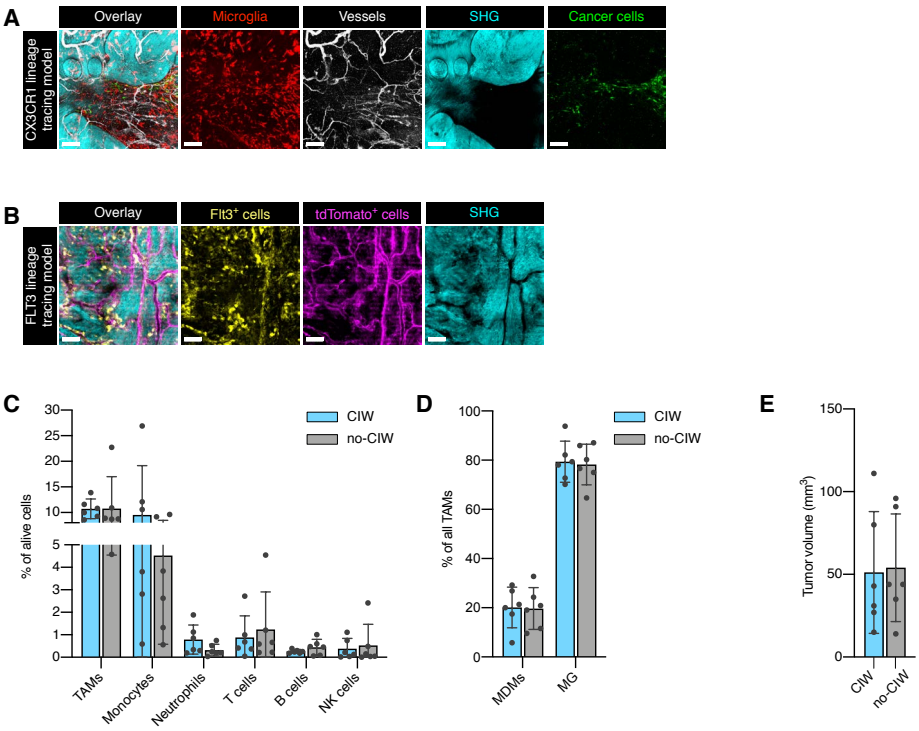

Supplementary Fig. 3. TME characterization of lineage-tracing mouse models. (**A**) Representative two-photon microscopy images of the CX3CR1 lineage-tracing model showing tdTomato-expressing MG (red), dextran-Pacific Blue-labeled vessels (white), SHG imaging signal (cyan), and GFP-expressing cancer cells (green). (**B**) The FLT3 lineage-tracing model allows the detection of Flt3^{+} GFP-expressing immune cells (yellow), ectopic tdTomato mainly expressed in vessel-like structures (violet) and SHG imaging signal (cyan). Scale bars: 150 µm. (**C**) and (**D**) Flow cytometry analysis shows an equal abundance of the major immune cell types in glioma-bearing mice with and without a CIW (paired Wilcoxon test, no statistical differences were observed). Each dot represents one tumor. (**E**) Endpoint volume of the tumors (measured by MRI) that were characterized by flow cytometry in (C) and (D) (Mann-Whitney test, no statistical difference was observed). Each dot represents one tumor.

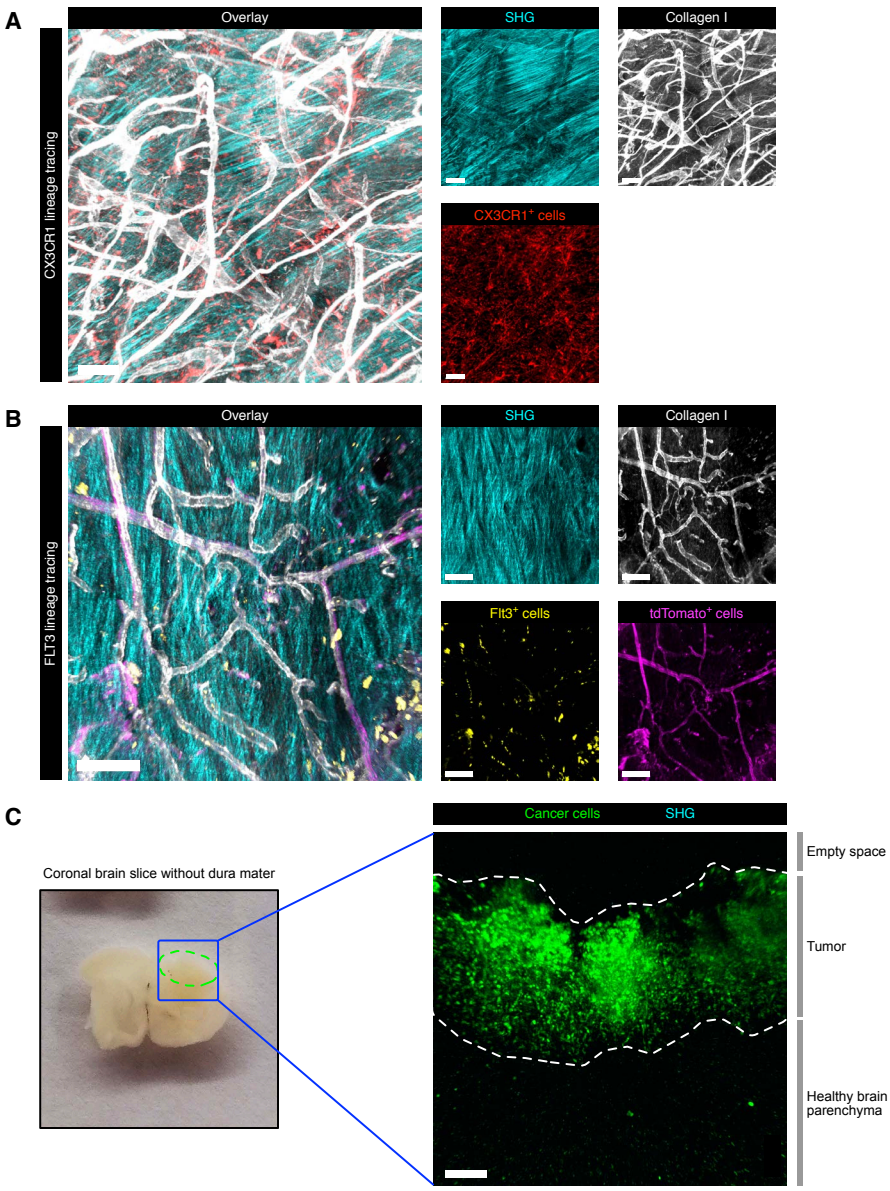

Supplementary Fig. 4. The dura mater, but not the brain parenchyma, shows SHG imaging signal. (**A**) and (**B**) Representative two-photon microscopy images of the dura mater dissected from glioma-bearing CX3CR1 lineage-tracing mice (A) and FLT3 lineage-tracing mice (B) show SHG signal. Scale bars: 100 μm. (**C**) 425-μm-thick tumor-bearing brain slices without dura mater (left, tumor area outlined by the dashed green line) imaged by two-photon microscopy (right) show GFP^+ cancer cells and the adjacent healthy brain parenchyma, but no SHG signal. Scale bars: 100 μm.

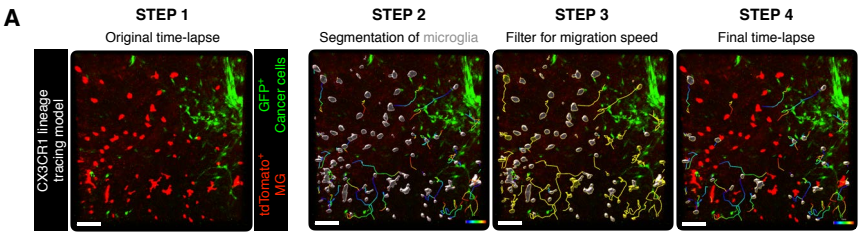

Supplementary Fig. 5. Filtering of migrating MG. (**A**) Cells are segmented and their movement is tracked over the entire course of the time-lapse (steps 1 and 2). Then, cell speed is used to discriminate migratory cells from stationary cells (yellow lines, track speed ≥ 0.05 μm/s, steps 3 and 4). Scale bars: 100 μm. Color-coded tracks display time through the time-lapse (blue indicates the start, and red indicates the end of the imaging acquisition).

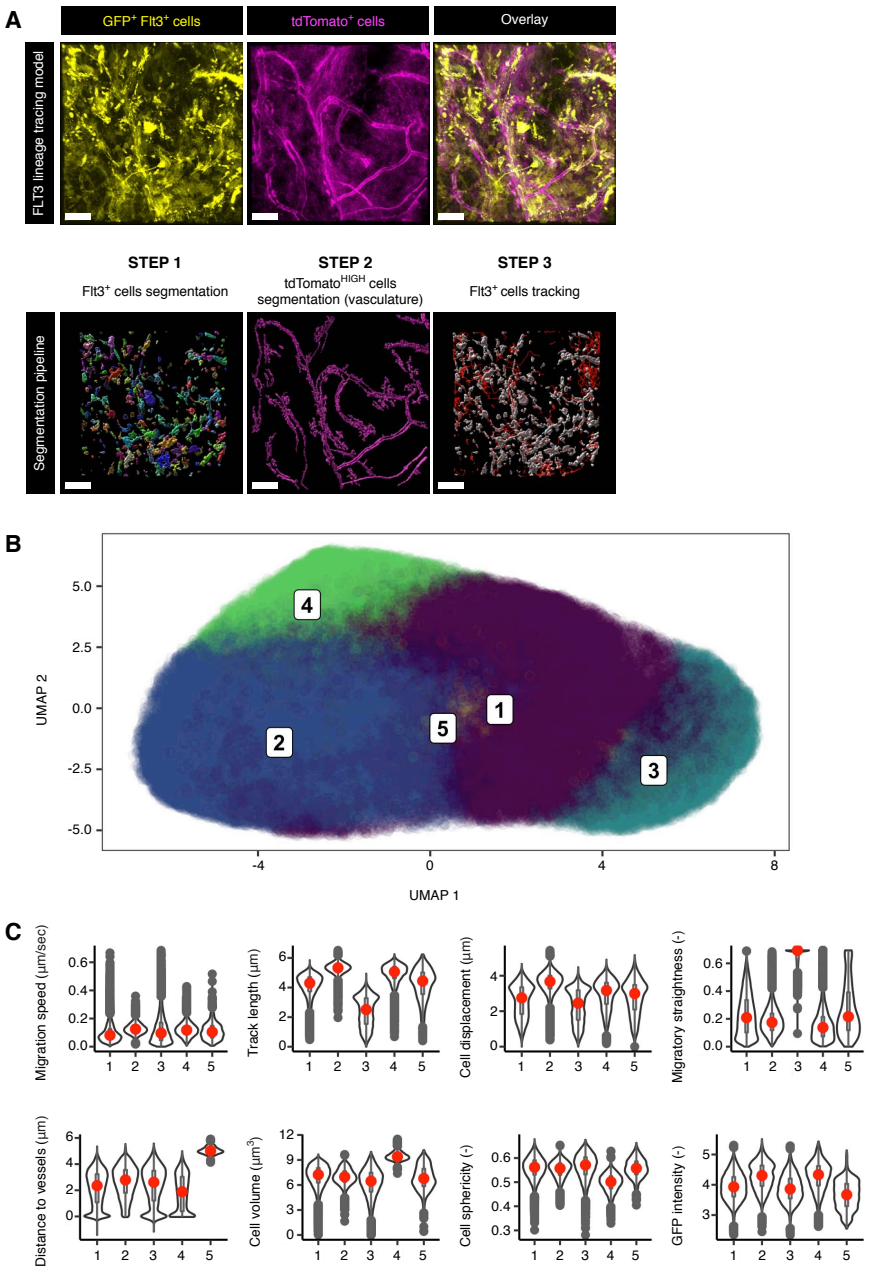

Supplementary Fig. 6. Dimensionality reduction analysis reveals distinct cells clusters in the FLT3 lineage-tracing model. (**A**) Segmentation and migration analysis of the FLT3 lineage tracing model. GFP$^+$Flt3$^+$ or tdTomato$^+$ cells (upper panel) were segmented in order to identify Flt3$^+$ peripheral immune cells (step 1) and highly tdTomato-expressing cells highlighted the vasculature (step 2). Flt3+ cell migration was tracked as the final step (step 3). (**B**) UMAP visualization of Flt3+ cell clusters. (**C**) Violin plots showing the different cell features in each of the clusters (the cluster numbers correspond to the IDs shown in (A)). Y-axis are displayed as logarithmic scale.

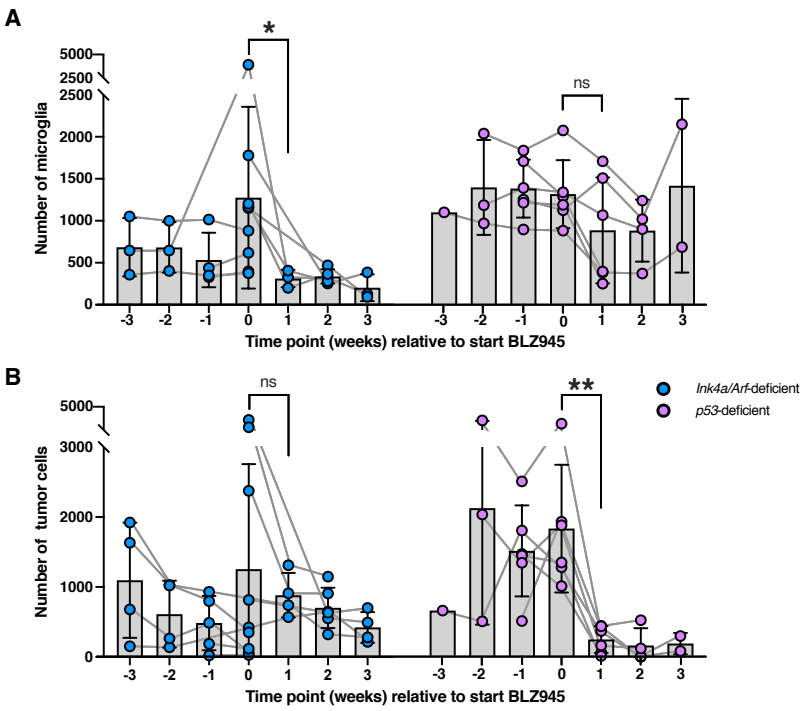

Supplementary Fig. 7. MG and tumor cell dynamics during tumor progression and in response to BLZ945. (**A**) Quantification of the number of MG and (**B**) tumor cells, in both *Ink4a/Arf*-deficient and *p53*-deficient gliomas. Each dot represents the number of cells in one FOV (Student's t-test, ns: not significant, * indicates P<0.05, and ** indicates P<0.01).

Supplementary Movies 1-4. Illustrative time-lapse movies of the *Ink4a/Arf*-deficient (movies 1 and 2) and the *p53*-deficient glioma models (3 and 4), two weeks before (1 and 3) and two weeks after (2 and 4) treatment initiation with BLZ945. MG are shown in red and tumor cells in green, and the total duration of each time-lapse is approximately 30 minutes with an interval of 1-2 minutes between each frame.

6.3 Combinatorial targeting of the glioma TME

6.3.1 Study rationale

Therapeutic targeting of TAMs can be achieved via a substantial arsenal of different agents which interfere with different signaling pathways involved in shaping the phenotype of these cells [76, 169]. With regard to CSF1R inhibition, several reports have shown that this treatment can lead to phenotypic reprogramming of TAMs, while in other studies blockade of this key signaling pathway led to TAM killing and overall cell depletion [76, 89].

For my first thesis project, I investigated the effects of an antibody targeting the extracellular ligand-binding domain of murine CSF1R (termed 2G2 antibody, developed by Roche Pharmaceuticals) [88]. Part of the rationale for using 2G2 was that it should be highly specific for targeting CSF1R and therefore may elicit a stronger pathway inhibition compared to small molecule inhibitors, which potentially can have off-target effects on other tyrosine kinases [89]. To bridge our studies with the clinical situation at the time these experiments were performed, we also sought to investigate combinatorial strategies including irradiation (IR). I additionally combined 2G2 with antiangiogenic treatment (A2V antibody from Roche, targeting Ang2 and VEGF-A signaling), with the rationale that this might synergize with targeting of TAMs, given that macrophages can modulate vascular functions through multiple mechanisms [65, 170, 171].

In order to complement our therapeutic strategies, we also investigated other experimental approaches to modulate CSF1R signaling. This included assessing, IL34, a second CSF1R ligand in addition the broadly-expressed CSF1, which has a more restricted expression pattern. In mouse tissues there have been reports of production by neurons, keratinocytes, as well as in kidney and testis, while in humans IL34 mRNA levels are highest in brain, spleen, and skin [93, 172]. IL34 deficient mice have a reduced number of microglia in the brain (20% decrease), which makes them more susceptible to neurotropic viruses [93]. The enriched expression in the brain therefore makes IL34 an interesting target to block signaling through this arm of the CSF1R pathway and investigate how this affects TAM phenotypes and glioma growth. Moreover, tissue-resident macrophages, such as microglia, and recruited monocytes can assume distinct roles [75, 171]. Previous studies from our lab and others have revealed the different ontogeny of microglia (MG) and monocyte-derived macrophages (MDMs) and how this may impact their differential roles in disease [29, 66, 75]. Nonetheless, although of distinct ontogeny, these two cell types display a certain degree of phenotypic plasticity and convergence, both in tumor development and in response to treatment [29, 75]. Therefore, we

reasoned that the IL34-deficient mouse model might be a useful tool to investigate the specific contribution of MG, since these mice are specifically depleted in these cells.

6.3.2 Results

All of the following experiments have been performed in two distinct PDGF-driven glioma (PDG) models, both based on the replication-competent ALV-splice acceptor (RCAS) retroviral system that allows the introduction of particular genetic alterations in a cell type-specific manner. DF1 chicken fibroblasts expressing either a RCAS-hPDFGB vector, or RCAS-hPDGFB and RCAS-Cre vectors together, have been intracranially injected in Nestin-Tva; Ink4a/Arf-/- mice (termed PDGFB Ink4a/Arf-/- glioma bearing mice or Ink4a/Arf-/- PDG model) or in Nestin-Tv-a; Pten flox/flox mice (termed PDGFB Pten-/- glioma bearing mice or Pten-/- PDG model), respectively.

Investigation of an anti-CSF1R antibody as a monotherapy and in combinatorial trials

Assessment of the 2G2 antibody as a single agent in preclinical trials

To explore the potential effects of the 2G2 antibody on tumor growth, we performed a 14 days trial with MRI measurements to evaluate the initial tumor volume and subsequent growth kinetics in the Ink4a/Arf-/- PDG model (Figure 1A). This model has been shown to respond very effectively to different CSF1R small-molecule inhibitors with maximum regression of tumor volume observed after 2 weeks of treatment [72, 73, 75]. In order to try and circumvent the heterogeneous and incomplete brain penetration of 2G2 (Figure 4A), glioma-bearing mice were treated either with a high loading dose (100 mg/kg) followed by weekly dosing (60 mg/kg), or with a standard weekly dose (30 mg/kg) (termed high dose schedule and standard dose schedule respectively). Mice in the 2G2-treated cohorts showed no therapeutic benefit compared to the control group, independent of the dosage assessed, with the tumors growing identically (Figure 1A). The potential effects of 2G2 monotherapy on TME composition were assessed by flow cytometry analysis at later endpoints (15 and 22 days after treatment initiation). We found that while the relative frequency of TAMs was significantly lower in the 2G2 group (Figure 1B), this did not impact the overall cellular density, depending on endpoint tumor volume and total cell count (Figure 1C). Subsequent analysis of TAM subpopulations showed a significant decrease of MG, while MDM numbers were not affected (Figure 1D). Based on these results we concluded that 2G2 monotherapy has no effects on tumor growth. TAM infiltration analysis suggests a potential impact on TAM numbers that may result from decreased MG cellular density.

Combination treatment of the 2G2 and irradiation and analysis of TAMs

The number of TAMs increases significantly in gliomas following irradiation [75], suggesting a potential benefit for combining IR and 2G2. Moreover, IR should improve blood-brain barrier (BBB) penetration, thus increasing antibody delivery to the tumor site [173]. In order to assess whether 2G2 treatment might be beneficial in the context of this combinatorial treatment, PDGFB-Ink4a/Arf-/- glioma-bearing mice were irradiated with a local single dose of 10 Gy followed by weekly 2G2 treatment using the high dose schedule (Figure 2A). Tumor regression, as measured by MRI, after IR was transiently less pronounced when combined with 2G2 (Figure 2B – compare left to right). However, this may simply reflect a reduction in the efficiency of clearing dead tumor cells post-IR in the 2G2 group, in the case where phagocytic capacity of macrophages is impaired at this time, which might be linked to the reduced TAMs observed in the 2G2 co-treatment group (Figure 2D). We did not observe any differences in the temporal kinetics of tumor rebound post-IR (Figure 2C).

In addition to changes in relative cellular frequencies, levels of the myeloid cell subpopulation-specific markers CD49d and CD11a were altered (Figure 2E) [66]. TAMs were reduced following 2G2 treatment in the context of combination with IR, which might be related to a better antibody penetration and/ or a significantly longer treatment duration than the monotherapy. However, even with these observed changes, 2G2 did not improve IR treatment outcome in these preclinical trials, in contrast to our findings with the small molecule BLZ945 [75].

Combination trials targeting CSF1R and VEGFA/ANG2

Anti-angiogenic therapies have been evaluated in the clinic for glioma patients, but did not have a major impact on overall survival [59, 60], although a number of countries approved this therapy for glioblastoma, including Switzerland [58], for its positive effects on life quality and edema control [51]. These clinical findings indicate the need for better understanding of the outcome of such treatments and evaluation of other therapeutic combinations that could improve their efficacy [59]. In a 1-week preclinical trial experiment, 2G2 treatment was combined with anti-angiogenic treatment; the A2V bispecific antibody from Roche targeting both VEGFA and Angiopoietin2 (Figure 3A). PDGFB-Ink4a/Arf-/- glioma-bearing mice were treated with the A2V antibody for 1.5 days before starting 2G2 administration, with the goal of achieving an initial vasculature stabilization that might then increase 2G2 antibody penetration [54]. However, neither A2V alone, nor A2V in combination with 2G2 resulted in a significantly decreased tumor growth (Figure 3B). It is important to note that mice in the control IgG cohort were purposely selected with a smaller initial tumor volume so that we could monitor them for 1 week (mice with larger tumors generally do not survive for 1 week without some therapeutic

intervention). Mice in the two treatment groups had larger initial tumors, so it is possible that there is a modest effect of A2V alone, although adding 2G2 does not lead to any obvious further differences in tumor volume. The number of TAMs was assessed by IF tissue staining using the macrophage marker, ionized calcium binding adaptor molecule 1 (Iba1), which showed a trend towards increased TAMs following A2V monotherapy, that was significantly decreased in mice co-treated with 2G2 (Figure 3C). These results, together with the analysis of the TME in the IR combinatorial trials, shows a significant decrease of TAMs when 2G2 treatment is added to either therapeutic intervention (Figures 2D and 3C). Nonetheless, 2G2 does not lead to a better outcome of antiangiogenic therapy in the preclinical setting.

Investigation of the biological mechanisms underlying the distinct consequences of CSF1R blockade, depending on the therapeutic agent utilized

2G2 monotherapy and combination with irradiation or antiangiogenic therapy did not show any survival benefit compared to the control groups. This is in contrast with previous publications that showed the use of different CSF1R small-molecule inhibitors in glioma models leading to tumor regression mediated by a phenotypic reprogramming of TAMs [72, 73, 75]. I therefore explored several potential possibilities that could explain the lack of evident 2G2 efficacy.

Analysis of 2G2 distribution in PDG glioma model

A large molecule such as the 2G2 antibody might not fully penetrate the BBB and thus only partially gain access to the tumor, even in high-grade lesions where the BBB can be transiently disrupted. Therefore, we used a fluorescently labelled Alexa647-2G2 antibody to assess *in vivo* distribution, and injected PDGFB-Pten-/- glioma-bearing mice with a 30 mg/kg dose and sacrificed 24h or 72h later. Labelled Alexa750-lectin was intravenously injected 5 minutes before sacrifice to visualize blood vessels in the tissue. Formalin-fixed whole brains were then processed for tissue clearing based on the 3DISCO technique [174]. We observed no Alexa647-2G2 signal in the normal brain, and some 2G2 retention in the tumor area 72 hours after injection (Figure 4A-B). However, we found that the antibody was heterogeneously distributed and penetration was dependent on vascular integrity and on tumor volume. On the other hand, the total amount of antibody in the tumor did not increase over time (Figure 4C). We therefore concluded that while heterogeneous, 2G2 delivery can be partially achieved in the brain.

Assessment of a brain-specific version of 2G2 (2G2 brain-shuttle)

Several approaches have been investigated in order to improve antibody penetration in the brain, including engineering of antibodies with precise motifs which bind to the transferrin

receptor on endothelial cells in the BBB thereby favoring their transcytosis [175]. Although my previous data showed that some 2G2 delivery into the tumor can be achieved, this was very heterogeneous. We therefore treated PDGFB-Ink4a/Arf-/- glioma-bearing mice with a 2G2 antibody linked to a molecular element binding to the transferrin receptor (termed the 2G2 brain-shuttle) using a high dose regimen, to potentially increase antibody penetration. Nonetheless, tumors continued to grow similarly to controls (Figure 4D). While we assume that this modified version of 2G2 should have improved brain penetration and accumulation within the tumor, we would need to perform further analysis to confirm this point.

Assessment of Fc-dead version of 2G2

We next investigated whether 2G2 might trigger a different biological response than the previously used small-molecule CSF1R inhibitors. The Fc-portion of an antibody can regulate the biological response to its binding, which includes, among others, antibody-dependent cellular cytotoxicity (ADCC) [176]. ADCC can be mediated by different cellular players, including macrophage binding to antibody-coated cells through the Fc-receptor, and consequently phagocytosing them. We therefore assessed whether treatment with a Fc-dead version of 2G2 could permit an uncoupling of the biological response mediated by the Fc part (potentially ADCC of 2G2-bound TAMs, which could explain the reduced frequencies of TAMs we observed in the combinatorial trials) and the actual consequence of CSF1R signaling inhibition (which might then resemble the effect of previously used small-molecule inhibitors) [72, 73, 75]. We treated PDGFB-Ink4a/Arf-/- glioma-bearing mice with Fc-dead 2G2 at a high dose schedule, but tumor growth kinetics were similar as previously observed, indicating no contribution of the Fc-portion of 2G2 on therapy outcome (Figure 4E), as previously reported for other cancer models [177].

Combine 2G2 treatment with a CSF1R small molecule inhibitor to assess reprogramming potency (with the small molecule inhibitor) in the context of partially reduced TAM frequencies (2G2 pre-treatment)

Given the differences between using small-molecule inhibitors of CSF1R, and my results to date with the 2G2 antibody, we also attempted to investigate whether there may be off-target effects of these compounds. While multiple previous studies investigating BLZ945 and PLX3397 had not led to any results in support of this notion, we nonetheless wanted to investigate this point in the context of 2G2 treatment. Therefore, we attempted to first deplete TAMs- the target population for CSF1R inhibitors in these models, and then ask whether there was still an effect of the small molecule. We used a commercially available CSF1R inhibitor (BLZ945, Selleck Chemicals) following 2G2 pre-treatment (Figure 5A), expecting one of two following outcomes.

In the first scenario, we might observe a decreased efficacy of the small-molecule inhibitor due to the prior reduction of TAMs with 2G2 (in a pre-treatment schedule), which are thus not present in a sufficient number to fully exert their antitumorigenic functions after being re-programmed by the small molecule. In the second scenario, we might observe a similar efficacy of the small molecule inhibitor after 2G2 pre-treatment. This would suggest that the tumor regression previously observed may be caused by off-target effects of the distinct small molecule inhibitors. However, as already mentioned, this second scenario might be really difficult to fully prove, since we now know that 2G2 monotherapy does not substantially impact TAM numbers. PDGFB-Ink4a/Arf-/- glioma-bearing mice were treated with 2G2 or IgG control for 10 or 17 days before starting BLZ945 treatment. We found that 2G2 pre-treatment did not impact BLZ945 efficacy, although the treatment group with a 17d 2G2 pre-treatment shows indications of a slightly slower regression than the control group (Figure 5D-E). In sum, using this rationale, we cannot currently conclude whether BLZ945 (or PLX3397) have any CSF1R off-target effects as the current experimental tools do not permit us to completely deplete TAMs in preclinical glioma models.

Investigate the contribution of IL34 in glioma

We currently conclude that key differences in the 2G2 mode of action, potency and binding site might explain its lack of efficacy. This, in combination with its incomplete and heterogeneous penetration in gliomas in the brain, might lead to the different therapeutic outcome compared to small-molecule CSF1R inhibitors. This might also indicate that CSF1R pathway inhibition can be finely tuned and lead to different phenotypic responses, ranging from macrophage killing to phenotypic reprogramming, and consequently significantly impact therapy outcome [76]. We therefore hypothesized that removing the brain-enriched CSF1R ligand IL34 might result in a partial inhibition of CSF1R signaling, thereby affecting the phenotypes of TAMs.

To test this hypothesis, we used IL34 KO mice [93]. We first validated the published phenotype of these mice by confirming the reduction of whole brain MG by 70% (Figure 6A-B), particularly in the brain anatomical regions where our experimental gliomas normally grow (cortex and corpus callosum) (Figure 6C). Of note, we observed a larger difference in MG content compared to the original publication [93], which is likely related to the additional use of Ly-6C, Ly-6G, CD49d and CD11a markers to more precisely define the MG population, instead of CD45 and CD11b alone, as previously described. We next injected IL34 KO mice and WT littermates orthotopically with a PDG-derived cell line but did not observe any evident

difference in tumor development. We also bred the IL34 KO line with the Ink4a/Arf-/- PDG model and monitored survival, but no differences were found between IL34 deficient mice and the control group (Figure 6D). The TME composition was also not altered in a subset of tumors that were analyzed by flow cytometry (Figure 6E, 6F and 6G). Together, our data indicate no apparent role of IL34 on glioma growth and TME composition.

6.3.3 Discussion

CSF1R targeting has shown promising efficacy in murine glioma models and it is being currently evaluated in multiple clinical trials [72, 73, 75, 90, 96]. In previous studies, BBB-permeable small-molecule inhibitors have been successfully tested not only as monotherapy, but also in combinatorial trials that further augmented the anti-tumor effect [73, 75, 90]. The anti-CSF1R antibody we assessed in this study did not lead to any favorable outcomes regarding tumor growth or animal survival. Of note, the larger molecular size of 2G2 could be the main underlying reason of such lack of efficacy, as shown by the heterogenous and incomplete distribution of the fluorescently labelled antibody inside the tumor. Indeed, 2G2 treatment led to TAM depletion in a various spectrum of extracranial tumor models [88, 178-182]. In our glioma model we observed a shift in the proportion of the different myeloid subpopulations upon treatment with 2G2 as single agent, but not a significant complete depletion. Thus, in the context of glioma, CSF1R inhibition with 2G2 could be differentially regulated by the specificities of the TME. Also, we only observed a trend in reduced TAM content in the therapeutic combinations with A2V or IR treatment, and did not observe any beneficial effects in these trials. Moreover, our experimental attempts to understand the detailed mechanism of 2G2 mode of action did not lead to conclusive results, including the investigation of glioma growth and TME composition in the context of IL34 deficiency, as a strategy to modulate CSF1R signaling. In sum, 2G2 treatment did not demonstrate any efficacy in our glioma model, either as a monotherapy, or in combinatorial trials. We hypothesize that the limited 2G2 penetration and distribution in the tumor bed are major hurdles for such a therapeutic approach, and this will be an important aspect to analyze in detail in any future project assessing an antibody-based therapy in these preclinical models.

6.3.4 Materials and Methods

Animals, cells and tumor models

Animals

The Nestin-Tv-a;*Ink4a/Arf*$^{-/-}$ and Nestin-Tv-a; Pten flox/flox mouse lines have been previously described [73, 152] and were generously provided by Dr. Eric Holland, USA. IL34$^{LacZ/LacZ}$ KO mouse line (C57BL/6J background) has been previously described [93] and was generously provided by Dr. Marco Colonna and Dr. Adriano Aguzzi. Nestin-Tv-a;*Ink4a/Arf*$^{-/-}$ mice and IL34 KO mice were bred to generate the IL34 KO Nestin-Tv-a;*Ink4a/Arf*$^{-/-}$ mouse line. All mice were bred within the University of Lausanne animal facilities, and all animal studies were approved by the Institutional Animal Care and Use Committees of the University of Lausanne and Canton Vaud, Switzerland.

Cells

For glioma induction, DF1 chicken fibroblasts were obtained from ATCC. RCAS vectors expressing PDGFB-HA or Cre recombinase were kindly provided by Dr. Tatsuya Ozawa and Dr. Eric Holland [37, 153]. Cells were cultured in DMEM (Life Technologies) supplemented with 10% fetal bovine serum (Life Technologies) under standard conditions.

Glioma model

4.5 to 7 weeks old mice were intracranially injected as previously described [66, 72, 73, 155]. Briefly, mice were fully anesthetized using isoflurane inhalation anesthesia (2% isoflurane/O_2 mixture), and a mixture of 2% lidocaïne (Streuli Pharma) and 0.5% bupivacaine (Carbostesin; Aspen Pharma Schweiz) was applied as a local anesthetic (50 µl per mouse), and 0.3 mg/ml buprenorphine (Temgesic; Indivior Schweiz) was given subcutaneously as a systemic anesthetic (100 µl per mouse). Using a stereotactic apparatus, cells were injected into the right frontal cortex (2 mm frontal, 1.5 mm lateral from bregma, 2 mm deep). Nestin-Tv-a;*Ink4a/Arf*$^{-/-}$ mice were injected with 2 x 10^5 RCAS-PDGFB-HA DF1 cells, while Nestin-Tv-a; Pten flox/flox mice were injected with 3 x 10^5 DF1 cells (a 1:1 mixture of RCAS-PDGFB-HA/ RCAS-Cre DF1 cells). The skin incision was sealed with Vetbond tissue adhesive (3M), and the mouse was placed on a heating pad and monitored until recovery from anesthesia. Finally, Bepanthen cream (Bayer) was applied on the incision site before placing the animal back in the cage.

Treatments

Therapeutic antibodies

All therapeutic antibodies were administered by intraperitoneal injection. The detailed information about the clone is listed in table 1. A high loading dose of 100 mg/kg, followed by weekly doses of 60 mg/kg, was defined as “high dose” 2G2 schedule; while a weekly 30 mg/kg regimen was defined as “standard dose” 2G2 schedule. 2G2 brain-shuttle version, FC-dead 2G2 and IgG control antibody were administered with the “high dose” schedule. Fluorescently labelled 2G2-Alexa647 antibody was administered once at 30 mg/kg. A2V antibody and IgG control antibody were administered at 20 mg/kg weekly.

Irradiation

Each tumor-bearing mouse was fully anaesthetized using isoflurane inhalation anesthesia (2% isoflurane/O_2 mixture). Irradiation of the head was performed with a X-RAD SmART instrument (Precision X-Ray) equipped with 1x1 cm collimator to contain irradiation in the tumor area only. First, a live-imaging CT scan of the head was performed to place the collimator in the correct position to irradiate the brain (cerebellum and the upper respiratory tract were left outside the field of view). A beam of 5 Gy was dosed laterally of the animal, from the right side and the left side respectively, for a total of 10 Gy.

BLZ945 treatment

BLZ945 powder (Selleck) was dissolved in 20% Captisol (w/v) (Ligand Pharmaceuticals) in H_2O. The pH was lowered to pH 2.2 with 37% HCl (Sigma-Aldrich) to allow the powder to fully dissolve. The solution was stirred overnight to obtain a clear solution. Dissolved BLZ945 was administered daily at 200 mg/kg by oral gavage.

Tissue analysis

Flow cytometry

Mice were sacrificed by terminal anesthesia using pentobarbital (CHUV, Lausanne, Switzerland), followed by transcardial perfusion with PBS. When possible, the tissue was kept in the dark to preserve the fluorophores. The brain tumor was macro-dissected and dissociated using the Brain Tumor Dissociation Kit (Miltenyi). The dissociated tissue was filtered through a 40 µm mesh filter and then underwent myelin removal using the Myelin Removal Beads Kit (Miltenyi). The resulting myelin-free single cell suspension underwent red blood cell lysis for 10 minutes on ice using 10x red blood cell lysis buffer (Biolegend). The single cell suspension was stained with the Zombie-near-infrared fixable viability kit

(Biolegend) for 20 minutes at room temperature (RT), washed with FACS buffer (2 mM EDTA (Life Technologies) and 0.5% BSA (Jackson ImmunoResearch) in PBS (Bichsel) and then FC-blocked (BD Biosciences) for 30 minutes on ice. After washing with FACS buffer, cells were incubated with directly-conjugated antibodies (table 1). Stained samples were washed 3 times with FACS buffer. For MRC1-intracellular staining, cells were fixed with Permeabilization/Fixation solution (Invitrogen) overnight at 4°C, and then incubated with antibody dilution mix in Permeabilization buffer (Invitrogen) for 30' at RT. Last, stained samples were washed 3 times with Permeabilization buffer. Samples acquisition was performed on a BD Fortessa at the Flow Cytometry Core Facility of University of Lausanne. FlowJo v10.7.1 (BD) was used for analysis.

Tissue sections immunofluorescence staining and imaging

10 µm tissue sections were thawed for 10', and circles were drawn around the tissue with a PAP pen (Daido Sangyo). After 5' wash with 1X PBS (Bichsel), the slides were permeabilized with 0.1% Triton X-100 (AppliChem) diluted in 1X PBS for 10' at room temperature (RT). Slides were then washed 3x5' with 1X PBS and then incubated with filtered blocking buffer for 1 hour at RT (1X PBS, 0.2% bovine serum albumin (Jackson ImmunoResearch), 10% donkey normal serum (EMD Millipore), 10% goat normal serum (Merck) – when using goat primary antibodies, BSA and goat serum were omitted from the blocking buffer mix). Sections were then incubated with the 250 µL/section primary antibodies mix (table X) in dilution buffer (1:1 mix of 1X PBS and blocking buffer) at 4°C overnight. The day after, slides were washed 3x10' with 1X PBS and then incubated with the secondary antibody mix (table X) in dilution buffer including 1:5000 DAPI (Life Technologies) for 1h at RT. Slides were eventually washed 3x10' with 1X PBS and mounted with a coverslip (Menzel-Gläser) and Dako mounting medium (Agilent). Stained tissue sections were imaged with an Axio Scan.Z1 slide scanner (Zeiss) equipped with a Colibri 7 LED light source (Zeiss) using a Plan-Apochromat 20x/0.8 DIC M27 coverslip-corrected objective (Zeiss). All slides from the same staining panel were digitalized using the same acquisition settings. All washes were performed in a slide bucket, while all incubation steps in a humified chamber. One section was stained with primary antibodies, while the adjacent section was stained with secondary antibodies only to assess unspecific antibody binding and signal.

Brain clearing

Glioma-bearing mice were injected intraperitoneally with 30 mg/kg 2G2-Alexa647 (Roche). 24h later, 100 µg of lectin-Alexa750 (Roche) were injected intravenously and allowed to circulate for 5 minutes. Mice were then sacrificed by terminal anesthesia using pentobarbital (CHUV, Lausanne, Switzerland), followed by transcardial perfusion with PBS and 4% PFA

(Electron Microscopy Sciences). Harvested brains were fixed for 24h in 4% PFA on a shaker. Fixed brains were then dehydrated in a tetrahydrofuran (Sigma-Aldrich) dilution series: 70% for 90', 80% for 90', 90% for 90', 100% for 90', 100% overnight, 100% for 60'. The container lid was firmly sealed with Parafilm (Bemis) to avoid contact with air and humidity. Afterwards, samples were directly put into 100% dibenzyl-ether (Sigma-Aldrich) for 3 to 5 days at 4°C on a shaker. Cleared tissues were then imaged with a light-sheet microscope.

Non-quantitative MRI monitoring

Monitoring of tumor growth for non-quantitative MR imaging was performed using a 1 Tesla Small Animal MR Scanner (Bruker BioSpec). The mouse was fully anaesthetized with 1-2% isoflurane/oxygen inhalation and placed on the imaging bed, while monitoring respiratory rate and temperature. Data acquisition was performed using the ParaVision software (Bruker). A 3-slice localizer was performed to assess the mouse head position. For glioma-bearing mice, 2D T_2-weighted acquisition was performed (turbo rapid acquisition relaxation enhancement (Turbo-RARE), repetition time (TR) 2500 ms, echo time (TE) 85 ms, number of averages (NA) 18, number of slices 10, slice thickness (ST) 0.6 mm, FOV 20 x 20 mm, pixel size 156 x 156 µm, echo train length (ETL) 12, acquisition time (AT) 3 min) with images being acquired in axial planes. After imaging, the mouse was returned to the cage and monitored until it regained consciousness. Volumetric analysis of the gliomas was performed on MR image DICOM files using the MIPAV software (National Institutes of Health, USA).

Data analysis

Statistics

Prism v.9 (GraphPad) and R version 4.1.0 were used to plot all data and perform statistical analysis (ggplot package). Parametric data were analyzed by a two-tailed Student's t-test (paired or unpaired depending on the experimental setup). Non-parametric data were analyzed by a Mann-Whitney test on ranks (paired or unpaired depending on the experimental setup). $P<0.05$ was considered as statistically significant. Each specific test is reported for each experiment in the figure legends. Boxplots are used to present the data, showing median and the 25^{th} to 75^{th} percentiles.

Table 1: Antibodies used in the study

Antibodies							
Target	**Species**	**Antibody**	**Manufacturer**	**Clone**	**Category number**	**Dilution**	**Application**
CSF1R	mouse-hamster chimeric	Anti-mouse CSF1R	Roche	2G2	-	-	In vivo
VEGFA/Ang2	murinized	Anti-mouse VEGFA/Ang3 bispecific	Roche	A2V	-	-	In vivo
CSF1R	mouse-human chimeric	Anti-mouse CSF1R Fc dead version	Roche	2G2	CSF1R-0039	-	In vivo
CSF1R	mouse-human chimeric	Anti-mouse CSF1R brain shuttle version	Roche	2G2	CSF1R-0040	-	In vivo
IgG1	mouse-hamster chimeric	Anti-mouse IgG1	Roche	MOPC21	-	-	In vivo
CSF1R	mouse-hamster chimeric	Anti-mouse CSF1R Alexa Fluor 647	Roche	2G2	-	-	In vivo
Iba1	Rabbit	Anti-mouse Iba1	Wako	Polyclonal		1:1000	Immunofluorescence panel #1
Ly-6C	Rat	Anti-mouse Ly-6C Brilliant Violet 711	BioLegend	HK1.4	128037	1:800	Flow cytometry panel #1
Ly-6G	Rat	Anti-mouse Ly-6G Brilliant Violet 605	BioLegend	1A8	127639	1:160	Flow cytometry panel #1
CD11b	Rat	Anti-mouse CD11b BUV661	BD Biosciences	M1/70	612977	1:800	Flow cytometry panel #1, Flow cytometry panel #2
CD49d	Rat	Anti-mouse CD49d PE/Cy7	BioLegend	R1-2	103618	1:160	Flow cytometry panel #1
CD45	Rat	Anti-mouse CD45 Alexa Fluor 700	BioLegend	30-F11	103128	1:200	Flow cytometry panel #1, Flow cytometry panel #2
CD3	Hamster	Anti-mouse CD3e BUV395	BD Biosciences	145-2C11	563565	1:75	Flow cytometry panel #1 and #2
NK-1.1	Mouse	Anti-mouse NK-1.1 Brilliant Violet 421	BioLegend	PK136	108741	1:640	Flow cytometry panel #1
CD19	Rat	Anti-mouse CD19 Brilliant Violet 605	BioLegend	6D5	115539	1:320	Flow cytometry panel #2
NK-1.1	Mouse	Anti-mouse NK-1.1 Brilliant Violet 711	BioLegend	PK136	108745	1:640	Flow cytometry panel #2
MRC1	Rat	Anti-mouse MRC1 APC	BioLegend	C068C2	141708	1:200	Flow cytometry panel #1

6.3.5 Figures

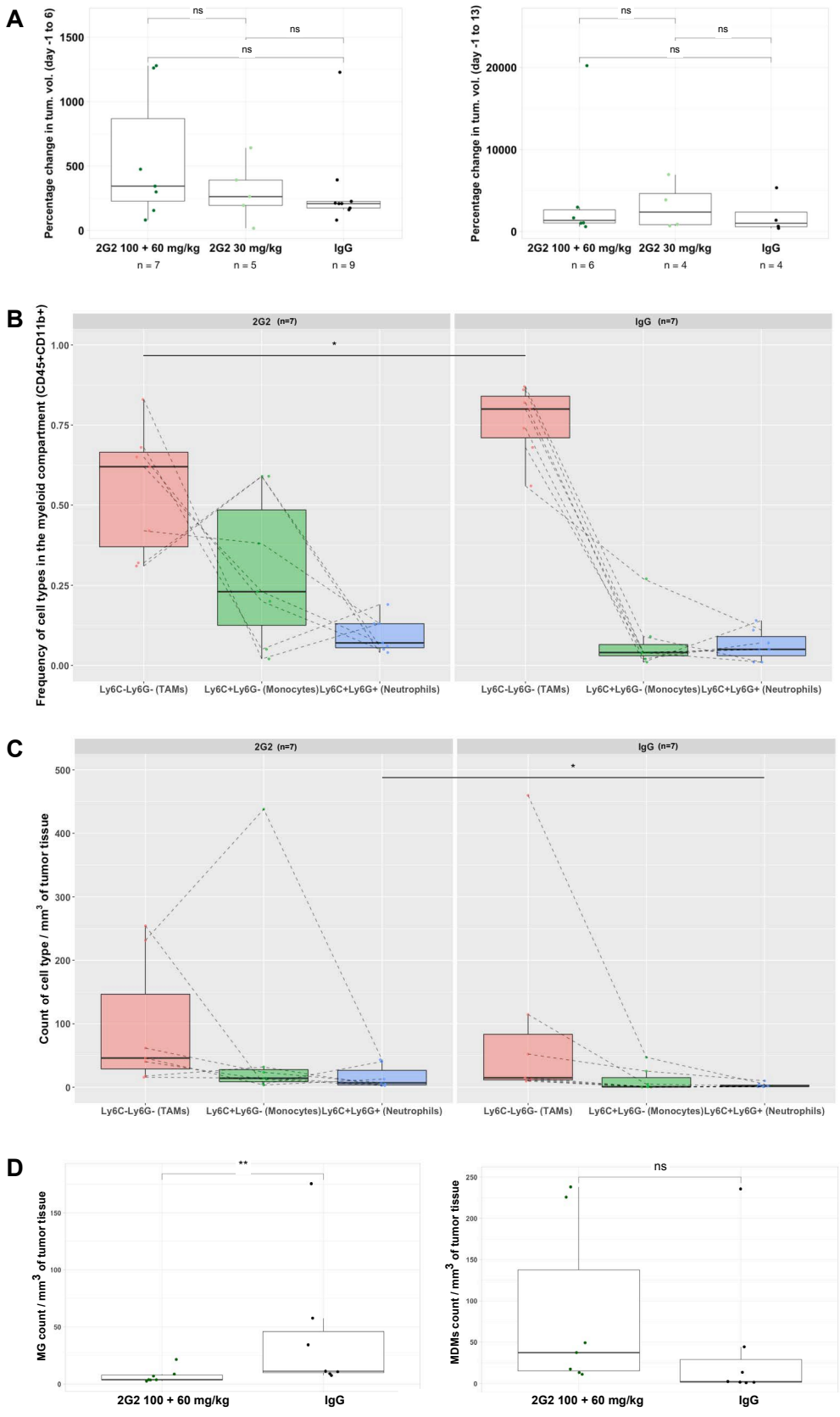
A
Percentage change in tum. vol. (day -1 to 6)
ns
ns
ns
2G2 100 + 60 mg/kg
2G2 30 mg/kg
IgG
n = 7
n = 5
n = 9
Percentage change in tum. vol. (day -1 to 13)
n = 6
n = 4
n = 4
B
2G2 (n=7)
IgG (n=7)
Frequency of cell types in the myeloid compartment (CD45+CD11b+)
Ly6C-Ly6G- (TAMs)
Ly6C+Ly6G- (Monocytes)
Ly6C+Ly6G+ (Neutrophils)
C
Count of cell type / mm3 of tumor tissue
D
MG count / mm3 of tumor tissue
MDMs count / mm3 of tumor tissue

Figure 1. 2G2 monotherapy does not affect glioma growth and partially alters the myeloid cell composition in the TME. (**A**) Changes in tumor volume of the different treatment groups in Ink4a/Arf$^{-/-}$ PDGF-driven glioma (PDG)-bearing mice in the first week of treatment (left) and over the full time course of the trial (2 weeks, right – to note, not all mice survived until this endpoint). Mice received a loading dose of 100 mg/kg 2G2, followed by one or two 60 mg/kg doses (1-week and 2-week time points respectively, the last dose was administered the day before endpoint). The standard treatment group lasted 2 weeks (30 mg/kg dose/week, for a total of three doses including the final dose the day before endpoint). The IgG control group was treated with the high dose schedule. (**B**) Flow cytometry analysis of the myeloid cell compartment in the tumor of 2G2- or IgG-treated mice. Population frequencies of TAMs (CD45+CD11b+Ly6C-Ly6G-), monocytes (CD45+CD11b+Ly6C+Ly6G-) and neutrophils (CD45+CD11b+Ly6C+Ly6G+) indicate a reduced frequency of TAMs in 2G2-treated mice. (**C**) Cellular density of TAMs, monocytes and neutrophils, which was calculated by assessing the absolute cell number by flow cytometry with counting beads, and normalizing the count to the endpoint tumor volume. (**D**) Cellular density of TAMs subpopulations. MG (left, CD49d-CD11a- TAMs) cellular density was decreased upon 2G2 treatment, while MDMs (right, CD49d+CD11a+ TAMs) were not affected by 2G2 therapy. In all graphs, the Mann-Whitney statistical test was used to assess significance; * $p<0.05$, ** $p<0.01$, ns or if not stated: non-significant.

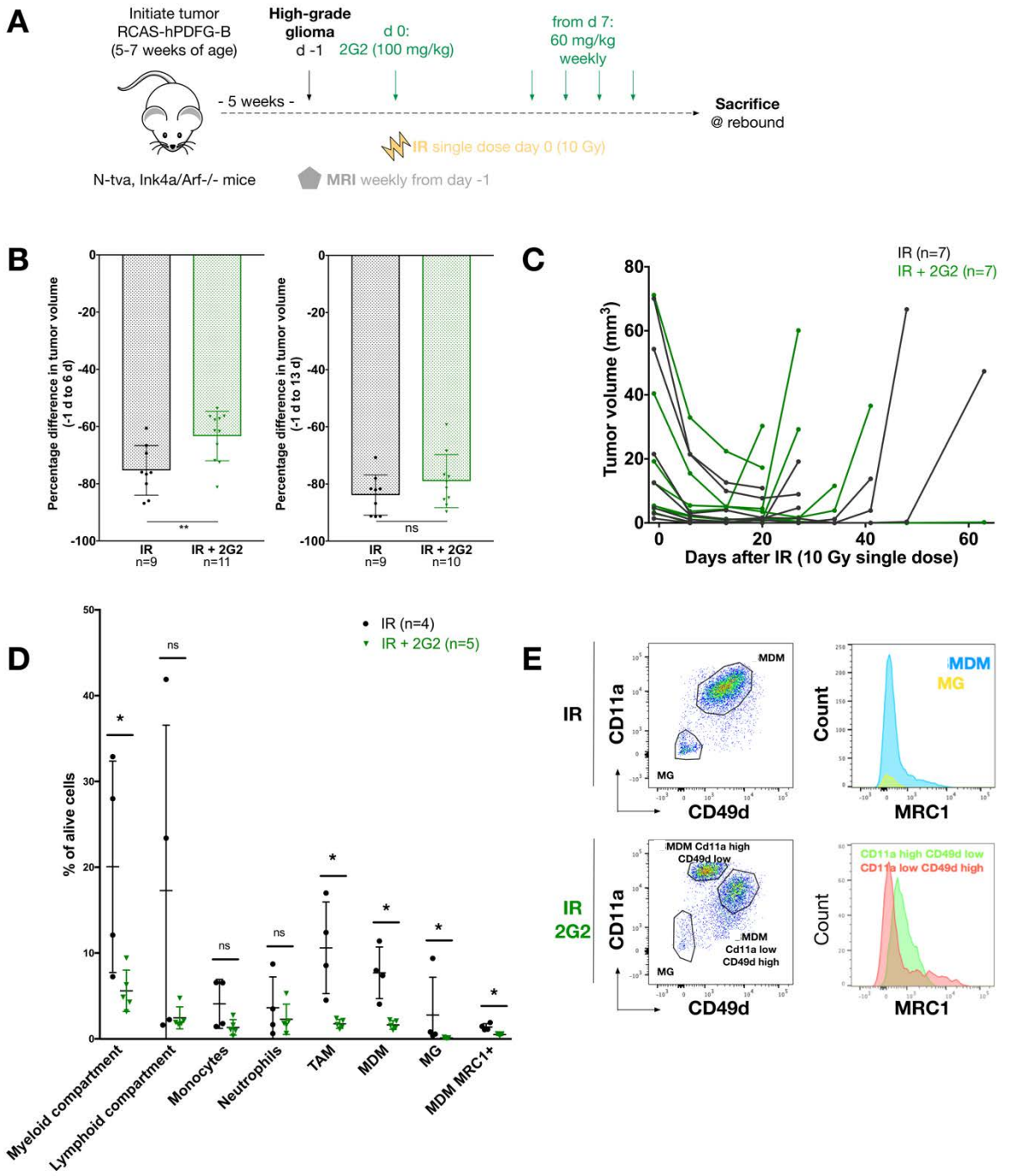

Figure 2. 2G2 combination treatment does not impact the response to IR. (**A**) Experimental design to assess therapeutic effect of irradiation (IR) alone and in combination with 2G2 in the PDG mouse glioma models. In these trials, no isotype control for the 2G2 antibody was injected (as it was not provided in sufficient quantities by Roche). (**B**) Percentage change in tumor volume after 7 or 14 days of treatment in Ink4a/Arf$^{-/-}$ PDG mice. (**C**) Tumor growth post-IR until endpoint (determined as tumor rebound). (**D**) FACS analysis of the myeloid cell compartment. TAM count is decreased in the presence of 2G2. (**E**) Analysis of microglia (MG) and monocyte-derived macrophage (MDM) sub-populations shows changes

in population-specific markers depending on treatment, together with differential expression of MRC1. Mann-Whitney statistical test was used to assess significance; * $p<0.05$, ** $p<0.01$, ns or if not stated: non-significant.

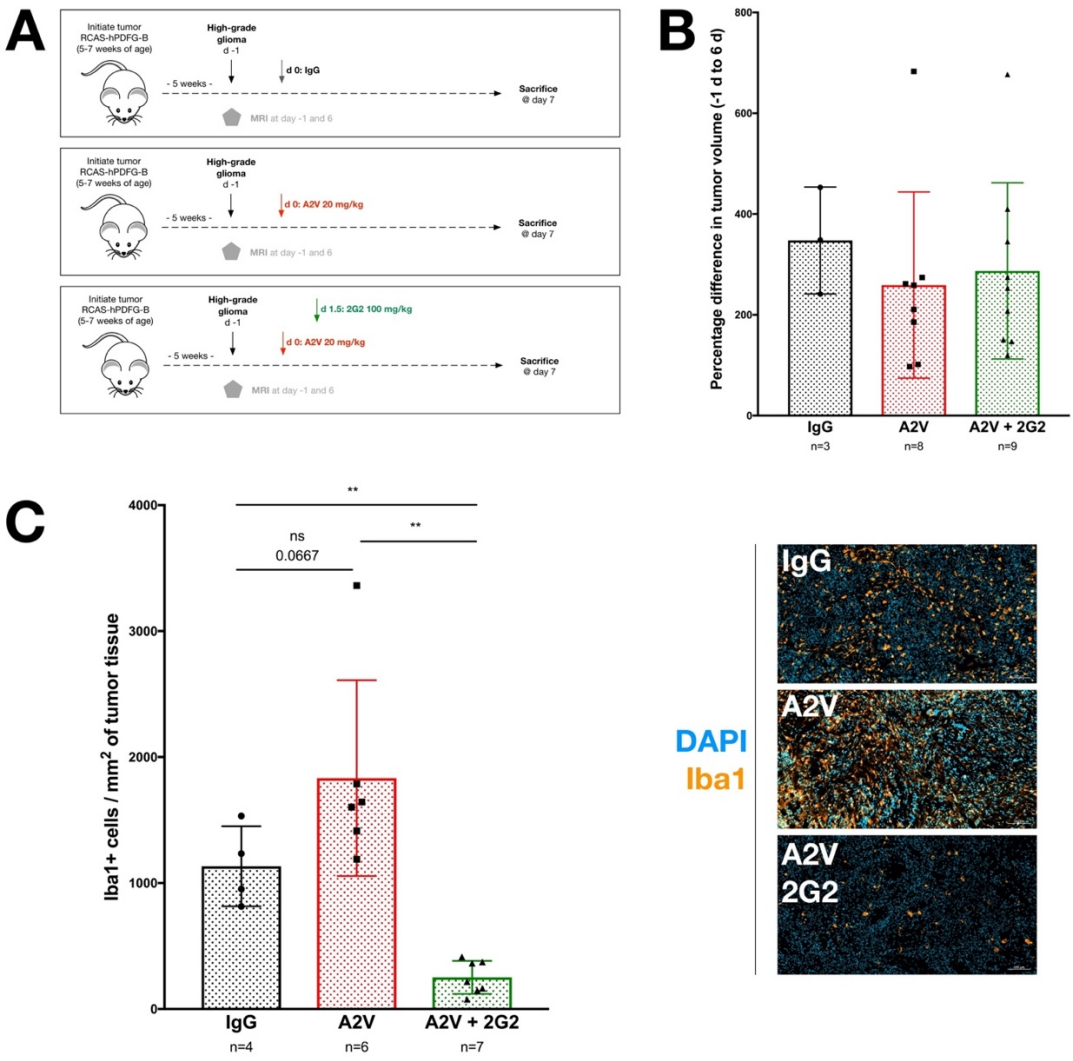

Figure 3. Therapeutic combination of 2G2 and A2V does not affect tumor growth but reduces the number of TAMs in gliomas. (**A**) Experimental design to assess the therapeutic effect of the A2V antibody alone, and in combination with 2G2, in the PDGF-driven glioma (PDG) mouse models. In these trials, for the 2G2 antibody no isotype control was injected (as this was not provided in sufficient quantities by Roche). (**B**) Percentage change in tumor volume after 7 days of treatment in Ink4a/Arf$^{-/-}$ PDG mice. (**C**) Quantification of tumor-associated microglia and macrophages (Iba1+). Representative images are shown on the right. All mice were treated for 1 week, apart from 3 mice in the A2V cohort and 1 mouse in the A2V + 2G2 cohort that were treated for 2 weeks in total (no obvious changes in the Iba1+ cell content for these mice were noted, apart from the A2V + 2G2 2-week treated mouse that had the lowest number of Iba1+ cells). Mann-Whitney statistical test was used to assess significance; ** $p<0.01$, ns or when not stated: non-significant.

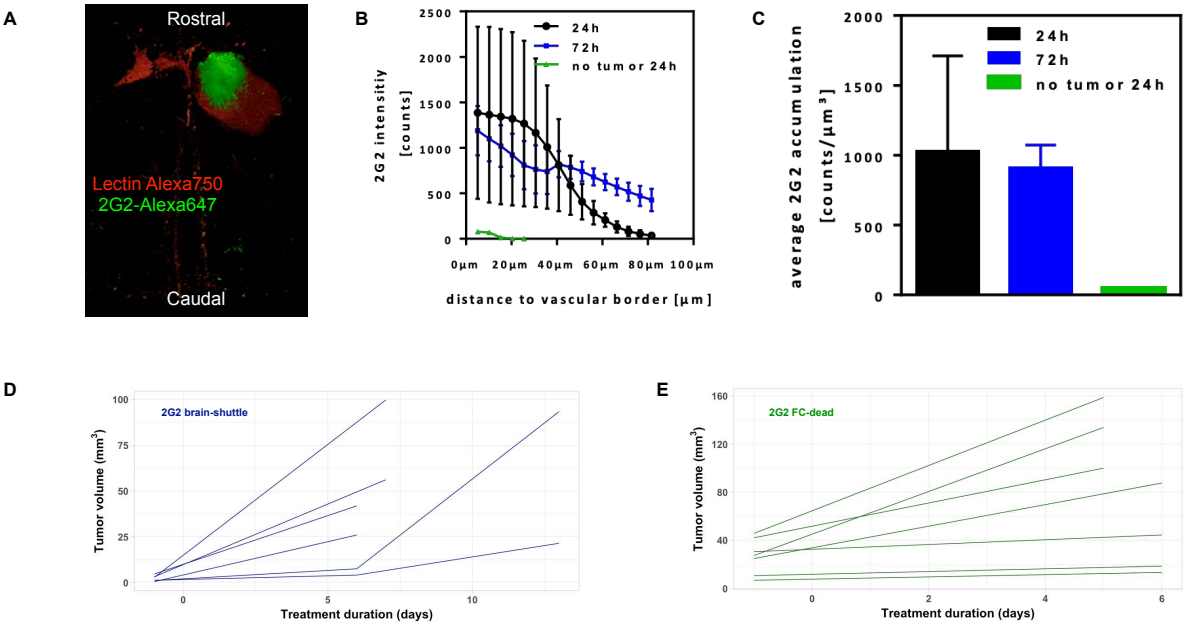

Figure 4. 2G2 partially penetrates into the tumor bed and distributes heterogeneously. (**A**) Representative 3D-light sheet microscopy image of whole brain samples from preliminary dosage optimization in the PDGFB Pten$^{-/-}$ model (30 mg/kg 2G2, 72 hours). (**B**) 2G2-Alexa647 penetration and accumulation (**C**) in the PDGF-B Pten$^{-/-}$ model. (**D**) Tumor growth curves in Ink4a/Arf$^{-/-}$ PDGF-driven glioma (PDG)-bearing mice treated with 2G2 brain-shuttle version or (**E**) FC-dead 2G2 with a high dose schedule (100 mg/kg loading dose followed by 60 mg/kg weekly).

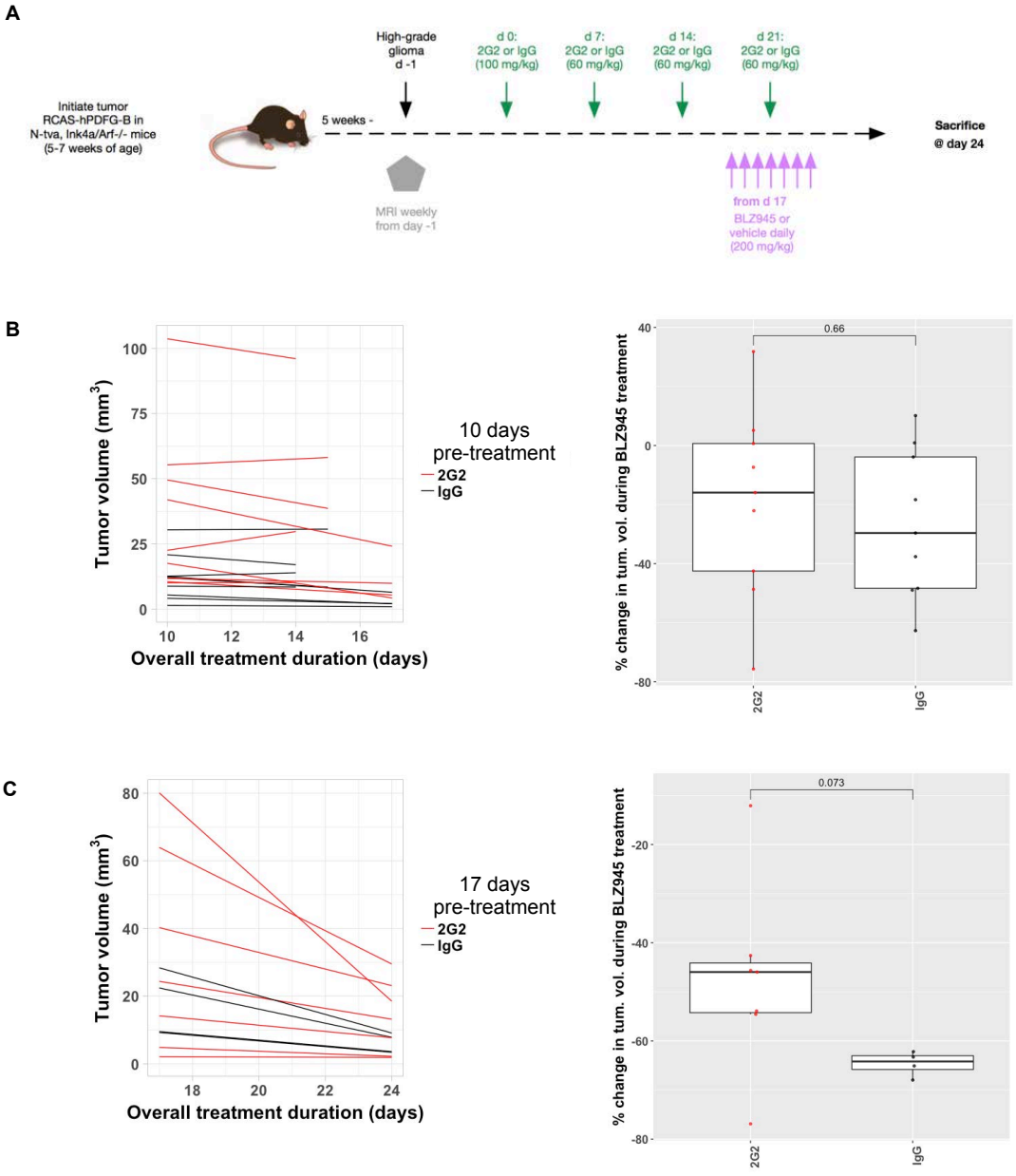

Figure 5. The anti-glioma efficacy of BLZ945 is not impacted by 2G2 pre-treatment. (**A**) Experimental design to assess the therapeutic effect of a commercial small-molecule CSF-1R inhibitor (BLZ945) following 2G2 pre-treatment in the PDGF-driven glioma (PDG) mouse models. Due to different tumor growth kinetics, mice were divided into two groups of either 10 or 17 days of 2G2 pre-treatment. (**B**) Tumor growth response to BLZ945 treatment in the 10 days 2G2 pre-treatment and IgG control (left) and percentage change of tumor volume in the same time frame (right). (**C**) Tumor growth response to BLZ945 treatment in the 17 days 2G2 pre-treatment and IgG control (left) and percentage change of tumor volume in the same time

frame (right). Mann-Whitney statistical test was used to assess significance in all comparisons; ** $p<0.01$, ns or when not stated: non-significant.

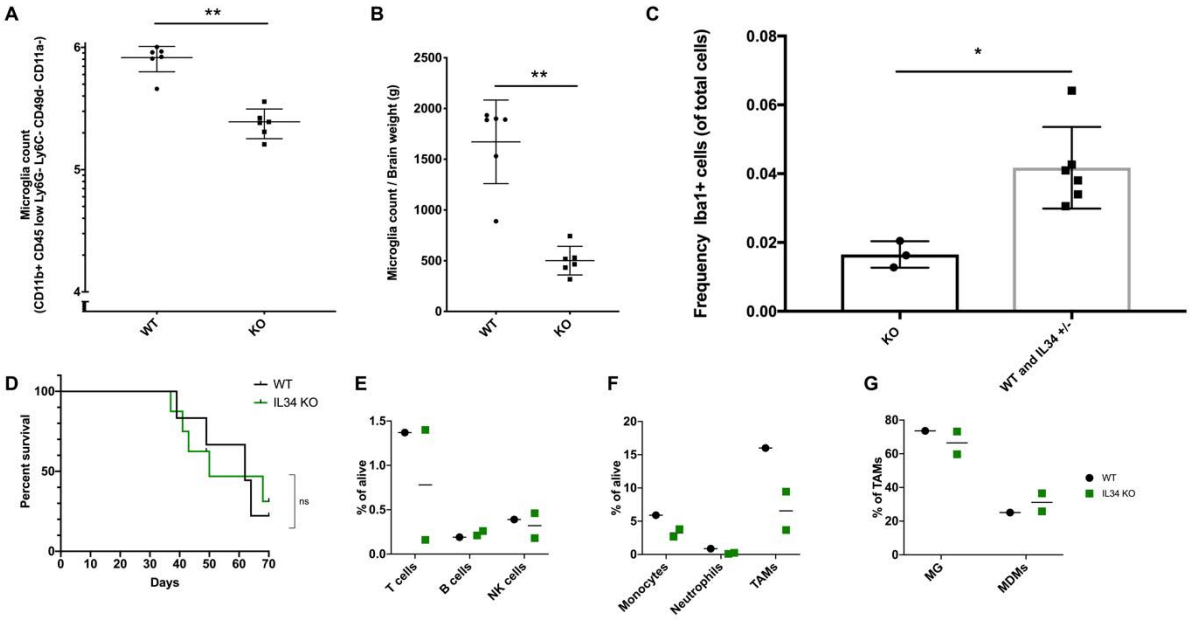

Figure 6. Glioma growth in IL34 KO mice is not affected despite the reduction in MG content in healthy brains. (**A**) Total microglial cell number (CD45+CD11b+Ly6C-Ly6G-CD49d-CD11a-) in the brains of IL34 KO or WT littermates (male mice, 5 to 7 weeks of age) and normalized to brain weight (**B**), showing MG reduction in mice lacking IL34. (**C**) Quantification of microglia (Iba1+) in cortex and corpus callosum. Mann-Whitney statistical test was used to assess significance in all comparisons; ** $p<0.01$, ns or when not stated: non-significant. (**D**) Survival curves of IL34 WT or IL34 KO PDGFB Ink4a/Arf-/- glioma bearing mice. TME composition analysis by flow cytometry of (**E**) lymphoid immune cells, (**F**) myeloid cells and (**G**) TAM subpopulations in a subset of IL34 WT or IL34 KO PDGFB Ink4a/Arf-/- gliomas.

7. Discussion

During my PhD thesis, I investigated in detail the glioma TME, with a major focus on TAMs, the most abundant immune cell population in this tumor type, which has been shown to be an attractive and effective therapeutic target in multiple preclinical glioma models [72, 73, 75, 90]. My goal was to gain new biological insights and ultimately contribute to a deeper understanding of the disease and to the development of novel treatments. While assessing the effectiveness of the therapeutic targeting of TAMs and other TME components, such as anti-angiogenic drugs and radiotherapy, I developed different imaging techniques to better monitor tumor progression and the response to such treatments. The implementation of ^{19}F MRI and an IVM-MRI imaging pipeline revealed new insights into the spatial and temporal characteristics of the TME. Such imaging approaches will help in the planning of future translational projects, by allowing us to delineate the complexity and temporal nature of TME cell dynamics. This will be essential to design and investigate new treatments, by carefully examining which cell type to target and the optimal timing of such interventions. Critically, I focused on techniques that enabled an extensive longitudinal monitoring of brain tumors *in vivo*, a powerful new advance for the field, in order to observe the different cell types in their native environment in the same animals over time. Moreover, a key aspect was the investigation of both preclinical imaging methods and translationally-relevant approaches that could ultimately be implemented in the clinic.

7.1 ^{19}F MR imaging of TAMs

The clinical management of glioma patients relies heavily upon MRI. For example, the MRI-contrast agent gadolinium can be injected intravenously and used to highlight specific tumor regions as it leaks out of areas where the BBB is impaired, thereby enabling a quantitative measurement of vascular functionality and permeability [136, 137]. In childhood and adult brain tumors the response to anti-angiogenic treatment was accurately predicted by this type of MRI [134, 135]. However, the vasculature is just one component of the immensely complex brain TME [10], and standardized and robust MRI-based biomarkers allowing the visualization of other key TME elements have not yet been extensively developed [120]. TAM abundance and diverse phenotypes influence the establishment of an immunosuppressive TME in gliomas [33, 34, 77], potentially blocking the effectiveness of novel immunotherapies in patients [50]. Despite their pivotal role in glioma biology, currently, the content of TAMs can

only be assessed on tissue biopsies obtained from the surgical removal of the tumor, and analysis of TAM dynamics in patients is consequently even more challenging.

In this thesis, I have sought to address these challenges through a complete and comprehensive analysis of the use of ^{19}F MRI. I have shown that this technique is a powerful strategy to image preclinical glioma and brain metastasis models, enabling the longitudinal and non-invasive monitoring of small, inflamed lesions. Importantly, the image acquisition was performed using a translationally-relevant clinical machine in the CHUV hospital. Given that MRI has been used to classify different brain malignancies [121], the imaging diagnostic repertoire might thereby be further augmented by the application of ^{19}F MRI. Indeed, we found significant differences in the PFCE-NP accumulation and distribution between the two brain tumor models, indicating a potential relevance for distinguishing high-grade gliomas and brain metastasis. Importantly, this observation may reflect the lower abundance of TAMs observed in brain metastasis, in both preclinical models and patient tissue samples [33, 34, 138], which could account for the lower accumulation of PFCE-NP.

In cancer, *ex vivo* labeling with PFC-NP has been used to non-invasively monitor cell-based therapies, such as in the context of adoptive T-cell transfer and DC-based cancer vaccination [139, 140]. *In vivo*, imaging of myeloid cells upon injection of PFC-NP has been only minimally investigated [115, 116, 141], and the detailed cellular composition of the labeled myeloid pool in different inflammation-associated contexts is only partially known [142]. In our study, we found that the myeloid-specific labeling with PFCE-NP in preclinical glioma models included several myeloid cell types, predominantly resident MG and peripherally-recruited MDMs. Notably, the labeling occurred directly within the tumor with no evident contribution of labeled cells infiltrating the tissue at later stages. Given that the cellular heterogeneity of the TME has been proposed to have direct translational implications [143], a detailed investigation of the PFCE-NP-labeled TAM pool enables one to better define the subpopulations being imaged. In this regard, gene expression analysis of the whole PFCE-NP-labeled TAM population allowed us to additionally investigate this complexity. Interestingly, we found a specific metabolic signature to be associated with PFCE-NP$^+$ TAMs, which may affect their phenotype and functionality [130, 144], and which was linked to their proximity to the tumor vasculature. While we did not investigate further the precise ontogeny of the labeled TAMs, these data suggest a potential implication of additional sub-populations, including CNS border-associated macrophages and perivascular macrophages (PVMs) [64].

Our data also showed that TAMs are not the sole cell population up-taking PFCE-NP. A small proportion of CD45$^-$ cells were also PFCE-NP$^+$, including several cell types such as endothelial

cells, which is potentially related to their active role in the trafficking of the NP. Uptake in other non-immune cells included cancer cells, as detected by IVM imaging. Consistently, rapidly dividing rat glioma cells have been shown to actively uptake nanoparticles by micropinocytosis *in vitro* [145]. Moreover, astrocytes have been shown to have phagocytic ability in experimental models involving the impairment of MG phagocytosis [147], and thus may also uptake the NP. Future experiments will therefore be important to study the precise ontogeny of the non-immune cells up-taking the PFCE-NP, as well as the underlying mechanism(s). Indeed, more research is critical to better understand the phagocytic process *in vivo*. While several studies have indicated a clear role for phagocytosis and macropinocytosis in PFC-NP uptake *in vitro* [125, 126], the IVM strategy presented in this study might be a valuable approach to address these open questions *in vivo* – which is of course most relevant. Of note, targeted NP are being developed to more efficiently target TAMs [107, 183], potentially allowing one to also design NP specific for other immune cells. In this context, IVM could represent a powerful platform to help design and evaluate cell type-specific NP to selectively target only a specific cell population of interest.

TAMs can adapt to tumor growth and in response to therapies by changes in abundance and their phenotypes [40, 75]. In this regard, ^{19}F MRI has allowed us to gain critical insights in a temporal and spatial manner to monitor distinct inflammatory changes throughout IR therapy response and regrowth by applying multispectral MR imaging of PFCE-NP and PFTBH-NP. We identified and validated different TME niches, which were distinctly characterized by their temporal and spatial appearance, and MG/MDM content. These niches were monitored before treatment and at recurrence, but importantly also during tumor dormancy. During this quiescent phase, several TAM-mediated resistance mechanisms have previously been described in the context of different therapeutic approaches [73, 75]. By using ^{19}F MRI we were successful in non-invasively monitoring the dormant tumors. Moreover, ^{19}F MRI revealed that IR not only led to a shift in the MDM:MG ratio, consistent with our previous findings using flow cytometry analyses [75], but also impacted the spatial distribution of the cells. This finding thereby layers on additional temporal and spatial variables to the concept of brain TME complexity, which we were able to follow in a clinically relevant manner.

In future experiments, it will be important to assess if, for example, the pre- and post-IR TME niches respond differently to specific treatments. In this regard, NP have also been shown to be an efficient carrier of macrophage-targeting compounds, and could thus be used as a therapeutic vector to differentially target specific niches [184]. Moreover, we also identified an IR-induced niche characterized by iron-rich TAMs (mainly MDMs). Importantly, iron is a crucial metal micronutrient whose metabolism within tumors is regulated by TAMs, with a consequent

effect on tumor growth [148]. Specifically, cancer cell proliferation has been shown to rely on iron in different cancer types, including leptomeningeal metastasis. In this recent study, metastatic cancer cells in the subarachnoid space were able to outcompete macrophages by taking up more iron, thereby sustaining their growth and potentially weakening the immune system within the CNS [185]. Furthermore, iron has also been shown to affect the activation state of macrophages themselves. Specifically, iron^{+} macrophages have been associated with an anti-tumorigenic role at the growing margins in a brain metastasis model [186], and generally high iron influx in macrophages has been linked with an M1-like phenotype in multiple tumor types [148]. Conversely, in the context of IR therapy, where we observed an increased frequency of iron^{+} MDMs, recent studies showed an overall pro-tumorigenic education of TAMs following IR in glioma models [75]. Thus, future single cell analyses will be relevant to fully understand the complexity of TAMs in response to IR and assess whether phenotypically opposing subpopulations appear following treatment.

Anti-angiogenic therapies and nanoparticle-based drug delivery have been comprehensively studied in brain tumors. The first, to achieve a better drug delivery by normalizing the vasculature [4], and the second, to direct drug accumulation within the tumor specifically. This would be expected to improve the pharmacokinetic profile, achieve continuous drug release and potentially lead to less side-effects [106]. The unique properties of the BBB, however, require a precise and thorough assessment of the effect of vascular integrity on drug delivery [4]. While anti-angiogenic treatment has been shown to improve the efficacy of chemotherapeutic agents in glioma models [149], different pediatric brain tumor models harboring distinct genetic drivers were shown to have a differential BBB impairment. Consequently, chemotherapy was delivered effectively only in medulloblastomas with disrupted vessels [150], which has important translational implications for treating children with this disease.

Our results also revealed an important relationship between vascular heterogeneity and PFCE-NP accumulation, as we observed NP accumulation only in areas of dysmorphic vessels. It is therefore crucial to carefully evaluate the molecular properties and the size of each of the drugs considered for combinatorial treatments, and also investigate how the unique brain vasculature could be modulated to optimize drug delivery. In sum, we propose ^{19}F MRI as a powerful MRI-based method to reveal key insights regarding the brain TME, along with conventional BBB leakage assessment using gadolinium. Of note, iron-loaded magnetic nanoparticles (MNP) have been used to predict response to therapy in a preclinical study, specifically to paclitaxel-encapsulated therapeutic nanoparticles (TNP) in a subcutaneous fibrosarcoma immunodeficient mouse model [187]. Through MRI-based

modeling of the MNP kinetics, the authors could predict TNP distribution and thereby stratify mice between responders and non-responders to TNP therapy [187]. Interestingly, MNP and TNP uptake occurred primarily in TAMs. Therefore, PFC-NP might also represent a potential strategy to predict the response to therapeutic NP. Moreover, in the same fibrosarcoma model, macrophage abundance was shown to correlate with vessel permeability upon IR treatment [188]. Specifically, IR increased TAM abundance (similarly to the project presented in this thesis, and the lab's previous study in multiple glioma models [75]), which mainly localized adjacent to highly permeable vessels [188]. Therefore, additional studies are required to explore the interplay between TAM presence and vessel permeability and determine how this interaction is modulated by different treatments. Any potential future clinical application of ^{19}F MRI requires rigorous answers to these open questions, as imaging at different time points during the clinical management of the patients will likely be impacted by several fluctuating factors affecting the TME. Additionally, detailed pharmacokinetics studies are needed to predict the PFC-NP distribution and the actual intracellular concentration *in vivo*. Importantly, while PFCs are generally inert and do not affect the cellular phenotype of *ex vivo* labeled cells [139, 189], any potential changes upon *in vivo* labeling are more challenging to assess.

Together, our study on ^{19}F MRI has shed light on the complexity of glioma biology and has resulted in new insights regarding the imaging and functions of myeloid cells in brain tumors. Accordingly, we propose ^{19}F MRI as an effective and powerful platform to non-invasively and longitudinally gain critical information regarding the composition and functionality of the brain TME. In the future, it will be of great interest to assess the predictive potential of ^{19}F MRI in relation to monitoring brain malignancy-related processes, including necrotic inflammation, pseudo-progression and pseudo-regression. This can lead to many benefits regarding the clinical management of glioma patients, including prediction of response to targeted treatments, and may be additionally harnessed for evaluation of other CNS diseases, as indicated by studies employing experimental models of multiple sclerosis and stroke [110, 190].

7.2 Intravital imaging of the brain TME

The TME is not a static milieu: during the course of tumor progression and in response to therapy, the cellular composition changes considerably [40, 75]. Conventional laboratory techniques allow researchers to investigate these dynamics, but are partially lacking in terms of addressing the temporal component of such longitudinal data. Moreover, tissue processing can impact its structure and the phenotypes of the associated cells. It is therefore important

to implement complementary approaches and to expand our repertoire of empirical techniques, which can be performed alongside current methods to gain a deeper understanding of key biological processes, including in cancer.

IVM is a cutting-edge approach for high-resolution cellular imaging, allowing one to visualize the cells in their natural environment and to monitor animals longitudinally. In doing so, it is of course critical to evaluate the components of the organ that has been imaged [191]. The location of the CIW in the skull gives visual access to the brain parenchyma, but also to the meningeal layers above it. While some IVM studies of the brain removed the dura mater during the window implantation [101], others left it intact [192, 193] and could visualize it by SHG [192]. In our IVM model, the dura mater was left in place to preserve the composition of the natural environment. Importantly, the dura mater-related SHG signal source was confirmed by *ex vivo* imaging. However, the skull craniotomy can potentially induce local inflammation and perturb the functions of the underlying meninges and parenchyma [191]. While our analyses did not reveal any alterations in the glioma TME following CIW implantation, in future experiments it will be important to also assess the potential impact on normal dura homeostasis and compare it to less invasive approaches such as mechanical thinning of the cranium. In a recent IVM study investigating the behavior and morphology of TAMs in a glioma model, image analysis starting at an imaging depth >50 µm from the pial surface was proposed as a means to differentiate the meninges and parenchyma [103]. In this regard, it will be important to consider this point in interpretation of the imaging data, although our PCA analysis indicated that the distance to the SHG signal was not driving any specific clustering of cells.

An interesting observation we were able to make for the first time via IVM was the identification of GFP^+ glioma cells within the dura. This implies that the normal parenchymal-meningeal boundaries have been disrupted, thereby representing an additional challenge to the definition of the normal anatomical structures. Importantly, recent studies reported the presence of lymphatics in the dura mater, which drain from the brain borders to the cervical lymph nodes [7, 8, 194]. Moreover, manipulation of the meningeal lymphatics in murine glioma models has been shown to be a potent therapeutic strategy to prime T cells and induce a better immune response against the tumor [9, 195]. Therefore, IVM has the unique potential to investigate the interactions between cancer cells, antigen-presenting cells, T cells and all other TME components at the meninges-tumor interface which could potentially be involved in regulating the adaptive immune response (or lack thereof). In order to achieve such detailed imaging, additional lineage-tracing models would be required as well as labeling strategies to delineate the different meningeal layers and vessels [191]. These interesting applications would necessitate the combination of multiple fluorophores, and it will therefore be crucial to

precisely define the cellular source of the different signals. Towards this end, the design and implementation of new deconvolution algorithms and spectral unmixing would facilitate the analysis pipeline [196].

New sophisticated methodologies are also required to analyze the large data sets created by IVM imaging. The generation of single cell data has opened a new era of research, with the main focus being various *omics*-approaches. However, imaging analysis of behavioral features and cellular morphology allows one to similarly apply unsupervised clustering to these types of data. Indeed, we found that dimensionality reduction of IVM-acquired data is a powerful strategy to define different subsets of cells. Interestingly, we identified a highly-migratory cluster of CX3CR1^{+} cells (likely MG, but with a potential additional contribution of dural BAMs). Our current cell lineage tracing strategy does not allow us to definitively discriminate MG from non-parenchymal macrophages. Importantly, leptomeningeal macrophages also express CX3CR1 and are only partially replenished by peripheral immune cells [64, 197]. Nonetheless, we could still investigate the variation of other parameters to more specifically delineate MG, such as cellular morphology or *Cx3cr1* expression. Although other brain resident non-parenchymal macrophages comprise only a small fraction of the total parenchymal MG population [197], we cannot exclude that these cells might account for a substantial number in the environment immediately below the CIW.

Future studies will also be important for a more detailed understanding of the migratory cues engaged by BLZ945 treatment. These could result from cellular activation following CSF1R inhibition and the release of chemo-attractants within the TME, but also be attributed to modifications of physical constraints that facilitate cellular movement. Furthermore, we also observed differential migratory behaviors depending on the genetic background of the tumor. Previous studies in our lab showed that genetically-distinct glioma GEMMs respond differentially to CSF1R inhibition [73, 75], and recent reports have indicated that the genetic makeup of gliomas impacts the cellular composition of the TME [40, 75]. Therefore, our findings further support the emerging notion that the underlying cancer cell genetics sculpt the TME, and can influence both tumor progression and response to therapy.

7.3 CSF1R targeting, alone and in combination with other therapeutic strategies

CSF1R has been shown to be an attractive candidate for targeting TAMs in gliomas and other preclinical tumor models [73, 75, 76, 81], and multiple CSF1R inhibitors have advanced to

clinical trials. Blockade of CSF1R signaling has been shown to impact both TAM phenotypes and viability [72, 75, 177]. In gliomas, CSF1R targeting with distinct small-molecule inhibitors led to a pronounced tumor regression [72, 73, 75, 90]. Importantly, CSF1R targeting efficacy can be further improved by combination with other treatments to avoid the development of resistance or to boost the adaptive immune response against the tumor [74, 75, 90, 94].

Surprisingly, the CSF1R targeting antibody 2G2 which I evaluated in this thesis, did not show any therapeutic efficacy in our glioma model, neither alone nor in combination with irradiation or anti-angiogenic therapy. We attempted to understand the molecular mechanisms that could explain these results, which are clearly different to the afore-mentioned studies using small-molecule inhibitors, but we did not obtain clear and conclusive answers. 2G2 antibody penetration was found to be incomplete and heterogeneous in mouse gliomas, potentially explaining the lack of evident efficacy. We tried a higher dosing schedule and employed a brain-shuttle version of 2G2, but neither resulted in any anti-glioma effects. Also, Fc-mediated ADCC does not seem to be a relevant mechanism for 2G2 in brain tumors, as shown in another study for this antibody, where both 2G2 and 2G2-Fc dead version were used to treat tumor-bearing mice in a subcutaneous adenocarcinoma model [177]. In this context, both antibodies efficiently depleted TAMs and had a similar therapeutic outcome [177].

Another potential explanation is that the small-molecule inhibitors BLZ945 and PLX3397 could have some affinity for other tyrosine kinases. However, for BLZ945 in particular, this was extensively tested at Novartis against a large panel of tyrosine kinases, and there was only high potency and selectivity for CSF1R. Experiments in which we combined treatment with BLZ945 (from a commercial source) in the context of 2G2 pre-treatment did not give conclusive results, which was most likely due to there being no impact of 2G2 therapy on the number of TAMs. We therefore have to conclude that the optimal experimental setup to understand the mechanism of 2G2 action, and lack of therapeutic response in the brain, is currently not available. For these reasons, this particular project was ended after the second year of my PhD. It is certainly possible that the imaging techniques which I developed in my subsequent years in the lab, including both IVM and *ex vivo* brain slice imaging, might have been potential tools to better understand 2G2 distribution, and as such these can be beneficial for similar projects in the future. This project also showed the importance of evaluating different therapeutic entities targeting the same receptor, and ideally to do that in different cancer models with distinct TMEs. This strategy can be extremely informative since it more closely represents the challenges inherent to the clinical situation, where the mutational landscape of each tumor and the individual differences of the TME in each organ and in each patient will likely drive differential responses to targeted therapies.

The divergent effects of the 2G2 antibody versus small-molecule CSF1R inhibitor therapies can be at least partially explained by major differences of these therapies in their ability to fully access the brain parenchyma and the glioma tumor bed. However, we also hypothesized that the observed differences might be additionally related to the strength of CSF1R pathway inactivation. Different studies have shown that phenotypic reprogramming can be a far more efficient therapeutic approach to harness TAMs to attack the tumor, rather than simply killing them [76]. Interestingly, IL34-deficient mice only partially lack MG, as confirmed by my independent characterization in this thesis, indicating that CSF1R signaling in this context might only be partially blunted, rather than completely blocked. While endogenous IL34 levels are highest in brain and skin, expression can be induced in other tissues under pathological conditions. Indeed in cancer, the induction of IL34 expression has been shown to mediate immunosuppression following chemotherapy in lung tumors, suggesting a possible role of this interleukin in shaping the TME [198, 199].

To assess the potential role of IL34 in gliomas, I performed several pilot experiments including orthotopic injection of a PDG glioma cell line in IL34 KO mice, and a survival trial using the Ink4a/Arf KO PDG GEMM. However, there were no differences in tumor development and survival, and analyses of the TME did not show any significant differences, including in MG abundance (despite the reduction in MG numbers in the normal brain parenchyma). Together, we infer that IL34 deficiency might be compensated for by CSF1, the major ligand for CSF1R, thereby dampening any potential effects on TAM abundance and phenotypes.

In conclusion, therapeutic targeting of the CSF1R pathway is highly dependent on the modality of signaling inhibition and modulation. Moreover, CSF1R inhibition can additionally have systemic effects due to the central role of this pathway in the biology of all macrophage populations in the body, which is critical to take into consideration in terms of the potential for toxicity in patients. As such, brain-specific factors driving the tumoral education of TAMs in gliomas and other brain cancers could represent important therapeutic avenues for future exploration. Moreover, novel NP-based approaches to enhance drug delivery have been recently shown to promote a tumor-specific accumulation of BLZ945 in a subcutaneous colon carcinoma model [200], and might be interesting to explore in our different preclinical models of brain cancer while simultaneously taking advantage of the knowledge we have now gained on NP distribution in the brain.

8. References

1. Yuste, R., *From the neuron doctrine to neural networks*, in *Nature Reviews Neuroscience*. 2015, Nature Publishing Group. p. 487-497.
2. Kuhn, S., et al., *Oligodendrocytes in Development, Myelin Generation and Beyond*, in *Cells 2019, Vol. 8, Page 1424*. 2019, Multidisciplinary Digital Publishing Institute. p. 1424.
3. Prinz, M., S. Jung, and J. Priller, *Microglia Biology: One Century of Evolving Concepts.* Cell, 2019. **179**(2): p. 292-311.
4. Arvanitis, C.D., G.B. Ferraro, and R.K. Jain, *The blood-brain barrier and blood-tumour barrier in brain tumours and metastases.* Nat Rev Cancer, 2020. **20**(1): p. 26-41.
5. Forrester, J.V., P.G. McMenamin, and S.J. Dando, *CNS infection and immune privilege*, in *Nature Reviews Neuroscience 2018 19:11*. 2018, Nature Publishing Group. p. 655-671.
6. Lima, K.A.d., J. Rustenhoven, and J. Kipnis, *Meningeal Immunity and Its Function in Maintenance of the Central Nervous System in Health and Disease*, in *https://doi.org/10.1146/annurev-immunol-102319-103410*. 2020, Annual Reviews p. 597-620.
7. Aspelund, A., et al., *A dural lymphatic vascular system that drains brain interstitial fluid and macromolecules*, in *Journal of Experimental Medicine*. 2015, The Rockefeller University Press. p. 991-999.
8. Louveau, A., et al., *Structural and functional features of central nervous system lymphatic vessels*, in *Nature 2015 523:7560*. 2015, Nature Publishing Group. p. 337-341.
9. Song, E., et al., *VEGF-C-driven lymphatic drainage enables immunosurveillance of brain tumours*, in *Nature 2020 577:7792*. 2020, Nature Publishing Group. p. 689-694.
10. Quail, D.F. and J.A. Joyce, *The Microenvironmental Landscape of Brain Tumors.* Cancer Cell, 2017. **31**(3): p. 326-341.
11. Mayor, R. and E. Theveneau, *The neural crest*, in *Development (Cambridge)*. 2012, Oxford University Press for The Company of Biologists Limited. p. 2247-2251.
12. Bjornsson, C.S., et al., *It takes a village: Constructing the neurogenic niche*, in *Developmental Cell*. 2015, Cell Press. p. 435-446.
13. Jung, E., et al., *Emerging intersections between neuroscience and glioma biology*, in *Nature Neuroscience*. 2019, Nature Research. p. 1951-1960.
14. Aldape, K., et al., *Challenges to curing primary brain tumours.* Nat Rev Clin Oncol, 2019.
15. Arndt V Hauri D, H.R., Junker C, Kuehni C, Lorez M, Pfeiffer V, Roy E, Schindler M, Feller A, *Swiss Cancer Report 2015. Federal Statistical Office (FSO)*. 2016.
16. *Surveillance, Epidemiology, and End Results (SEER) Program (www.seer.cancer.gov) SEER*Stat Database: Incidence - SEER 9 Regs Research Data, Nov 2018 Sub (1975-2016) <Katrina/Rita Population Adjustment> - Linked To County Attributes - Total U.S., 1969-2017 Counties, National Cancer Institute, DCCPS, Surveillance Research Program, released April 2019, based on the November 2018 submission.*
17. DN, L., et al., *The 2021 WHO Classification of Tumors of the Central Nervous System: a summary*, in *Neuro-oncology*. 2021, Neuro Oncol. p. 1231-1251.
18. Lapointe, S., A. Perry, and N.A. Butowski, *Primary brain tumours in adults*, in *The Lancet*. 2018, Lancet Publishing Group. p. 432-446.
19. Huang, J., et al., *Isocitrate dehydrogenase mutations in glioma: From basic discovery to therapeutics development*, in *Frontiers in Oncology*. 2019, Frontiers Media S.A.
20. Noushmehr, H., et al., *Identification of a CpG Island Methylator Phenotype that Defines a Distinct Subgroup of Glioma*, in *Cancer Cell*. 2010. p. 510-522.

21. Malta, T.M., et al., *Glioma CpG island methylator phenotype (G-CIMP): Biological and clinical implications*, in *Neuro-Oncology*. 2018. p. 608-620.
22. Hegi, M.E., et al., *MGMT Gene Silencing and Benefit from Temozolomide in Glioblastoma*, in *New England Journal of Medicine*. 2005, Massachusetts Medical Society p. 997-1003.
23. Gusyatiner, O. and M.E. Hegi, *Glioma epigenetics: From subclassification to novel treatment options.* Semin Cancer Biol, 2018. **51**: p. 50-58.
24. Wang, Q., et al., *Tumor Evolution of Glioma-Intrinsic Gene Expression Subtypes Associates with Immunological Changes in the Microenvironment*, in *Cancer Cell*. 2017, Cell Press. p. 42-56.e6.
25. Verhaak, R.G., et al., *An integrated genomic analysis identifies clinically relevant subtypes of glioblastoma characterized by abnormalities in PDGFRA, IDH1, EGFR and NF1*, in *Cancer Cell*. 2010. p. 98.
26. Neftel, C., et al., *An Integrative Model of Cellular States, Plasticity, and Genetics for Glioblastoma.* Cell, 2019. **178**(4): p. 835-849 e21.
27. Stupp, R., et al., *Radiotherapy plus concomitant and adjuvant temozolomide for glioblastoma.* N Engl J Med, 2005. **352**(10): p. 987-96.
28. Kaffes, I., et al., *Human Mesenchymal glioblastomas are characterized by an increased immune cell presence compared to Proneural and Classical tumors.* Oncoimmunology, 2019. **8**(11): p. e1655360.
29. Venteicher, A.S., et al., *Decoupling genetics, lineages, and microenvironment in IDH-mutant gliomas by single-cell RNA-seq.* Science, 2017. **355**(6332).
30. Stupp, R., et al., *Effect of Tumor-Treating Fields Plus Maintenance Temozolomide vs Maintenance Temozolomide Alone on Survival in Patients With Glioblastoma: A Randomized Clinical Trial.* JAMA, 2017. **318**(23): p. 2306-2316.
31. Lorez M Arndt V, R.S., Nanieva R, *Benign and Malignant Primary Brain Tumours in the Swiss Population (2010-2014)*, in *Swiss Cancer Bulletin*. 2018. p. 188-196.
32. Ricard, D., et al., *Primary brain tumours in adults.* Lancet, 2012. **379**(9830): p. 1984-96.
33. Klemm, F., et al., *Interrogation of the Microenvironmental Landscape in Brain Tumors Reveals Disease-Specific Alterations of Immune Cells.* Cell, 2020. **181**(7): p. 1643-1660 e17.
34. Friebel, E., et al., *Single-Cell Mapping of Human Brain Cancer Reveals Tumor-Specific Instruction of Tissue-Invading Leukocytes.* Cell, 2020. **181**(7): p. 1626-1642 e20.
35. Wang, L.B., et al., *Proteogenomic and metabolomic characterization of human glioblastoma.* Cancer Cell, 2021. **39**(4): p. 509-528 e20.
36. Hambardzumyan, D., et al., *Modeling Adult Gliomas Using RCAS/t-va Technology.* Transl Oncol, 2009. **2**(2): p. 89-95.
37. T, O., et al., *Most human non-GCIMP glioblastoma subtypes evolve from a common proneural-like precursor glioma*, in *Cancer cell*. 2014, Cancer Cell. p. 288-300.
38. Oldrini, B., et al., *Somatic genome editing with the RCAS-TVA-CRISPR-Cas9 system for precision tumor modeling*, in *Nature Communications 2018 9:1*. 2018, Nature Publishing Group. p. 1-16.
39. Li, Y., et al., *Arming Anti-EGFRvIII CAR-T With TGFβ Trap Improves Antitumor Efficacy in Glioma Mouse Models*, in *Frontiers in Oncology*. 2020, Frontiers. p. 1117.
40. Magod, P., et al., *Exploring the longitudinal glioma microenvironment landscape uncovers reprogrammed pro-tumorigenic neutrophils in the bone marrow.* Cell Rep, 2021. **36**(5): p. 109480.
41. WH, H., et al., *Contemporary Mouse Models in Glioma Research*, in *Cells*. 2021, Cells.
42. Taylor, O.G., J.S. Brzozowski, and K.A. Skelding, *Glioblastoma Multiforme: An Overview of Emerging Therapeutic Targets.* Front Oncol, 2019. **9**: p. 963.
43. O'Donnell, J.S., M.W.L. Teng, and M.J. Smyth, *Cancer immunoediting and resistance to T cell-based immunotherapy*, in *Nature Reviews Clinical Oncology*. 2019, Nature Publishing Group. p. 151-167.

44. Bejarano, L., M.J.C. Jordao, and J.A. Joyce, *Therapeutic Targeting of the Tumor Microenvironment.* Cancer Discov, 2021. **11**(4): p. 933-959.
45. Gill, J. and V. Prasad, *A reality check of the accelerated approval of immune-checkpoint inhibitors*, in *Nature Reviews Clinical Oncology 2019 16:11*. 2019, Nature Publishing Group. p. 656-658.
46. Quail, D.F. and J.A. Joyce, *Molecular Pathways: Deciphering Mechanisms of Resistance to Macrophage-Targeted Therapies.* Clin Cancer Res, 2017. **23**(4): p. 876-884.
47. Huang, B., et al., *Current Immunotherapies for Glioblastoma Multiforme.* Front Immunol, 2020. **11**: p. 603911.
48. Omuro, A., et al., *Nivolumab with or without ipilimumab in patients with recurrent glioblastoma: results from exploratory phase I cohorts of CheckMate 143.* Neuro Oncol, 2018. **20**(5): p. 674-686.
49. Reardon DA Brandes AA, O.A., *Randomized Phase 3 Study Evaluating the Efficacy and Safety of Nivolumab vs Bevacizumab in Patients With Recurrent Glioblastoma: CheckMate 143*, in *Neuro Oncol*. 2017. p. 21.
50. Gromeier, M., et al., *Very low mutation burden is a feature of inflamed recurrent glioblastomas responsive to cancer immunotherapy.* Nat Commun, 2021. **12**(1): p. 352.
51. Gil-Gil, M.J., et al., *Bevacizumab for the Treatment of Glioblastoma*, in *Clinical Medicine Insights: Oncology*. 2013. p. 123-135.
52. Hanahan, D. and Robert A. Weinberg, *Hallmarks of Cancer: The Next Generation*, in *Cell*. 2011, Elsevier. p. 646-674.
53. Pezzuto, A. and E. Carico, *Role of HIF-1 in Cancer Progression: Novel Insights. A Review*, in *Current Molecular Medicine*. 2018, Bentham Science Publishers Ltd. p. 343-351.
54. Jain, R.K., *Normalization of tumor vasculature: an emerging concept in antiangiogenic therapy.* Science, 2005. **307**(5706): p. 58-62.
55. Lanitis, E., M. Irving, and G. Coukos, *Targeting the tumor vasculature to enhance T cell activity*, in *Current Opinion in Immunology*. 2015, Elsevier Ltd. p. 55-63.
56. Levin, V.A., et al., *Impact of bevacizumab administered dose on overall survival of patients with progressive glioblastoma.* J Neurooncol, 2015. **122**(1): p. 145-50.
57. Lou, E., et al., *Bevacizumab therapy for adults with recurrent/progressive meningioma: a retrospective series.* J Neurooncol, 2012. **109**(1): p. 63-70.
58. Weller, M., et al., *EANO guidelines on the diagnosis and treatment of diffuse gliomas of adulthood.* Nat Rev Clin Oncol, 2021. **18**(3): p. 170-186.
59. van den Bent, M.J., et al., *Bevacizumab and temozolomide in patients with first recurrence of WHO grade II and III glioma, without 1p/19q co-deletion (TAVAREC): a randomised controlled phase 2 EORTC trial.* Lancet Oncol, 2018. **19**(9): p. 1170-1179.
60. T, S., et al., *Patients With Proneural Glioblastoma May Derive Overall Survival Benefit From the Addition of Bevacizumab to First-Line Radiotherapy and Temozolomide: Retrospective Analysis of the AVAglio Trial*, in *Journal of clinical oncology : official journal of the American Society of Clinical Oncology*. 2015, J Clin Oncol. p. 2735-2744.
61. Guilliams, M., et al., *Establishment and Maintenance of the Macrophage Niche*, in *Immunity*. 2020, Cell Press. p. 434-451.
62. Davies, L.C., et al., *Tissue-resident macrophages*, in *Nature Immunology 2013 14:10*. 2013, Nature Publishing Group. p. 986-995.
63. Kim, J.S., et al., *A Binary Cre Transgenic Approach Dissects Microglia and CNS Border-Associated Macrophages.* Immunity, 2021. **54**(1): p. 176-190 e7.
64. Kierdorf, K., et al., *Macrophages at CNS interfaces: ontogeny and function in health and disease.* Nat Rev Neurosci, 2019. **20**(9): p. 547-562.
65. Lapenna, A., M. De Palma, and C.E. Lewis, *Perivascular macrophages in health and disease.* Nat Rev Immunol, 2018. **18**(11): p. 689-702.
66. Bowman, R.L., et al., *Macrophage Ontogeny Underlies Differences in Tumor-Specific Education in Brain Malignancies.* Cell Rep, 2016. **17**(9): p. 2445-2459.

67. Hambardzumyan, D., D.H. Gutmann, and H. Kettenmann, *The role of microglia and macrophages in glioma maintenance and progression*, in *Nature Neuroscience*. 2015, Nature Publishing Group. p. 20-27.
68. Orecchioni, M., et al., *Macrophage Polarization: Different Gene Signatures in M1(LPS+) vs. Classically and M2(LPS–) vs. Alternatively Activated Macrophages*, in *Frontiers in Immunology*. 2019, Frontiers. p. 1084.
69. Pombo Antunes, A.R., et al., *Single-cell profiling of myeloid cells in glioblastoma across species and disease stage reveals macrophage competition and specialization.* Nat Neurosci, 2021. **24**(4): p. 595-610.
70. Bingle, L., N.J. Brown, and C.E. Lewis, *The role of tumour-associated macrophages in tumour progression: implications for new anticancer therapies.* J Pathol, 2002. **196**(3): p. 254-65.
71. Komohara, Y., et al., *Possible involvement of the M2 anti-inflammatory macrophage phenotype in growth of human gliomas.* J Pathol, 2008. **216**(1): p. 15-24.
72. Pyonteck, S.M., et al., *CSF-1R inhibition alters macrophage polarization and blocks glioma progression.* Nat Med, 2013. **19**(10): p. 1264-72.
73. Quail, D.F., et al., *The tumor microenvironment underlies acquired resistance to CSF-1R inhibition in gliomas.* Science, 2016. **352**(6288): p. aad3018.
74. Antonios, J.P., et al., *Immunosuppressive tumor-infiltrating myeloid cells mediate adaptive immune resistance via a PD-1/PD-L1 mechanism in glioblastoma.* Neuro Oncol, 2017. **19**(6): p. 796-807.
75. Akkari, L., et al., *Dynamic changes in glioma macrophage populations after radiotherapy reveal CSF-1R inhibition as a strategy to overcome resistance.* Sci Transl Med, 2020. **12**(552).
76. Kowal, J., M. Kornete, and J.A. Joyce, *Re-education of macrophages as a therapeutic strategy in cancer.* Immunotherapy, 2019. **11**(8): p. 677-689.
77. Molgora, M. and M. Colonna, *Turning enemies into allies-reprogramming tumor-associated macrophages for cancer therapy.* Med (N Y), 2021. **2**(6): p. 666-681.
78. von Roemeling, C.A., et al., *Therapeutic modulation of phagocytosis in glioblastoma can activate both innate and adaptive antitumour immunity*, in *Nature Communications 2020 11:1*. 2020, Nature Publishing Group. p. 1-12.
79. Willingham, S.B., et al., *The CD47-signal regulatory protein alpha (SIRPa) interaction is a therapeutic target for human solid tumors.* Proc Natl Acad Sci U S A, 2012. **109**(17): p. 6662-7.
80. Anfray, C., et al., *Current Strategies to Target Tumor-Associated-Macrophages to Improve Anti-Tumor Immune Responses.* Cells, 2019. **9**(1).
81. Cassetta, L. and J.W. Pollard, *Targeting macrophages: therapeutic approaches in cancer.* Nat Rev Drug Discov, 2018.
82. Yang, L. and Y. Zhang, *Tumor-associated macrophages: from basic research to clinical application.* J Hematol Oncol, 2017. **10**(1): p. 58.
83. Bubna, A.K., *Imiquimod - Its role in the treatment of cutaneous malignancies.* Indian J Pharmacol, 2015. **47**(4): p. 354-9.
84. N, v.R. and H. E, *Liposomes for specific depletion of macrophages from organs and tissues*, in *Methods in molecular biology (Clifton, N.J.)*. 2010, Methods Mol Biol. p. 189-203.
85. Flores-Toro, J.A., et al., *CCR2 inhibition reduces tumor myeloid cells and unmasks a checkpoint inhibitor effect to slow progression of resistant murine gliomas*, in *Proceedings of the National Academy of Sciences of the United States of America*. 2020, National Academy of Sciences. p. 1129-1138.
86. BZ, Q., et al., *CCL2 recruits inflammatory monocytes to facilitate breast-tumour metastasis*, in *Nature*. 2011, Nature. p. 222-225.
87. Coniglio, S.J., et al., *Microglial Stimulation of Glioblastoma Invasion Involves Epidermal Growth Factor Receptor (EGFR) and Colony Stimulating Factor 1 Receptor (CSF-1R) Signaling*, in *Molecular Medicine*. 2012, The Feinstein Institute for Medical Research. p. 519.

88. Ries, C.H., et al., *Targeting tumor-associated macrophages with anti-CSF-1R antibody reveals a strategy for cancer therapy.* Cancer Cell, 2014. **25**(6): p. 846-59.
89. Ries, C.H., et al., *CSF-1/CSF-1R targeting agents in clinical development for cancer therapy.* Curr Opin Pharmacol, 2015. **23**: p. 45-51.
90. Yan, D., et al., *Inhibition of colony stimulating factor-1 receptor abrogates microenvironment-mediated therapeutic resistance in gliomas.* Oncogene, 2017. **36**(43): p. 6049-6058.
91. Pixley, F.J. and E.R. Stanley, *CSF-1 regulation of the wandering macrophage: complexity in action.* Trends Cell Biol, 2004. **14**(11): p. 628-38.
92. Stanley, E.R. and V. Chitu, *CSF-1 receptor signaling in myeloid cells.* Cold Spring Harb Perspect Biol, 2014. **6**(6).
93. Wang, Y., et al., *IL-34 is a tissue-restricted ligand of CSF1R required for the development of Langerhans cells and microglia.* Nat Immunol, 2012. **13**(8): p. 753-60.
94. Cannarile, M.A., et al., *Colony-stimulating factor 1 receptor (CSF1R) inhibitors in cancer therapy.* J Immunother Cancer, 2017. **5**(1): p. 53.
95. Saha, D., R.L. Martuza, and S.D. Rabkin, *Macrophage Polarization Contributes to Glioblastoma Eradication by Combination Immunovirotherapy and Immune Checkpoint Blockade*, in *Cancer Cell*. 2017, Cell Press. p. 253-267.e5.
96. Chia-Chi Lin, et al. , *Phase I study of BLZ945 alone and with spartalizumab (PDR001) in patients (pts) with advanced solid tumors [abstract].* Cancer Res, 2020. **80**.
97. Butowski, N., et al., *Orally administered colony stimulating factor 1 receptor inhibitor PLX3397 in recurrent glioblastoma: an Ivy Foundation Early Phase Clinical Trials Consortium phase II study.* Neuro Oncol, 2016. **18**(4): p. 557-64.
98. Parkhurst, C.N., et al., *Microglia promote learning-dependent synapse formation through brain-derived neurotrophic factor.* Cell, 2013. **155**(7): p. 1596-609.
99. Boyer, S.W., et al., *All hematopoietic cells develop from hematopoietic stem cells through Flk2/Flt3-positive progenitor cells.* Cell Stem Cell, 2011. **9**(1): p. 64-73.
100. Suijkerbuijk, S.J.E. and J. van Rheenen, *From good to bad: Intravital imaging of the hijack of physiological processes by cancer cells*, in *Developmental Biology*. 2017, Academic Press. p. 328-337.
101. Alieva, M., et al., *Intravital imaging of glioma border morphology reveals distinctive cellular dynamics and contribution to tumor cell invasion*, in *Scientific Reports 2019 9:1*. 2019, Nature Publishing Group. p. 1-11.
102. Ricard, C., et al., *Phenotypic dynamics of microglial and monocyte-derived cells in glioblastoma-bearing mice*, in *Scientific Reports 2016 6:1*. 2016, Nature Publishing Group. p. 1-15.
103. Chen, Z., J.L. Ross, and D. Hambardzumyan, *Intravital 2-photon imaging reveals distinct morphology and infiltrative properties of glioblastoma-associated macrophages*, in *Proceedings of the National Academy of Sciences*. 2019, National Academy of Sciences. p. 14254-14259.
104. Uribe-Querol, E. and C. Rosales, *Phagocytosis: Our Current Understanding of a Universal Biological Process.* Front Immunol, 2020. **11**: p. 1066.
105. Weissleder, R., M. Nahrendorf, and M.J. Pittet, *Imaging macrophages with nanoparticles.* Nat Mater, 2014. **13**(2): p. 125-38.
106. Miller, M.A., S. Arlauckas, and R. Weissleder, *Prediction of Anti-cancer Nanotherapy Efficacy by Imaging.* Nanotheranostics, 2017. **1**(3): p. 296-312.
107. Leimgruber, A., et al., *Behavior of endogenous tumor-associated macrophages assessed in vivo using a functionalized nanoparticle.* Neoplasia, 2009. **11**(5): p. 459-68, 2 p following 468.
108. Rashidian, M., et al., *Noninvasive imaging of immune responses.* Proc Natl Acad Sci U S A, 2015. **112**(19): p. 6146-51.
109. Perez-Medina, C., et al., *PET Imaging of Tumor-Associated Macrophages with 89Zr-Labeled High-Density Lipoprotein Nanoparticles.* J Nucl Med, 2015. **56**(8): p. 1272-7.
110. Flogel, U., et al., *In vivo monitoring of inflammation after cardiac and cerebral ischemia by fluorine magnetic resonance imaging.* Circulation, 2008. **118**(2): p. 140-8.

111. van Heeswijk, R.B., et al., *Fluorine MR Imaging of Inflammation in Atherosclerotic Plaque in Vivo.* Radiology, 2015. **275**(2): p. 421-9.
112. van Heeswijk, R.B., et al., *Fluorine-19 magnetic resonance angiography of the mouse.* PLoS One, 2012. **7**(7): p. e42236.
113. Jacoby, C., et al., *Probing different perfluorocarbons for in vivo inflammation imaging by 19F MRI: image reconstruction, biological half-lives and sensitivity.* NMR Biomed, 2014. **27**(3): p. 261-71.
114. Darcot, E., et al., *A characterization of ABL-101 as a potential tracer for clinical fluorine-19 MRI.* NMR Biomed, 2020. **33**(1): p. e4212.
115. Makela, A.V. and P.J. Foster, *Imaging macrophage distribution and density in mammary tumors and lung metastases using fluorine-19 MRI cell tracking.* Magn Reson Med, 2018. **80**(3): p. 1138-1147.
116. Khurana, A., et al., *Visualization of macrophage recruitment in head and neck carcinoma model using fluorine-19 magnetic resonance imaging.* Magn Reson Med, 2018. **79**(4): p. 1972-1980.
117. Klemm, F. and J.A. Joyce, *Microenvironmental regulation of therapeutic response in cancer.* Trends Cell Biol, 2015. **25**(4): p. 198-213.
118. Tan, I.L., et al., *CSF1R inhibition depletes tumor-associated macrophages and attenuates tumor progression in a mouse sonic Hedgehog-Medulloblastoma model.* Oncogene, 2021. **40**(2): p. 396-407.
119. Florian Klemm, et al., *Compensatory CSF2-driven macrophage activation promotes adaptive resistance to CSF1R inhibition in breast-to-brain metastasis.* Nat Cancer, 2021. **in press**.
120. Smits, M., *MRI biomarkers in neuro-oncology.* Nat Rev Neurol, 2021. **17**(8): p. 486-500.
121. Swinburne, N.C., et al., *Machine learning for semi-automated classification of glioblastoma, brain metastasis and central nervous system lymphoma using magnetic resonance advanced imaging.* Ann Transl Med, 2019. **7**(11): p. 232.
122. Mehrabian, H., et al., *Advanced Magnetic Resonance Imaging Techniques in Management of Brain Metastases.* Front Oncol, 2019. **9**: p. 440.
123. Li, Q., et al., *Exploring MRI Characteristics of Brain Diffuse Midline Gliomas With the H3 K27M Mutation Using Radiomics.* Front Oncol, 2021. **11**: p. 646267.
124. Mukherjee, S., et al., *The yin and yang of imaging tumor associated macrophages with PET and MRI.* Theranostics, 2019. **9**(25): p. 7730-7748.
125. Nienhaus, F., et al., *Phagocytosis of a PFOB-Nanoemulsion for (19)F Magnetic Resonance Imaging: First Results in Monocytes of Patients with Stable Coronary Artery Disease and ST-Elevation Myocardial Infarction.* Molecules, 2019. **24**(11).
126. Ahrens, E.T., et al., *In vivo imaging platform for tracking immunotherapeutic cells*, in *Nat Biotechnol*. 2005. p. 983-987.
127. Herting, C.J., et al., *Tumour-associated macrophage-derived interleukin-1 mediates glioblastoma-associated cerebral oedema.* Brain, 2019. **142**(12): p. 3834-3851.
128. Di Costanzo, A., et al., *Proton MR spectroscopy of cerebral gliomas at 3 T: spatial heterogeneity, and tumour grade and extent.* Eur Radiol, 2008. **18**(8): p. 1727-35.
129. Bouvain, P., et al., *Dissociation of (19)F and fluorescence signal upon cellular uptake of dual-contrast perfluorocarbon nanoemulsions.* MAGMA, 2019. **32**(1): p. 133-145.
130. Carmona-Fontaine, C., et al., *Metabolic origins of spatial organization in the tumor microenvironment.* Proc Natl Acad Sci U S A, 2017. **114**(11): p. 2934-2939.
131. Chirizzi, C., et al., *Multispectral MRI with Dual Fluorinated Probes to Track Mononuclear Cell Activity in Mice.* Radiology, 2019. **291**(2): p. 351-357.
132. Puchala, M., Z. Szweda-Lewandowska, and J. Kiefer, *The influence of radiation quality on radiation-induced hemolysis and hemoglobin oxidation of human erythrocytes.* J Radiat Res, 2004. **45**(2): p. 275-9.
133. Rittase, W.B., et al., *Deposition of Iron in the Bone Marrow of a Murine Model of Hematopoietic Acute Radiation Syndrome.* Exp Hematol, 2020. **84**: p. 54-66.

134. Zormpas-Petridis, K., et al., *MRI Imaging of the Hemodynamic Vasculature of Neuroblastoma Predicts Response to Antiangiogenic Treatment.* Cancer Res, 2019. **79**(11): p. 2978-2991.
135. Wirsching, H.G., et al., *MRI and (18)FET-PET Predict Survival Benefit from Bevacizumab Plus Radiotherapy in Patients with Isocitrate Dehydrogenase Wild-type Glioblastoma: Results from the Randomized ARTE Trial.* Clin Cancer Res, 2021. **27**(1): p. 179-188.
136. Dregely, I., et al., *Imaging biomarkers in oncology: Basics and application to MRI.* J Magn Reson Imaging, 2018. **48**(1): p. 13-26.
137. Ku, M.C., et al., *Assessment of Blood Brain Barrier Leakage with Gadolinium-Enhanced MRI.* Methods Mol Biol, 2018. **1718**: p. 395-408.
138. Niesel, K., et al., *The immune suppressive microenvironment affects efficacy of radio-immunotherapy in brain metastasis.* EMBO Mol Med, 2021. **13**(5): p. e13412.
139. Gonzales, C., et al., *In-Vivo Detection and Tracking of T Cells in Various Organs in a Melanoma Tumor Model by 19F-Fluorine MRS/MRI.* PLoS One, 2016. **11**(10): p. e0164557.
140. Ahrens, E.T., et al., *Clinical cell therapy imaging using a perfluorocarbon tracer and fluorine-19 MRI.* Magn Reson Med, 2014. **72**(6): p. 1696-701.
141. Weibel, S., et al., *Imaging of intratumoral inflammation during oncolytic virotherapy of tumors by 19F-magnetic resonance imaging (MRI).* PLoS One, 2013. **8**(2): p. e56317.
142. Balducci, A., et al., *A novel probe for the non-invasive detection of tumor-associated inflammation.* Oncoimmunology, 2013. **2**(2): p. e23034.
143. Alvaro-Espinosa, L., et al., *Brain Microenvironment Heterogeneity: Potential Value for Brain Tumors.* Front Oncol, 2021. **11**: p. 714428.
144. Mohan, A.A., et al., *Targeting Immunometabolism in Glioblastoma.* Front Oncol, 2021. **11**: p. 696402.
145. Moore, A., R. Weissleder, and A. Bogdanov, Jr., *Uptake of dextran-coated monocrystalline iron oxides in tumor cells and macrophages.* J Magn Reson Imaging, 1997. **7**(6): p. 1140-5.
146. Zimmer, C., et al., *Tumor cell endocytosis imaging facilitates delineation of the glioma-brain interface.* Exp Neurol, 1997. **143**(1): p. 61-9.
147. Konishi, H., et al., *Astrocytic phagocytosis is a compensatory mechanism for microglial dysfunction.* EMBO J, 2020. **39**(22): p. e104464.
148. DeRosa, A. and A. Leftin, *The Iron Curtain: Macrophages at the Interface of Systemic and Microenvironmental Iron Metabolism and Immune Response in Cancer.* Front Immunol, 2021. **12**: p. 614294.
149. Mathivet, T., et al., *Dynamic stroma reorganization drives blood vessel dysmorphia during glioma growth.* EMBO Mol Med, 2017. **9**(12): p. 1629-1645.
150. Phoenix, T.N., et al., *Medulloblastoma Genotype Dictates Blood Brain Barrier Phenotype.* Cancer Cell, 2016. **29**(4): p. 508-522.
151. Sullivan, K.M., A. Dean, and M.M. Soe, *OpenEpi: a web-based epidemiologic and statistical calculator for public health.* Public Health Rep, 2009. **124**(3): p. 471-4.
152. Dai, C., et al., *PDGF autocrine stimulation dedifferentiates cultured astrocytes and induces oligodendrogliomas and oligoastrocytomas from neural progenitors and astrocytes in vivo.* Genes Dev, 2001. **15**(15): p. 1913-25.
153. Becher, O.J., et al., *Gli activity correlates with tumor grade in platelet-derived growth factor-induced gliomas.* Cancer Res, 2008. **68**(7): p. 2241-9.
154. Quail, D.F., et al., *Obesity alters the lung myeloid cell landscape to enhance breast cancer metastasis through IL5 and GM-CSF.* Nat Cell Biol, 2017. **19**(8): p. 974-987.
155. Hambardzumyan, D., et al., *Modeling Adult Gliomas Using RCAS/t-va Technology*, in *Translational Oncology*. 2009, Elsevier. p. 89-IN6.
156. Sevenich, L., et al., *Analysis of tumour- and stroma-supplied proteolytic networks reveals a brain-metastasis-promoting role for cathepsin S.* Nat Cell Biol, 2014. **16**(9): p. 876-88.

157. Chae, W.H., et al., *Evaluating Magnetic Resonance Spectroscopy as a Tool for Monitoring Therapeutic Response of Whole Brain Radiotherapy in a Mouse Model for Breast-to-Brain Metastasis.* Front Oncol, 2019. **9**: p. 1324.
158. Darcot, E., et al., *Compressed sensing with signal averaging for improved sensitivity and motion artifact reduction in fluorine-19 MRI.* NMR Biomed, 2021. **34**(1): p. e4418.
159. Colotti, R., et al., *Characterization of perfluorocarbon relaxation times and their influence on the optimization of fluorine-19 MRI at 3 tesla.* Magn Reson Med, 2017. **77**(6): p. 2263-2271.
160. Quail, D.F. and J.A. Joyce, *Microenvironmental regulation of tumor progression and metastasis.* Nat Med, 2013. **19**(11): p. 1423-37.
161. Ott, M., R.M. Prins, and A.B. Heimberger, *The immune landscape of common CNS malignancies: implications for immunotherapy.* Nat Rev Clin Oncol, 2021.
162. Chen, Z., J.L. Ross, and D. Hambardzumyan, *Intravital 2-photon imaging reveals distinct morphology and infiltrative properties of glioblastoma-associated macrophages.* Proc Natl Acad Sci U S A, 2019. **116**(28): p. 14254-14259.
163. Wellenstein, M.D. and K.E. de Visser, *Cancer-Cell-Intrinsic Mechanisms Shaping the Tumor Immune Landscape.* Immunity, 2018. **48**(3): p. 399-416.
164. Brennan, C.W., et al., *The somatic genomic landscape of glioblastoma.* Cell, 2013. **155**(2): p. 462-77.
165. Brown, G.C. and J.J. Neher, *Eaten alive! Cell death by primary phagocytosis: 'phagoptosis'.* Trends Biochem Sci, 2012. **37**(8): p. 325-32.
166. Miller, E.B., et al., *In vivo imaging reveals transient microglia recruitment and functional recovery of photoreceptor signaling after injury.* Proc Natl Acad Sci U S A, 2019. **116**(33): p. 16603-16612.
167. Benz, C., et al., *The stream of precursors that colonizes the thymus proceeds selectively through the early T lineage precursor stage of T cell development.* J Exp Med, 2008. **205**(5): p. 1187-99.
168. Muzumdar, M.D., et al., *A global double-fluorescent Cre reporter mouse.* Genesis, 2007. **45**(9): p. 593-605.
169. Quail, D.F. and J.A. Joyce, *Molecular Pathways: Deciphering Mechanisms of Resistance to Macrophage-Targeted Therapies*, in *Clin Cancer Res*. 2017. p. 876-884.
170. Faraco, G., et al., *Brain perivascular macrophages: characterization and functional roles in health and disease.* J Mol Med (Berl), 2017. **95**(11): p. 1143-1152.
171. DeNardo, D.G. and B. Ruffell, *Macrophages as regulators of tumour immunity and immunotherapy.* Nat Rev Immunol, 2019. **19**(6): p. 369-382.
172. Baghdadi, M., et al., *Interleukin-34, a comprehensive review.* J Leukoc Biol, 2018. **104**(5): p. 931-951.
173. van Vulpen, M., et al., *Changes in blood-brain barrier permeability induced by radiotherapy: implications for timing of chemotherapy? (Review).* Oncol Rep, 2002. **9**(4): p. 683-8.
174. Erturk, A., et al., *Three-dimensional imaging of solvent-cleared organs using 3DISCO.* Nat Protoc, 2012. **7**(11): p. 1983-95.
175. Johnsen, K.B., et al., *Targeting transferrin receptors at the blood-brain barrier improves the uptake of immunoliposomes and subsequent cargo transport into the brain parenchyma.* Sci Rep, 2017. **7**(1): p. 10396.
176. Herbrand, U., *Antibody-Dependent Cellular Phagocytosis: The Mechanism of Action That Gets No Respect A Discussion About Improving Bioassay Reproducibility.* BioProcessing Journal, 2016. **15**(1): p. 26-29.
177. Hoves, S., et al., *Rapid activation of tumor-associated macrophages boosts preexisting tumor immunity.* J Exp Med, 2018. **215**(3): p. 859-876.
178. Bissinger, S., et al., *Macrophage depletion induces edema through release of matrix-degrading proteases and proteoglycan deposition.* Sci Transl Med, 2021. **13**(598).
179. Martinez-Usatorre, A., et al., *Overcoming microenvironmental resistance to PD-1 blockade in genetically engineered lung cancer models.* Sci Transl Med, 2021. **13**(606).

180. Baer, C., et al., *Suppression of microRNA activity amplifies IFN-gamma-induced macrophage activation and promotes anti-tumour immunity.* Nat Cell Biol, 2016. **18**(7): p. 790-802.
181. Keklikoglou, I., et al., *Periostin Limits Tumor Response to VEGFA Inhibition.* Cell Rep, 2018. **22**(10): p. 2530-2540.
182. Salvagno, C., et al., *Therapeutic targeting of macrophages enhances chemotherapy efficacy by unleashing type I interferon response.* Nat Cell Biol, 2019. **21**(4): p. 511-521.
183. Zambito, G., et al., *Fluorinated PLGA-PEG-Mannose Nanoparticles for Tumor-Associated Macrophage Detection by Optical Imaging and MRI.* Front Med (Lausanne), 2021. **8**: p. 712367.
184. Rodell, C.B., et al., *TLR7/8-agonist-loaded nanoparticles promote the polarization of tumour-associated macrophages to enhance cancer immunotherapy.* Nat Biomed Eng, 2018. **2**(8): p. 578-588.
185. Chi, Y., et al., *Cancer cells deploy lipocalin-2 to collect limiting iron in leptomeningeal metastasis.* Science, 2020. **369**(6501): p. 276-282.
186. Leftin, A., et al., *Iron imaging reveals tumor and metastasis macrophage hemosiderin deposits in breast cancer.* PLoS One, 2017. **12**(9): p. e0184765.
187. Miller, M.A., et al., *Predicting therapeutic nanomedicine efficacy using a companion magnetic resonance imaging nanoparticle.* Sci Transl Med, 2015. **7**(314): p. 314ra183.
188. Miller, M.A., et al., *Radiation therapy primes tumors for nanotherapeutic delivery via macrophage-mediated vascular bursts.* Sci Transl Med, 2017. **9**(392).
189. Fink, C., et al., *Fluorine-19 Cellular MRI Detection of In Vivo Dendritic Cell Migration and Subsequent Induction of Tumor Antigen-Specific Immunotherapeutic Response*, in *Molecular Imaging and Biology*. 2019, Springer New York LLC.
190. Zhong, J., et al., *In Vivo Quantification of Inflammation in Experimental Autoimmune Encephalomyelitis Rats Using Fluorine-19 Magnetic Resonance Imaging Reveals Immune Cell Recruitment outside the Nervous System.* PLoS One, 2015. **10**(10): p. e0140238.
191. Coles, J.A., et al., *Where are we? The anatomy of the murine cortical meninges revisited for intravital imaging, immunology, and clearance of waste from the brain.* Prog Neurobiol, 2017. **156**: p. 107-148.
192. Ricard, C. and F.C. Debarbieux, *Six-color intravital two-photon imaging of brain tumors and their dynamic microenvironment.* Front Cell Neurosci, 2014. **8**: p. 57.
193. Askoxylakis, V., et al., *A cerebellar window for intravital imaging of normal and disease states in mice.* Nat Protoc, 2017. **12**(11): p. 2251-2262.
194. Petrova, T.V. and G.Y. Koh, *Organ-specific lymphatic vasculature: From development to pathophysiology.* J Exp Med, 2018. **215**(1): p. 35-49.
195. Hu, X., et al., *Meningeal lymphatic vessels regulate brain tumor drainage and immunity.* Cell Res, 2020. **30**(3): p. 229-243.
196. Kapsokalyvas, D., et al., *Multiview deconvolution approximation multiphoton microscopy of tissues and zebrafish larvae.* Sci Rep, 2021. **11**(1): p. 10160.
197. Jordao, M.J.C., et al., *Single-cell profiling identifies myeloid cell subsets with distinct fates during neuroinflammation.* Science, 2019. **363**(6425).
198. Baghdadi, M., et al., *High co-expression of IL-34 and M-CSF correlates with tumor progression and poor survival in lung cancers.* Sci Rep, 2018. **8**(1): p. 418.
199. Baghdadi, M., et al., *Chemotherapy-Induced IL34 Enhances Immunosuppression by Tumor-Associated Macrophages and Mediates Survival of Chemoresistant Lung Cancer Cells.* Cancer Res, 2016. **76**(20): p. 6030-6042.
200. Wei, Q., et al., *FXIIIa substrate peptide decorated BLZ945 nanoparticles for specifically remodeling tumor immunity.* Biomater Sci, 2020. **8**(20): p. 5666-5676.